Age and mantle sources of Quaternary basalts associated with ”leaky” transform faults of 1 the migrating Anatolia-Arabia-Africa triple junction

Michael A Cosca, Mary Reid, Jonathan R Delph, Gonca Gençalioğlu Kuşcu, Janne Blichert-Toft, Wayne Premo, Donna L Whitney, Christian Teyssier, Bora Rojay

To cite this version:

Michael A Cosca, Mary Reid, Jonathan R Delph, Gonca Gençalioğlu Kuşcu, Janne Blichert-Toft, et al.. Age and mantle sources of Quaternary basalts associated with ”leaky” transform faults of 1 the migrating Anatolia-Arabia-Africa triple junction. Geosphere, 2020, 17 (1), pp.1-26. ⟨10.1130/GES02266.1⟩. ⟨hal-02991152⟩

HAL Id: hal-02991152

https://hal.science/hal-02991152v1

Submitted on 5 Nov 2020

Geosphere

E: geosphere@geosociety.org
W: geosociety.org/gsa
T: @geosociety

Age and mantle sources of Quaternary basalts associated with "leaky" transform faults of the migrating Anatolia-Arabia-Africa triple junction

Tracking no: GS2266

Authors:
Michael Cosca (USGS), Mary Reid (Northern Arizona University), Jonathan Delph, Gonca Gençalioğlu Kuşcu (Muğla Sıtkı Koçman University), Janne Blichert-Toft, Wayne Premo (U.S. Geological Survey), Donna L. Whitney (Department of Geology and Geophysics, University of Minnesota), Christian Teyssier (University of Minnesota), and Bora Rojay (Middle East Technical University)

Abstract:
The Anatolia (Eurasia), Arabia, and Africa tectonic plates converge in SE Turkey, near the Gulf of İskenderun, forming a tectonically active and unstable triple junction (A3 triple junction). The plate boundaries are marked by broad zones of major, dominantly left-lateral transform faults including the East Anatolian fault zone (Anatolia-Arabia boundary) and the Dead Sea fault zone (Arabia-Africa boundary). Quaternary basalts occur locally within these "leaky" transform fault zones, providing evidence that mantle melting, basalt genesis, and eruption are linked to crustal deformation and faulting extending into the upper mantle. Samples of alkaline basalt (including basanite) from two volcanic fields (Toprakkale and Karasu) are investigated within a broad zone of transtension associated with these plate boundary faults near the İskenderun and Amik Basins, respectively. Immediately beneath the study area, seismic velocities of the upper mantle beneath southern Anatolia reveal thick lithosphere, including parts of the subducted African continental margin, in stark contrast with much thinner mantle lithosphere (~60 km) underlying the adjacent Arabian margin. Melting depths estimated for the alkaline rocks generally cluster between 60 and 70 km over a wide region, in agreement with the seismic structure, with a second clustering of pressures at ~90 km depth for the basanites. Toprakkale basalts have 40Ar/39Ar plateau ages ranging from 810 {plus minus} 60 ka to 46 {plus minus} 13 ka, and Karasu volcanic field basalts have 40Ar/39Ar plateau ages ranging from 2.63 {plus minus} 0.17 Ma to 52 {plus minus} 16 ka. Toprakkale basalts have 176Hf/177Hf ratios (0.282966 to 0.283019) somewhat higher than those of Karasu basalts (0.282837 to 0.282965), with some overlap in 143Nd/144Nd ratios (0.512781 to 0.512866 versus 0.512648 to 0.512806). Toprakkale 206Pb/204Pb ratios (19.025 {plus minus} 0.001) exhibit less variation than in Karasu basalts (18.800 to 19.324), and 208Pb/204Pb values for the Toprakkale basalts (38.978 to 39.103) are slightly lower than in Karasu basalts (39.100 to 39.219). Two basanites within the Toprakkale volcanic field have 87Sr/86Sr of 0.0703070 and 0.703136, 143Nd/144Nd of 0.512931 and 0.512893, 176Hf/177Hf of 0.283019 and 0.282995, 206Pb/204Pb of 19.087 and 19.155, and 208Pb/204Pb of 38.861 and 38.915. We interpret the combined radiogenic isotope data (Sr, Nd, Hf, Pb) from all alkaline basalts to reflect partial melting at the base of the mantle lithosphere, while the basanites are interpreted as possibly including some melt contributions from lithospheric mantle blocks that foundered and melted at ~90 km depth within the asthenosphere. The plate boundaries and the position of the A3 triple junction appear to have migrated to the SW since the beginning of the Pliocene as the Anatolia-Africa plate boundary has adjusted to extrusion of the Anatolian plate. The current position of the A3 triple junction is near the Amik Basin, but faults, seismicity, and topographic expressions indicate that inception of the triple junction began as early as 5 Ma in a position farther to the NE. Quaternary basalts studied here are restricted to a broad zone of transtension formed in response to these plate adjustments. Establishment of the triple junction over the past 5 Ma was synchronous with rollback of the African slab beneath Anatolia and associated trench retreat, consistent with Pliocene uplift in Cyprus and with the current positions of plate boundaries. The A3 triple junction is considered unstable and likely to continue migrating to the SW for the foreseeable geologic future.

Age and mantle sources of Quaternary basalts associated with "leaky" transform faults of the migrating Anatolia-Arabia-Africa triple junction

Michael A. Cosca[1], Mary Reid[2], Jonathan R. Delph[3], Gonca Gençalioğlu Kuşcu [4], Janne Blichert-Toft[5], Wayne Premo[1], Donna L. Whitney[6], Christian Teyssier[6], Bora Rojay[7]

[1]U.S. Geological Survey, Denver, USA
[2]Northern Arizona University, Flagstaff, USA
[3]University of Oregon, Eugene, USA
[4]Muğla Sıtkı Koçman University, Muğla Turkey
[5]Laboratoire de Géologie de Lyon, Ecole Normale Supérieure de Lyon, CNRS UMR 5276, Université de Lyon, 46 Allée d'Italie, 69007 Lyon, France
[6]University of Minnesota, Minneapolis, USA
[7]Middle East Technical University, Ankara, Turkey

Abstract

The Anatolia (Eurasia), Arabia, and Africa tectonic plates converge in SE Turkey, near the Gulf of İskenderun, forming a tectonically active and unstable triple junction (A^3 triple junction). The plate boundaries are marked by broad zones of major, dominantly left-lateral transform faults including the East Anatolian fault zone (Anatolia-Arabia boundary) and the Dead Sea fault zone (Arabia-Africa boundary). Quaternary basalts occur locally within these "leaky" transform fault zones, providing evidence that mantle melting, basalt genesis, and eruption are linked to crustal deformation and faulting extending into the upper mantle. Samples of alkaline basalt (including basanite) from two volcanic fields (Toprakkale and Karasu) are investigated within a broad zone of transtension associated with these plate boundary faults near the İskenderun and Amik Basins, respectively. Immediately beneath the study area, seismic velocities of the upper mantle beneath southern Anatolia reveal thick lithosphere, including parts of the subducted African continental margin, in stark contrast with much thinner mantle lithosphere (~60 km) underlying the adjacent Arabian margin. Melting depths estimated for the alkaline rocks generally cluster between 60 and 70 km over a wide region, in agreement with the seismic structure, with a second clustering of pressures at ~90 km depth for the basanites.

Toprakkale basalts have $^{40}Ar/^{39}Ar$ plateau ages ranging from 810 ± 60 ka to 46 ± 13 ka, and Karasu volcanic field basalts have $^{40}Ar/^{39}Ar$ plateau ages ranging from 2.63 ± 0.17 Ma to 52 ± 16 ka. Toprakkale basalts have $^{176}Hf/^{177}Hf$ ratios (0.282966 to 0.283019) somewhat higher than those of Karasu basalts (0.282837 to 0.282965), with some overlap in $^{143}Nd/^{144}Nd$ ratios (0.512781 to 0.512866 versus 0.512648 to 0.512806). Toprakkale $^{206}Pb/^{204}Pb$ ratios (19.025 ± 0.001) exhibit less variation than in Karasu basalts (18.800 to 19.324), and $^{208}Pb/^{204}Pb$ values for

the Toprakkale basalts (38.978 to 39.103) are slightly lower than in Karasu basalts (39.100 to 39.219). Two basanites within the Toprakkale volcanic field have $^{87}Sr/^{86}Sr$ of 0.0703070 and 0.703136, $^{143}Nd/^{144}Nd$ of 0.512931 and 0.512893, $^{176}Hf/^{177}Hf$ of 0.283019 and 0.282995, $^{206}Pb/^{204}Pb$ of 19.087 and 19.155, and $^{208}Pb/^{204}Pb$ of 38.861 and 38.915. We interpret the combined radiogenic isotope data (Sr, Nd, Hf, Pb) from all alkaline basalts to reflect partial melting at the base of the mantle lithosphere, while the basanites are interpreted as possibly including some melt contributions from lithospheric mantle blocks that foundered and melted at ~90 km depth within the asthenosphere.

The plate boundaries and the position of the A^3 triple junction appear to have migrated to the SW since the beginning of the Pliocene as the Anatolia-Africa plate boundary has adjusted to extrusion of the Anatolian plate. The current position of the A^3 triple junction is near the Amik Basin, but faults, seismicity, and topographic expressions indicate that inception of the triple junction began as early as 5 Ma in a position farther to the NE. Quaternary basalts studied here are restricted to a broad zone of transtension formed in response to these plate adjustments. Establishment of the triple junction over the past 5 Ma was synchronous with rollback of the African slab beneath Anatolia and associated trench retreat, consistent with Pliocene uplift in Cyprus and with the current positions of plate boundaries. The A^3 triple junction is considered unstable and likely to continue migrating to the SW for the foreseeable geologic future.

Introduction

Near the Gulf of İskenderun in the eastern Mediterranean Sea, the tectonic plates of Africa, Anatolia, and Arabia intersect to form an unstable triple junction (referred to here as the A^3 triple junction) along left lateral transform faults (Dewey et al., 1986) (Fig. 1). This instability is associated with significant crustal deformation, reflected by broad regions of high seismicity (Ergin et al., 2004), apparent crustal thinning (Abgarmi et al., 2017), and the development of transtensional basins (e.g., Cilicia-Adana-İskenderun and Samandağ-Amik-Karasu-Narli) and transpressional ranges (e.g., Amanos Mountains) under conditions of complex strain partitioning (Tatar et al., 2004; Aksu et al., 2005; Seyrek et al., 2007). Within this dynamic setting, small volumes of Quaternary mafic lava occur locally along transform fault segments and/or between rotating crustal blocks within fault zones (e.g., Tatar et al., 2004; Kavak et al., 2009). Because these near-primary basalts are restricted spatially to zones associated with the A^3 triple junction, this magmatism provides an opportunity to study melt generation within an actively developing continental plate boundary.

Modern-day geophysical methods provide insight into physical heterogeneities within the Earth's crust and mantle at depths where magmas are sourced, and this insight is particularly useful for characterizing the generation of recently erupted near-primary melts (e.g., Plank and Forsyth, 2016; Reid et al., 2019). The integration of geochemical and geophysical datasets furthers understanding of the chemical, thermal, and physical evolution of tectonically active regions. New data from the US NSF Continental Dynamics-Central Anatolian Tectonics (CD-CAT) seismic deployment (e.g., Abgarmi et al., 2017) vastly increased seismic coverage in south-central Anatolia, thus providing unprecedented imaging of physical contrasts in the crust and upper mantle. Geophysical images of the upper mantle beneath southern Anatolia near the A^3 triple junction highlight inferred regions of subducted Neotethyan oceanic lithosphere and associated African continental margin (Biryol et al., 2011; Abgarmi et al., 2017; Delph et al., 2017; Portner et al., 2018). Lateral changes in Anatolian upper mantle velocity structure are consistent with the regional distribution of Quaternary magmatism, such that magmatism near the triple junction is generally restricted to areas underlain by thinner lithosphere (Delph et al., 2017). Understanding how these lithospheric contrasts in seismic data may correlate with the geochemistry of Quaternary volcanic rocks, however, requires a more careful analysis of magma source characteristics.

In this study, we present rock compositions, high-precision $^{40}Ar/^{39}Ar$ geochronology, and radiogenic isotope geochemistry (including some of the first Hf and Pb isotope data) of Quaternary basalts from two volcanic fields proximal to transform fault segments of the A^3 triple junction alongside a compilation of published results, and compare the integrated dataset with seismic images of the uppermost mantle. We demonstrate that the geochemical and geophysical data support magma generation at two distinct depth intervals, consistent with melting of both lithospheric and asthenospheric mantle sources. When placed within the tectonic context of the region, the ascent of these basaltic magmas is likely facilitated by plate boundary "leaky" transform faults. These results have implications for the timing and position of the developing triple junction, evolution of plate boundary faults, and tectonic escape of the Anatolian microplate.

Tectonic Setting

Tectonic forces controlling movements between the Anatolian, African, and Arabian plates in the eastern Mediterranean have led to the development of a tectonically complex and unstable triple junction (e.g., Şengör et al., 1985; Perinçek and Çemen, 1990; Reilinger et al., 2006). Modern geodesy and radar measurements show relative plate displacements up to 20 mm a^{-1} (Reilinger et al., 2006; Mahmoud et al., 2013; Cavalié and Jónsson, 2014). The A^3 triple junction is currently centered near the Amik sub-basin within the Karasu rift (Fig. 2A) (Dewey et al., 1986; Over et al., 2004), however other triple junction locations have been proposed and names applied owing to the tectonic complexity and distributed deformation within the region (e.g., Karig and Kozlu, 2009; Tari et al., 2014). The three plates are separated by two major transform fault systems: the left-lateral NE-SW trending East Anatolian fault zone (EAFZ) and its southern linkage to the left-lateral N-S trending Dead Sea fault zone (DSFZ) (Dewey and Şengör, 1979; Rojay et al, 2001; Westaway, 2004; Tatar et al., 2004; Duman and Emre, 2013) (Fig. 2A). Here, both transtension and transpression are recorded in a significant network of smaller faults subparallel to the plate boundaries (e.g., Kavak et al., 2009). Focal mechanisms between fault zones reflect their complex interplay, showing normal, thrust, and mixed compressional and extensional oblique-slip over a large range of depths (Ergin et al., 2004). Within the field area, transtension across a wide area surrounding the A^3 triple junction has resulted in the development of major basins, including the Cilicia-Adana-İskenderun Basins and the Karasu Basin (including its Samandağ, Amik, and Narli sub-basins) located northwest and southeast of the EAFZ, respectively (Fig. 2A).

The DSFZ and the EAFZ are neotectonic geologic structures that cross-cut an earlier orogenic belt of late Cretaceous ophiolites, including the Kızıldağ (Amanos) and Baer Bassit ophiolites

(Fig. 2A). These ophiolites represent the former collision zone (Bitlis suture) between the Nubian (Africa-Arabia) – Eurasian (Anatolia) plates and the intervening Neotethys ocean. This ophiolite mélange was itself over-thrusted during the late Miocene by Jurassic-Cretaceous platform carbonates, equivalent to those exposed in the Kyrenia range in Cyprus, forming an imbricated stack of ophiolite and carbonate rocks (e.g., Şengör and Yılmaz, 1981). Near the Gulf of İskenderun the transition from a largely compressional tectonic system to one dominated by transtension and transpression developed when rifting in the Red Sea began in the late Miocene, leading to formation of the translational DSFZ – EAFZ fault system, and finally by tectonic extrusion of the Anatolian plate along the EAFZ (e.g., Şengör et al., 1985; Hempton, 1987; Brocard et al., 2020).

The EAFZ has been active since the Pliocene (e.g., McKenzie, 1976; Şengör et al., 1985; Muehlberger and Gordon, 1987) with present-day average left-lateral slip estimated by GPS of ~ 10 mm a^{-1} (Reilinger et al., 2006). Near the town of Çelikhan, the EAFZ splits into two main segments (a northern and a main southern strand) largely separated by the Amanos Mountains (Duman and Emre, 2013) (Fig. 2B). The Amanos Mountains, a ~ 2300 m elevation range, is an uplifted block of Precambrian-cored continental crust within a major zone of transpression, and despite its position between the two major strands of the EAFZ, contains few mapped Quaternary faults. This apparent tectonic rigidity is consistent with its relatively recent and coherent uplift since 4 Ma (Seyrek at al., 2008), and the stark relief of the Amanos Mountains relative to the low-relief Arabian margin suggests a strong asymmetry in structural deformation and differential crustal uplift (e.g., Rojay, 2001; Reilinger et al., 2006).

The main southern strand of the EAFZ extends ~ 580 km from the so-called Karlıova triple junction in the east, where it joins the North Anatolian fault, to the Amik Basin in the west (Rojay et al., 2001; Westaway, 2004; Kavak et al., 2009; Duman and Emre, 2013). The Amik Basin approximately coincides with the northern termination of the DSFZ, which accommodates ~ 5 mma^{-1} of left-lateral motion between the African and Arabian plates (Reilinger et al., 2006; Mahmoud et al., 2013) (Fig. 2A), and its continuation as the main southern strand of the EAFZ (e.g., Arpat and Şaroğlu, 1972; Rojay et al., 2001; Westaway, 2004; Kavak et al., 2009; Duman and Emre, 2013; Yuce et al., 2014). Where the EAFZ transits the Karasu valley (also referred to as rift, trough, basin, or graben), it is characterized by a diffuse network of individual fault segments comprising several restraining and releasing bends (Duman and Emre, 2013). The Karasu valley is bordered on its western margin by the Amanos Mountains and the east-dipping Karasu (Amanos) fault zone, and on its eastern margin by the west-dipping Yesemek (East Hatay) fault zone (Rojay et al., 2001; Seyrek et al., 2008; Duman and Emre, 2013) (Fig. 2A). Farther to the southeast the Aaferin fault represents a major fault splay of the DSFZ that roughly parallels the Karasu valley before linking with the main strand of the EAFZ near the town of Kahramanmaraş (Fig. 2A).

The northern segment of the EAFZ diverges from the main segment of the EAFZ near the village of Çelikhan, continuing ~ 350 km toward the Gulf of İskenderun. Similar to the main southern strand of the EAFZ, the northern strand consists of several individual fault segments, connected by releasing and restraining bends and ultimately projecting offshore on strike toward the Kyrenia- Misis fault zone (Fig. 2A) (Duman and Emre, 2013). Both the northern and southern strands of the EAFZ project offshore into the Mediterranean, likely connecting to major fault networks associated with the Cyprean trench (e.g., Duman and Emre, 2013) where strike-slip deformation related to the interaction of the three plates gives way to compressional deformation related to the northward movement of the African plate (e.g., Imprescia et al., 2012). The northern strand of the EAFZ becomes diffuse as it approaches the Gulf of İskenderun, as deformation is distributed across smaller faults within a broad zone of transtension. Along the northern margin of the Gulf of İskenderun two subparallel fault segments, the Karataş and Yumurtalık faults (Fig. 2B) are sinistral strike slip faults with some reversed throw, can be considered as examples of such small discontinuous faults that are part of a much broader network of transtension. The Karataş and Yumurtalık faults were previously referred to as the Karataş-Osmaniye fault (e.g., McKenzie, 1976), and have often been considered the boundary between Anatolian and African lithosphere (e.g., Parlak et al., 1997; Gürsoy et al., 2003; Westaway, 2003; 2004; Seyrek et al., 2008; Kavak et al., 2009).

Quaternary (Leaky Transform) Volcanism Along the EAFZ

Locally occurring along and/or near both the northern and southern fault segments of the EAFZ are two small Quaternary volcanic fields (here referred to as the Toprakkale and Karasu volcanic fields) (Figs. 2A and 2B) containing small volcanic cones, lava flows, and ash fall deposits (e.g., Parlak et al., 1997, 1998; Alıcı et al., 2001; Yurtmen et al., 2000; Kavak et al., 2009). Quaternary volcanic rocks along the EAFZ are neither voluminous nor widespread and are absent west of the İskenderun Basin and similarly absent northeast of Fevzipaşa along the main strand of the EAFZ (Fig. 2B).

Toprakkale Volcanic Field

The Toprakkale volcanic field refers to all of the Quaternary volcanic centers and lava flows of the Ceyhan-Osmaniye-Erzin-Toprakkale region, including the basaltic ash-fall deposits along the northern shore of the Gulf of İskenderun near İncirli (e.g., Polat et al., 1997; Arger et al., 2000; Yurtmen et al., 2000; Bağcı et al., 2011; Italiano et al., 2017; Oyan, 2018) (Fig. 2B). Volcanism in the Toprakkale volcanic field is spatially associated with the roughly parallel NE-SW trending Karataş and Yumurtalık faults, and a small stepover near the Delihalil volcano represented by the Toprakkale fault (Duman and Emre, 2013).

Published ^{40}Ar/^{39}Ar and K-Ar ages between 0.1 and 2.3 Ma for basalts in the Toprakkale volcanic field (Arger et al., 2000; Oyan, 2018) are consistent with paleomagnetic studies of volcanic rocks along the northern strand of the EAFZ that have both normal and reversed polarities (Gürsoy et al., 2003). The Toprakkale volcanic rocks are mafic, with high combined alkalis ($Na_2O + K_2O$), and are classified as basanites and basalts (Fig. 3). Relative to primitive mid-ocean ridge basalts (MORB), they are enriched in light rare earth elements (LREE), large ion lithophile elements (LILE), and high field strength elements (HFSE) (e.g., Polat et al., 1997; Arger et al., 2000; Yurtmen et al., 2000; Bağcı et al., 2011). The radiogenic isotopic signatures ^{87}Sr/^{86}Sr and ^{143}Nd/^{144}Nd are consistent with derivation from an isotopically depleted, ocean island basalt (OIB)-like mantle source. Trace element differences between the basanites and alkaline basalts have been argued to indicate differential degrees of mantle lithosphere partial melting (1.5-4.6% vs 9.2%) (Bağcı et al., 2011; Oyan, 2018).

Karasu Volcanic Field

The Karasu volcanic field includes all localized Quaternary lava flows and vents in the Amik Basin, a sub-basin within the Karasu rift, exposed over a distance of approximately 60 km between Kırıkhan and Fevzipaşa (Figs. 2A and 2B) (Rojay et al. 2001). Northeast of Fevzipaşa a tectonic saddle separates the Amik and Narli sub-basins and also areas containing Quaternary versus Miocene volcanic rocks (Rojay et al. 2001). Borehole data within the Karasu valley are consistent with sedimentation and volcanism occurring throughout much of the Quaternary, as the Karasu valley continues to act as a zone of active infilling, with sag structures (sub-basins) consistent with active transpression (Rojay et al., 2001).

When plotted on a conventional total alkali versus SiO_2 rock discrimination plot, the volcanic rocks from the Karasu volcanic field plot almost entirely within the basalt field (Fig. 3), but can be considered alkalic basalts if discriminated using the Zr/Ti vs Nb/Y diagram of Pearce (1996). In notable contrast with the Toprakkale volcanic field, no basanites have been described from the Karasu volcanic field. On the basis of normative mineralogy and geochemical data, Alıcı et al. (2001) distinguished alkali olivine basalts from quartz- or olivine-tholeiites from the Karasu valley. However, this level of rock discrimination is poorly resolved in the geochemical and isotopic data with, for example, $^{87}Sr/^{86}Sr$ and $^{143}Nd/^{144}Nd$ values showing considerable overlap. The wide range in $^{87}Sr/^{86}Sr$ (0.703353 to 0.705490) and trace element compositions could indicate crustal contamination in many of the samples from the Karasu valley (Alıcı et al., 2001).

Samples

Eight samples of fresh volcanic rock were collected from both the Toprakkale volcanic field (5 samples) and the Karasu volcanic field (3 samples) in July, 2012 (Fig. 2B). All of the samples are either directly or proximally associated with fault segments of the EAFZ. Within the Toprakkale volcanic field, samples of dark basaltic rock were collected from outcrops including near the summit of the Quaternary Delihalil volcano (R12OS-1, -3), and near the town of Toprakkale (R12OS-4). Additional samples were collected from layered volcanic flow and ash deposits that occur along the northern margin of the Gulf of İskenderun, in the vicinity of the Yumurtalık fault (R12OS -5, -6). Two samples from the Karasu volcanic field were collected near the village of Hassa (R12HA -01, -02), associated with the Hassa fault segment of the Karasu (Amanos) fault segment of the southern strand of the EAFZ (Fig. 2B), and from Fevzipaşa (R12Ha-03), near the İslahiye releasing bend of the Karasu fault along the western side of the Karasu valley. Samples R12HA-1 and -2 were collected in an area where several small volcanic centers (Büyük, Güvenç, Hassa, Bosalan) occur (Fig. 2B), possibly within local dilational zones ("spenochasms" Tatar et al., 2004) formed in response to differential stress along the EAFZ. Sample R12HA-1 was collected from a lava flow exposed within a flowing creek bed, and sample R12HA-02 was collected from stratigraphically overlying fresh lava. These sample sites are within the much larger regional K-Ar geochronology study by Rojay et al. (2001) and were collected to try to gain better precision on the ages from this area. Specific sample procedures corresponding to different analytical methods are described below.

Methods

Rock chemistry

Surficial contamination was removed from rock samples by extensive rinsing in water, followed by a sequence of 5-10 minute ultrasonification that progressed from dilute (~2%) hydrogen peroxide to dilute (~0.01 N) hydrochloric acid, with intermediate and final steps in distilled water. Major and trace element concentrations were determined on rock powders by quantitative X-ray fluorescence spectrometry, inductively coupled plasma mass spectrometry, and inductively coupled plasma atomic emission mass spectrometry. Samples for this investigation were analyzed by SGS Minerals in Lakefield, Ontario, using standard methods and calibrations.

^{40}Ar/^{39}Ar

The ^{40}Ar/^{39}Ar analyses were performed at the U.S. Geological Survey (USGS) in Denver, CO. Fresh rock fragments of approximately 3mm^3 in size were prepared by crushing, washing in deionized water, and handpicking. Together with the neutron fluence monitor Fish Canyon sanidine, samples were loaded into precise positions within 18 mm Al disks, stacked, wrapped in Al foil, and encapsulated under vacuum in a quartz tube. The quartz tube was sealed into an Al canister and rotated at 1 rpm during neutron irradiation for 11 MWH in the central thimble position of the USGS TRIGA reactor (Dalrymple et al., 1981). Following irradiation, the samples and fluence monitors were loaded with tweezers into a stainless-steel sample holder and then placed into a laser chamber with an externally pumped ZnSe window, which is attached to a custom-built ultra-high vacuum extraction line. The volume of the mostly stainless-steel vacuum extraction line, including a cryogenic trap operated at -130°C and two SAES™ GP50 getters (one at room temperature, one operated at 2.2A), is estimated at ~450 cc. A combination of turbo molecular pumps and ion pumps maintain steady pressures within the extraction line of < 1.33×10^{-7} Pa. Samples were incrementally heated in steps of 90 seconds, by controlled power output of a 50W CO_2 laser equipped with a beam homogenizing lens resulting in uniform energy over the entire sample surface. The reported incremental heating data represent results from individual mineral grains. During laser heating any sample gas released was exposed to the cryogenic trap and was further purified for an additional 120 seconds by exposure to both the cryogenic trap and the SAES getters. The sample gas was expanded into a Thermo Scientific ARGUSVI™ mass spectrometer and argon isotopes were analyzed simultaneously using four Faraday detectors (^{40}Ar, ^{39}Ar, ^{38}Ar, ^{37}Ar) and one ion counter (^{36}Ar). Following data acquisition of 10 minutes, time zero intercepts were fit to the data (using parabolic and/or linear best fits) and corrected for backgrounds, detector inter-calibrations, and nucleogenic interferences. The mass spectrometer computer program written by A. Deino of the Berkeley Geochronology Center was used for data acquisition, age calculations, and plotting. All ^{40}Ar/^{39}Ar ages reported in Table 2 are referenced to an age of 28.201 ± 0.046 Ma for the Fish Canyon sanidine (Kuiper et al., 2008), the decay constants of Min et al. (2000), and an atmospheric ^{40}Ar/^{36}Ar ratio of 298.56 ± 0.31 (Lee et al., 2006). Laser fusion of >10 individual Fish Canyon Tuff sanidine crystals at each closely monitored position within the irradiation package resulted in neutron flux ratios reproducible to ≤ 0.25% (2σ). Isotopic production ratios were determined from irradiated CaF_2 and KCl salts and for this study the following values were measured: $(^{36}Ar/^{37}Ar)_{Ca} = (2.4 \pm 0.05) \times 10^{-4}$; $(^{39}Ar/^{37}Ar)_{Ca} = (6.59 \pm 0.10) \times 10^{-4}$; and $(^{38}Ar/^{39}Ar)_K = (1.29 \pm 0.03) \times 10^{-2}$. Cadmium shielding during irradiation prevented any measurable $(^{40}Ar/^{39}Ar)_K$. ^{40}Ar/^{39}Ar plateau ages (and uncertainties) are considered the best estimate of the cooling age of the minerals and were calculated from samples if three or more consecutive heating steps released ≥ 50% of the total ^{39}Ar and also had statistically (2σ) indistinguishable ^{40}Ar/^{39}Ar ages.

Sr, Nd, Hf, and Pb isotope analyses

The analytical techniques used for Pb-Sr-Nd isotopic systematics on whole-rock powders at the USGS were similar to those reported by Tatsumoto and Unruh (1976) and more recently by Premo and Loucks

(2000) and Premo and Taylor (2010). The whole-rock powders were dissolved in 7 ml PFA Teflon^{TM} vials with ultrapure concentrated HF + HNO_3 while heating to ~150°C on a hot plate for at least 5 days. Lead was extracted from the dissolved effluent using AG 1-X8 anion-exchange resin in Teflon^{TM} columns and a very dilute HBr medium. The Pb laboratory contamination (blank) varied between 60 and 300 pg during the present analytical session. Strontium and REE were separated from the rest of the sample using a 30 ml volume cation-exhange column (Birck and Allègre, 1978), while Sm was separated from Nd using the α-isobutyric method of Lugmair et al. (1975). Strontium and Nd blanks were less than 300 pg each.

Lead, Sr, and Nd isotopic measurements were conducted using a Triton™ (Thermo-Fisher Scientific) 9-collector mass spectrometer which operates with a 10-kV acceleration voltage and 10^{11}-ohm resistors for the Faraday cups. Lead residues were re-dissolved in H_3PO_4 and loaded onto single Re filaments. The measured Pb isotopic ratios were corrected using the algorithms and programming of Ludwig (1980; 1985) for laboratory blanks with measured compositions of $^{206}Pb/^{204}Pb = 19.34 \pm 0.53$, $^{207}Pb/^{204}Pb = 15.53 \pm 0.08$, and $^{208}Pb/^{204}Pb = 38.11 \pm 0.20$, and instrumental mass fractionation (0.08 ± 0.03 % per a.m.u.) as determined from multiple runs of the NIST Pb standards SRM-981 and 982. Between 500 and 1000 ng of Sr and Nd were loaded separately on outgassed Re filaments with a Ta_2O_5 activator. Within-run 1 SE (standard error) values for conventionally fractionation-corrected isotope ratios using accepted $^{88}Sr/^{86}Sr = 8.375209$ typically were ~0.0004% for $^{87}Sr/^{86}Sr$ and ~0.002% for $^{84}Sr/^{86}Sr$ in un-spiked samples. Un-spiked NIST $SrCO_3$ standard SRM-987 was run after each five unknowns and its average value was used to determine a normalization factor (F) for measured $^{87}Sr/^{86}Sr$ values as F= $^{87}Sr/^{86}Sr_{Measured}$ / 0.710248. The long-term weighted average for the NIST-corrected $^{87}Sr/^{86}Sr$ in the USGS carbonate standard EN-1 (giant clam shell) was 0.709176 ± 0.000002 (n=31, MSWD = 0.82, probability of fit = 0.74). Measured $^{143}Nd/^{144}Nd$ data were normalized to $^{146}Nd/^{144}Nd = 0.7219$ and monitored for instrumental bias using the JNd-1 Nd standard (Tanaka et al., 2000). A mean $^{143}Nd/^{144}Nd$ value of 0.512087 ± 0.00006 (2SE%) was obtained during the same runs and an average of two JNdi-1 analyses is 0.512085 ± 0.0006 (2SE%).

Hafnium and duplicate Pb isotope analyses were performed at the Ecole Normale Supérieure in Lyon (ENSL) on the same whole rock powders as those for USGS chemical and isotopic analyses. In this case, ~600 mg of whole rock powder was leached in high-purity 6 M HCl in stages alternating between heating to 125°C and ultrasonication. The total duration of leaching was 50 minutes. The leachate was decanted and the residue washed repeatedly in ultrapure water before digestion in high-purity concentrated HNO_3 and HF in 1:3 proportions. After evaporation, Hf was leached from the digested residue using high-purity concentrated HF and separated first from the remaining sample matrix, then from Ti using a two-stage chromatographic procedure (Blichert-Toft et al., 1997). The Ca-Mg fluoride precipitate remaining after the HF-leaching step was dissolved in 6 M HCl and converted to bromides. Lead was separated and purified from this solution on a 50 µL AG 1-X8 anion-exchange column using dilute HBr to elute the sample matrix and 6 M HCl to elute the Pb.

Isotopic analyses were performed at ENSL on the Nu Plasma HR multiple-collector inductively coupled plasma mass spectrometer. Groups of two to four Hf isotope analyses were bracketed by analyses of the JMC-475 Hf standard. Results were normalized for instrumental mass fractionation using an exponential law relative to $^{179}Hf/^{177}Hf= 0.7325$. The JMC-475 Hf standard run in alternation in the session with the unknowns yielded $^{176}Hf/^{177}Hf =0.282158 \pm 0.000004$ (2 s.d.; n=11). Lead was analyzed using Tl doping (5 ppb) and sample-standard bracketing (White et al., 2000), wherein the NIST 981 Pb standard was systematically run after every second sample. Analyses were normalized to the values of Eisele et al. (2003). External 2σ reproducibility of ^{206}Pb/^{204}Pb, ^{207}Pb/^{204}Pb, and ^{208}Pb/^{204}Pb are ± 100-200 ppm (or 0.01-0.02 %), while those of ^{207}Pb/^{206}Pb and ^{208}Pb/^{206}Pb are ± 50 ppm (or 0.005%). Internal run errors on all Pb isotope ratios were better than the external reproducibility. Hafnium and Pb blanks were <20 pg. The Sr, Nd, Hf, and Pb isotope data are listed in Table 3.

Results

Rock geochemistry

Major and trace element compositions of samples collected from both the Toprakkale and Karasu volcanic fields support previous analyses (e.g., Polat et al., 1997; Yurtmen et al., 2000; Alıcı et al., 2001; Nikogosian et al., 2018; Oyan, 2018) noting a limited range of rock type from alkaline basalt to basanite (Fig. 3), with basanite only reported from the Toprakkale volcanic field (this and previous studies). Relative to primitive mantle compositions, all samples from this study (Fig. 4) and other studies (Fig. 5) have compositions that are enriched in LILE and LREE, and share more similarities to OIB. CIPW normative mineralogy calculations indicate that the basanites are nepheline-normative, and petrographic inspection of the samples reveals fresh basalts with phenocrysts of olivine and clinopyroxene in a matrix of plagioclase and iron-titanium oxides (Fig. 6). Some samples preserve fresh glass and vesicles, and the basanite samples are notably coarser grained than any of the alkaline basalts collected in this study.

Sr, Nd, Hf, and Pb isotope geochemistry

The two basanites analyzed from the Toprakkale volcanic field have the following isotopic ratios: $^{87}Sr/^{86}Sr$ of 0.703070 and 0.703136; $^{143}Nd/^{144}Nd$ of 0.512931 and 0.512893 (ε_{Nd} = +5.8 to +5.0); $^{176}Hf/^{177}Hf$ of 0.283019 and 0.282995 (ε_{Hf} = +8.7 to +7.9); $^{206}Pb/^{204}Pb$ of 19.087 and 19.155; and $^{208}Pb/^{204}Pb$ of 38.861 and 38.915, where the Pb isotope values are averages of those obtained at the USGS and ENSL. $^{143}Nd/^{144}Nd$ and $^{87}Sr/^{86}Sr$ for Toprakkale basanites (Parlak et al., 2000; Bağcı et al., 2011; this study) are among the highest and lowest values, respectively, when compared to Miocene mafic Anatolian lavas (cf. compilations by McNab et al., 2018 and Uslular and Gençalioğlu-Kuşcu, 2019a) (Fig. 7). They also overlap those of the most isotopically depleted Miocene basalts in northern and central Arabia, albeit displaced to slightly lower $^{87}Sr/^{86}Sr$. Plots of $^{176}Hf/^{177}Hf$ and $^{143}Nd/^{144}Nd$ lie within the distribution of oceanic mantle compositions defined by MORB and OIB (deviation from the mantle array, $\Delta\varepsilon_{Hf}$, of –2) (Fig. 7), and resemble those of Late Miocene basalts of western Anatolia (Aldanmaz et al., 2015). Lead isotope signatures lie close to, but above, the Northern Hemisphere Reference Line (NHRL; Hart, 1984) in $^{207}Pb/^{204}Pb$-$^{206}Pb/^{204}Pb$ and $^{208}Pb/^{204}Pb$ -$^{206}Pb/^{204}Pb$ space (Δ7/4 deviations of ~5 and Δ8/4 of ~15) (Fig. 7), similar to those of Miocene basalts from Northern and Central Arabia as well as those of Late Miocene and Quaternary basalts in Western Anatolia.

Alkaline Toprakkale basalts have somewhat higher $^{176}Hf/^{177}Hf$ ratios (0.282966 to 0.283019; ε_{Hf} = +6.9 to +8.7) than alkaline Karasu basalts (0.282837 to 0.282965; ε_{Hf} = +2.3 to +6.8) and somewhat higher $^{143}Nd/^{144}Nd$ ratios (0.512781 to 0.512866 and ε_{Nd} = +2.8 to +4.5, versus 0.512648 to 0.512806 and ε_{Nd} = +0.2 to +3.3). Plots of $^{176}Hf/^{177}Hf$ and $^{143}Nd/^{144}Nd$ values lie within the oceanic mantle array ($\Delta\varepsilon_{Hf}$ of ~ –2.1 to +0.4) (Fig. 7), in this respect resembling Late Pliocene and Quaternary basalts of western Anatolia (Aldanmaz et al., 2015) in contrast to contemporaneous near-primary basalts in central Anatolia with similar Nd isotope ratios which are displaced to ε_{Hf} values ~6 units higher (Reid et al., 2017). $^{206}Pb/^{204}Pb$ for alkaline Toprakkale basalts are relatively invariant (19.025 ± 0.001), whereas those for Karasu basalts vary from 18.800 to 19.324; $^{208}Pb/^{204}Pb$ ratios overlap but are displaced to lower values in Toprakkale basalts (38.978 to 39.103) relative to the Karasu basalts (39.101 to 39.219). More generally, Pb isotope ratios extend to values well above the NHRL in $^{207}Pb/^{204}Pb$-$^{206}Pb/^{204}Pb$ and $^{208}Pb/^{204}Pb$ - $^{206}Pb/^{204}Pb$ space (Δ7/4 up to 17 and Δ8/4 up to 75) (Fig. 7). Although there is some overlap in radiogenic isotope ratios, the combined data highlight differences between the two Quaternary volcanic fields, with the Toprakkale basanites displaying the most distinct and restrictive mantle signatures.

$^{40}Ar/^{39}Ar$ geochronology

The $^{40}Ar/^{39}Ar$ geochronological data from this study constrain alkalic basalt volcanism in the Toprakkale and Karasu volcanic fields to between 46 ± 13 ka and 2.63 ± 0.17 Ma (Fig. 8). The Delihalil volcano is the most prominent edifice in the Toprakkale volcanic field, with $^{40}Ar/^{39}Ar$ plateau ages (2σ errors throughout) of 46 ± 13 ka (R12-OS1) and 50 ± 20 ka (R12-OS3) determined from basanites collected near and just below the summit, respectively. The young Delihalil volcanic edifice erupted onto alkaline basalt lavas dated at 750 ± 90 ka (R12-OS4), with similar ages of 810 ± 60 ka (R12-OS5) and 780 ± 60 ka (R12-OS6) determined from samples collected along the northern margin of the Gulf of İskenderun; all three of these samples have identical geochemical and petrographic characteristics, despite being collected 30 km apart.

In the Karasu volcanic field, the basalt (R12HA-01) flow exposed in the creek bed near the village of Hassa produced a $^{40}Ar/^{39}Ar$ plateau age of 2.63 ± 0.17 Ma. A basalt lava flow (R12HA-02) from overlying lavas exposed in the creek bed produced the youngest basalt dated from the Karasu volcanic field with a $^{40}Ar/^{39}Ar$ plateau age of 52 ± 16 ka. A lava flow toward the northern end of the Karasu volcanic field near the village of Fevzipaşa records a $^{40}Ar/^{39}Ar$ plateau age of 230 ± 30 ka (R12HA-03).

Discussion

Magma sources and melt equilibration depths: Toprakkale basanites

The Hf and Pb isotope compositions obtained for Toprakkale basanites, considered together with Sr and Nd isotope data, provide important new constraints on their mantle source(s). New and published Sr isotope data for Toprakkale basanites exhibit minor variability (average $^{87}Sr/^{86}Sr$ = 0.70315 ± 0.00007 (1 sd); n=14) despite approximately two-fold variations in La/Nb, La/Yb, and Ba/Nb. Helium isotope values averaging $R/R_a = 7.6 \pm 0.3$ obtained for five Toprakkale basanites are indistinguishable from those of MORB mantle (Italiano et al., 2017). More generally, the isotopic features of the Toprakkale basanites, and specifically the Hf and Pb isotopic data reported here, lie within mantle arrays defined by the isotopic characteristics of oceanic basalts, and close to those with a common mantle component (“C”; Hanan and Graham, 1996). As noted by several authors (Polat et al., 1997; Alıcı et al., 2001; Yurtmen, 2002; Oyan, 2018; Nikogosian et al., 2018), the incompatible element characteristics of the basanites resemble those of OIB. Thus, both isotopic and incompatible element characteristics of the Toprakkale basanites indicate that they are OIB-type, asthenosphere-derived melts largely unmodified by crustal contributions.

Basanites could be derived by partial melting of garnet pyroxenite (Keshav et al., 2004), hornblende peridotite (Pilet et al., 2008) or, in this study area specifically, phlogopite-bearing garnet peridotite (Oyan, 2018). The latter source was identified for Toprakkale basalts based on the apparent buffering of alkalis and alkaline earths relative to the LREE during melting. Depths of peridotite-derived melt equilibration can be estimated using olivine-orthopyroxene-melt barometry (Lee et al., 2009; Plank and Forsyth, 2016). Relevant conditions for melt equilibration are assumed to be: (1) primary melts in equilibrium with a Fo_{89} source (a fairly conservative estimate judging by Arabian mantle xenoliths; Stern and Johnson, 2010); (2) minimum water contents given by H_2O (ppm) = 200•Ce (ppm), a relation typical for oceanic basalts (Reid et al., 2017); and (3) $Fe^{2+}/\Sigma Fe = 0.18$ and 0.16 for the basanites and basalts, respectively, extrapolated based on estimated water contents (Kelley and Cottrell, 2009). Barometer uncertainty is ± 8 km (Plank and Forsyth, 2016). Basanites were filtered for Mg# ≥ 55 and $CaO/Al_2O_3 > 0.6$, since those with lower values are more likely to have experienced clinopyroxene fractionation (Italiano et al., 2017).

Pressure estimates for basanite melt equilibration with peridotite derived from new and published chemical analyses average 2.7 ± 0.2 GPa (n=31; data in supplementary table, S1), corresponding to a mean depth estimate of 91 ± 3 km, assuming an average crustal thickness of 30 km as indicated by seismic data (Abgarmi et al., 2017). The ~90 km depth estimate for melt equilibration is consistent with REE and HFSE evidence for Toprakkale basanite generation in the garnet stability field (Oyan, 2018; Nikogosian et al., 2018). The corresponding equilibration pressure is within 0.3 GPa of values reported previously (Çoban, 2007; Reid et al., 2017; Nikogosian et al., 2018) albeit for a larger number of samples and with differing assumptions about primary melt compositions. These pressure estimates are considerably lower than the value of 3.7 GPa estimated by Oyan (2018) using the barometer formulation of Lee et al. (2009). Much of this difference is probably attributable to different barometer formulations. Inferred water contents are 1.0 to 1.6 wt.% but could be higher if the source is more hydrous than typical sub-oceanic mantle. Increasing water contents by a factor of two, for example, reduces the depth estimate by only 2 km. Allowing for an uncertainty in $Fe^{2+}/\Sigma Fe$ of ± 0.05 (likely a maximum) would increase the depth uncertainty by ± 4 km.

Magma sources and melt equilibration depths: Toprakkale and Karasu basalts

The isotopic and enriched trace element compositions of basalts from the Toprakkale and Karasu volcanic fields have been variously ascribed to subduction-modified sources (Yurtmen et al., 2000; Italiano et al., 2017), mantle signatures overprinted by crustal contributions (Alıcı et al., 2001; Oyan, 2018), and mantle source heterogeneity (Nikogosian et al., 2018). The elevated $^{207}Pb/^{204}Pb$ and $^{208}Pb/^{204}Pb$ of the basalts could, by analogy with Miocene Central Anatolian basalts, reflect metasomatism of the lithosphere by a subduction-related component. However, the basalts are largely characterized by positive HFSE anomalies (e.g., $La/Nb_N = 0.6$ to 0.9) (Fig. 4) in contrast to the pronounced negative anomalies in relatively primitive subduction-influenced Miocene basalts from Central Anatolia (La/Nb_N mostly >2) (Reid et al., 2017; Uslular and Gençalioğlu-Kuşcu, 2019b). The oceanic mantle array-like Hf-Nd isotopic characteristics of Toprakkale and Karasu basalts also contrast with Hf isotope signatures that are displaced from the oceanic mantle array in Central Anatolian basalts (Reid et al., 2017). Instead, incompatible element patterns for the triple junction basalts are broadly similar to, albeit at lower abundances than, the basanites, as permitted if the basalts were generated by a greater degree of melting (Bağcı et al., 2011; Oyan, 2018).

The variations in new Hf, Δ7/4, and Δ8/4 isotope constraints along with new and previously determined Sr and Nd isotope ratios additionally require either source heterogeneity and/or contributions from more than one source. Paired isotope ratios from both volcanic fields define broadly linear arrays that trend from the basanites to the most evolved basalt, even though they span locations in two different volcanic fields (Fig. 7). The more enriched isotopic compositions of the alkaline Toprakkale basalts relative to the basanites could be the result of 2–5% crustal assimilation (Oyan, 2018), with olivine-normative basalts displaced even further in Nd and Hf isotope space. The somewhat different isotopic trends defined for the two volcanic fields would require different crustal endmembers if arising from crustal assimilation.

In detail, interelement ratios for the basalts (compiled data) and olivine-hosted melt inclusions (Nikogosian et al., 2018) in the Toprakkale volcanic field are more MORB-like than the basanites, an observation that is not easily reconciled with crustal assimilation. This has led to the hypothesis that at least some of the trace element heterogeneity exhibited by the basalts is derived from a more MORB-like mantle source than that of the basanites (Nikogosian et al., 2018), although the more enriched Sr, Nd, and Hf isotope signatures of the basalts do not support this interpretation.

Pressure estimates obtained for the Toprakkale and Karasu basalts assuming melt equilibration with peridotite average 1.9 ± 0.1 (n=26) and 1.8 ± 0.3 (n=15) GPa, respectively (data filtered as described above). These correspond to average depth estimates of 64 ± 4 km and 63 ± 8 km, or approximately 30 km shallower than those for the basanites. Such pressures are similar to those of 1.8 to 2.3 GPa and 2.05 to 2.17 GPa obtained in previous investigations (Reid et al., 2017; McNab et al. 2018; Nikogosian et al., 2018) and imply depths in the spinel peridotite stability field, contributions from which have been identified by other authors (Italiano et al., 2017; Oyan, 2018). Contributions from melting in the presence of garnet are also apparent from REE and HFSE systematics (Bağcı et al., 2010; Nikogosian et al., 2018), and are likely inherited as melt upwelled from depth; the "garnet-signatures" would not be erased by equilibration or mixing with more shallowly derived melts. Inferred water contents are from 0.6 to 1.4 wt.%.

Reconciling melt equilibration depths with geophysical images of mantle structure

Data from this and other studies show that the Toprakkale and Karasu volcanic fields were derived by partial melting of an oceanic basalt-like asthenospheric mantle source (basanites) with possible contributions from a lithospheric mantle ± crustal source (basalts). However, observed geochemical and isotopic variations between the volcanic fields may also be impacted by the regional tectonic complexities of an evolving triple junction, perhaps explaining why alkaline basalts occur in both volcanic fields while basanites have only been described from the Toprakkale volcanic field. Moreover, the melting depths inferred for the Toprakkale basanites are not only the deepest from either volcanic field but are also restricted to an area of transtension between strands of the EAFZ. The basanites are the most primitive in terms of Sr, Nd, Hf, and Pb radiogenic isotope data, with low overall variability compared to the less mafic rocks from both the Karasu and Toprakkale volcanic fields. The compositions of the basanites support relatively deep melting (mostly 80 to 105 km, averaging ~90 km) in contrast to the alkaline basalts that are mostly 60-70 km (Polat et al., 1997; Yurtmen et al., 2000; Bağcı et al., 2011; Oyan, 2018).

Large variations in crustal and upper mantle seismic structure are found near the A^3 triple junction. Using P-wave receiver functions, Abgarmi et al. (2017) imaged a significant decrease in crustal thickness at the transition from the Central Taurus Mountains (>40 km) to the Adana Basin (~30 km). This thinning is likely due to the extensional component of the dominantly transtensional northern strand of the EAFZ. Combining Rayleigh wave dispersion measurements to the receiver function measurements of Abgarmi et al. (2017) and jointly inverting to solve for the 3D shear-wave velocity structure of central Anatolia, Delph et al. (2017) observed a widespread and vertically-extensive fast shear-wave velocity anomaly beneath the central Taurus Mountains and western Adana Basin, interpreted as the underthrusted Cyprean slab. These fast velocities abruptly terminate near the central Adana Basin, transitioning to very slow upper mantle shear velocities beneath the Iskenderun Basin and areas farther east (< 4.2 km/s at >60 km; Fig. 9). These observations are consistent with thin crust (~30 km) and thin mantle lithosphere (~30 km) underlain by a hot and shallow melt-bearing asthenosphere beneath the A^3 triple junction that extends beneath the Arabian plate.

Melt equilibration depths for Quaternary basaltic magmatism in the Toprakkale and Karasu volcanic fields agree with the shallowest depths of very slow upper mantle shear velocities, and depths that define the base of the seismically-imaged lithosphere (Fig. 9). A general (mostly within 5 km) co-occurrence between melt equilibration and seismically-defined lithosphere-asthenosphere boundary (LAB) depths has also been observed elsewhere in Turkey (Reid et al.,

2017) and in the western USA (Reid et al., 2012; Plank and Forsyth, 2016). It can be explained by partial melts being able to segregate from upwelling mantle as the relatively rigid lithospheric lid is approached. Chemical and isotopic heterogeneity exhibited by these basalts would therefore reflect hybridization of asthenosphere-derived melts with lithosphere that is being thermally and chemically eroded, except where arising from crustal contamination

The relatively thin lithosphere (~50–60 km) below the İskenderun Basin extends farther to the east beneath the Arabian foreland (Angus et al., 2006; Delph et al., 2017) and is much thinner than the Arabian shield farther to the south, which has a lithospheric thickness of >100 km (Hansen et al., 2007). The comparatively thin Arabian foreland lithosphere may represent its original thickness as a continental passive margin prior to collision. Another possibility is that thinning and lateral erosion of the Arabian mantle lithosphere is occurring through an asthenospheric mantle erosion process, which could be linked to crustal tectonics and magmatism along the EAFZ. For example, northward mantle flow beneath the Arabian plate (Becker and Faccenna, 2011) coupled with the abrupt decrease in lithospheric thickness from >100 km to ~60 km could indicate shear-induced, edge-driven convective erosion of the mantle lithosphere (e.g., Kaislaniemi and van Hunen, 2014). Such edge-driven convection may provide a mechanism for adiabatic decompression melting of mantle that has entrained blocks of detached lithosphere, explaining the occurrence of localized small-volume basalts along the high-angle plate boundary faults (EAFZ) and also their geochemical and isotopic variations. Similarly, the Quaternary-recent mafic magmatism in the Karacadağ volcanic field in the Arabian foreland farther east (e.g., Lustrino et al., 2010; Ekici et al., 2014; Ekici and Macpherson, 2019) may also result from such a process, supporting regional-scale mantle lithospheric erosion of the Arabian foreland, extending into the A^3 triple junction. Indeed, magmatism at the Karacadağ volcanic field extends back to ~17 Ma (Ekici and Macpherson, 2019), showing a minor southeastward migration through time along a major regional fault (Keskin et al., 2012), consistent with edge-driven convective removal of mantle lithosphere.

The considerably deeper melt equilibration depths obtained here and in previous investigations of the Toprakkale basanites (~90 km; Reid et al., 2017; Oyan, 2018; Nikogosian et al., 2018) appear to require a different process of melt generation. The basanites could be melts of an oceanic basalt-like sub-lithospheric mantle source, as supported by the Pb and Hf isotope data reported here and recognized previously; they appear to define one end-member for the basalts (Fig. 7). Basanite melts could simply have separated from mantle upwelling along an adiabat at depths greater than the LAB, as observed in the Western Grand Canyon region of the western USA and proposed for the Sivas region of Central Anatolia (Plank and Forsyth, 2016; Reid et al., 2019).

A signature feature of the basanites is their depletions of alkalis and Pb relative to similarly incompatible elements, a signature that is also observed in basanites attributed to HIMU (high μ)-OIB mantle sources (Fig. 4; Bağcı et al., 2011; Oyan, 2018; Nikogosian et al., 2018). Basanites from oceanic islands that exhibit similar geochemical characteristics (e.g., St. Helena, Cook-Austral islands) are inferred to be derived from upwelling mantle plumes. The lack of high (>20) $^{206}Pb/^{204}Pb$ (or HIMU) in the Toprakkale basanites would reflect insufficient time for radiogenic ^{206}Pb ingrowth after recycling of oceanic crust into the plume source. Alternative origins have, however, been proposed for HIMU signatures regionally. Specifically, basanites erupted in the Toprakkale volcanic field and other localities in the Anatolia-Arabia region have been ascribed to melting of hydrous metasomatic veins impregnated within, or at the base of, the lithosphere or by reactive porous flow of melts migrating through the lithosphere (Bağcı et al., 2011; Aldanmaz et al., 2006; Oyan, 2018). For these scenarios, seismological constraints on the LAB under the Toprakkale volcanic field lead to expected melt equilibration depths similar to or less than those of the basalts (≤60 km). We therefore consider three alternatives: 1) the basanite melts were generated by heating of suspended blocks within the asthenopheric mantle that delaminated/dripped from the base of the lithosphere; 2) geochemical signatures of the nearby Cyprean slab mantle lithosphere were incorporated near the source (Fig. 9); or 3) the pressure estimates for basanite melt equilibration are invalid. Regarding the last, melt equilibration depths could be in error if the source lithology lacked orthopyroxene and/or olivine (e.g., if it were a pyroxenite) or if there were considerable pyroxene fractionation after melt extraction. Previous investigations (e.g., Oyan, 2018) and our data filtering suggest that neither scenario applies here.

Assuming the melt generation depths of ~ 90 km are reliable, the basanites from the Toprakkale volcanic field are sourced from ~ 30 km greater depths than the LAB. Although it is possible to invoke some component of a laterally eroded and deeper, subducted Cyprian slab as a potential source area due to its proximity (Fig. 9), there is no a priori reason to believe that such a source would impart HIMU-like trace element signatures on the basanites. Indeed, given the abrupt contrast in seismically imaged lithospheric thicknesses and distribution of Quaternary basalts within the Arabian foreland (e.g., Chorowicz et al., 2005; Stern and Johnson, 2019), it seems likely that the spatially restricted basanites represent melts sourced from lithospheric blocks previously detached by vigorous mantle convection and mechanical erosion at the base of the lithosphere beneath the Arabian foreland.

Plate boundary volcanism and tectonic escape of Anatolia

The combined K-Ar and $^{40}Ar/^{39}Ar$ ages indicate that the initial stages of volcanism began in the Toprakkale and Karasu volcanic fields with first appearances of alkaline volcanism at 2.25 ± 1.56 Ma (2 sd, Arger et al., 2000) and 2.63 ± 0.17 Ma (this study), respectively. These results are consistent with the K-Ar dating results of Rojay et al. (2001) but also indicate that basaltic volcanism in the Karasu valley began by 2.63 Ma, nearly 1 Ma earlier than previously known from imprecise K-Ar data. The new $^{40}Ar/^{39}Ar$ data from this study support a semi-continuous 2.5 Ma history of volcanism within the Karasu valley, consistent with borehole data showing intercalated basalt and fluvial-lacustrine sedimentation with significantly more sedimentation occurring along the western margin of the valley (Rojay et al., 2001). The 46 ± 13 ka basanite lava erupted from the Delihalil volcano, and the 50 ± 20 ka alkaline basalt lava flow in the Karasu valley also demonstrate that volcanism remains active in both the Toprakkale and Karasu volcanic fields. The initial period of volcanism in both volcanic fields was limited, as only one sample from each area records evidence of volcanism prior to 2 Ma, which provide the earliest evidence of magmas erupted along developing fault boundaries (Fig. 10). However, between 2 and 1 Ma, more widespread basaltic volcanism was localized along the Karasu fault zone and along the Yumurtalık fault zone in the Karasu and Toprakkale volcanic fields, respectively. Over the last 1 Ma, volcanism appears to have intensified and produced most of the exposed volume of volcanic rocks within both volcanic fields. These post-1 Ma volcanic rocks are focused within larger eruption centers such as the Delihalil volcano in the Toprakkale volcanic field and a number of smaller volcanic cones within the Karasu volcanic field along clearly defined fault segments. Although poorly constrained, there is some indication that volcanism within the Karasu volcanic field may have migrated toward the Arabian plate over the last 200 ka (Fig. 10).

Important questions in understanding the tectonic evolution of the A^3 triple junction are: (1) when did the modern fault systems bounding the triple junction become active, and (2) can the Quaternary lavas associated with the fault system provide chronological constraints on fault dynamics? Given that Quaternary volcanism is clearly localized along fault segments and releasing- and restraining-bends of the EAFZ (Tatar et al., 2004; Kavak et al., 2009), it seems likely that volcanism postdates initiation of major strike-slip activity related to Anatolian tectonic escape and, based on our new results, associated magmatism did not occur until 2.63 ± 0.17 Ma. While this provides a lower limit on tectonic escape of the Anatolian microplate along the western terminus of the EAFZ, others have suggested initiation of the EAFZ by ~4 Ma and possibly as early as 7 Ma near the Gulf of İskenderun (e.g., Westaway, 2003, 2004; Seyrek et al., 2008). A reasonable upper limit to the inception of the EAFZ is probably a few million years greater than the $^{40}Ar/^{39}Ar$ basalt ages judging from estimates of the time required for initial melt generation and transfer of melts through the crust (Cesare et al., 2009; Ferrari, 2004; Karakas et al., 2017). These estimates agree with independent geologic evidence supporting the transition from regional transpression to transtension and from "proto-escape" to active escape of the Anatolian plate along the EAFZ around 5 Ma (e.g., Yilmaz et al., 2006; Brocard et al., 2020).

Plate reorganization and triple junction initiation and migration

Prior to the late Miocene, a collisional plate boundary existed between Eurasia (Anatolia) and Nubia (Africa-Arabia), expressed geologically in the field by imbricated Kızıldağ and Baer Bassit ophiolite sequences (Bitlis suture). However, during the late Miocene, a combination of a detached Cyprean slab (e.g., Portner et al., 2018) and rifting within the greater Red Sea rift (e.g., Bosworth and Stockli, 2016), led to development of the DSFZ (Africa-Arabia) and the EAFZ (Anatolia-Arabia) transform faults and A^3 triple junction plate boundaries. The inception and continuing development of the A^3 triple junction plate boundaries is intimately tied to the evolving DSFZ-EAFZ fault system and how these faults respond to deformation related to tectonic escape of the Anatolian plate. Extrusion of the Anatolian plate since 5 Ma, currently moving at 21 mma^{-1} and partly driven by the 15 mma^{-1} advance of Arabia and its collision with Eurasia (e.g., Reilinger et al., 2006), is continuing to apply pressure (tectonic coupling) to the more slowly (5 mma^{-1}) advancing African plate.

Although transfer of left-lateral deformation from the DSFZ to the EAFZ is fairly well accepted and the EAFZ represents a major component of the A^3 triple junction, less well known is the offshore linkage of the northern EAFZ to the Kyrenia-Misis fault and how the main strand of the EAFZ links to the Cyprus trench (e.g., Duman and Emre, 2013). The exposed broad zone of distributed deformation, transtension, and basin development between the two main strands of the EAFZ clearly continues offshore, represented by the Adana-Cilicia and İskenderun basins. Indeed, continuing rollback of the Cyprean slab and associated trench retreat may explain some of the plate kinematics, including the location and possible migration of the triple junction and the occurrence of mafic magmatism associated with the A^3 triple junction.

We suggest that initiation of the triple junction at a position near the village of Kahramanmaraş began around 5 Ma, and subsequently migrated to the southwest to its current position near the Amik Basin (Fig. 11). This interpretation is consistent with an overall southwesterly shift in the locus of deformation along the EAFZ toward areas containing young and shallow basins. This interpretation also implies that plate segmentation within the lithosphere may not correspond to exposed crustal sequences representing former plate positions. For example, the trend of pronounced seismicity west of Kahramanmaraş (e.g., Duman and Emre, 2013) could represent either a zone of previous weakness or one of incipient faulting. Coincident with the A^3 triple junction migration was the linked migration of the Africa–Anatolia plate margin and a jump of the Cyprean trench to its current southerly position (Fig. 11). Geologic evidence for such a model within the Adana Basin includes the abrupt termination of late Miocene compressional (Bitlis suture) sedimentation features and the establishment of Pliocene and younger high angle translational faults and extensional/transtensional basins (e.g., Burton-Ferguson et al., 2005). Such a model is also consistent with a period of major Pliocene surface uplift within Cyprus (e.g., McCallum and Robertson, 1995; Kinnaird et al., 2011). This < 5 Ma plate margin jump follows the retreating Africa plate, and at least locally, along the advancing Anatolia plate margin, where the slab pull force was eliminated following detachment of the Cyprean slab (e.g., Portner et al., 2018). Cyprean slab detachment was a major factor driving the post-8 Ma surface uplift of the Taurus Mountains (e.g. Cosentino et al., 2012; Schildgen et al., 2012; Meijers et al., 2020). The same or similar tectonic forces responsible for the partial uplift of Cyprus will ultimately lead to future uplift of the Eratosthenes seamount.

Plate boundary reorganization from 5 Ma to present would have modified the regional deformation and the state of stress and promoted the tapping of sublithospheric melt along extensional/transtensional pathways (Fig. 11). African slab rollback and the southwesterly migration of the A^3 triple junction is not only consistent with establishment of the southern strand of the EAFZ as a primary plate boundary, it is also similarly consistent with mafic volcanism. The spatially restricted occurrence of Quaternary basalts between the current and former position of the A^3 triple junction suggests that the migration of the triple junction, in this case associated with trench migration (or jump), triggered deeply-sourced volcanism. Tectonic conditions favor continued migration of the A^3 triple junction along the Dead Sea transform fault as rollback of the African slab proceeds and the Anatolia-Africa-Arabia plate boundaries continue to evolve.

Summary

From 5 Ma to the present day, thin lithosphere and high heat flow have resulted in several volcanic fields near the margin of the Arabian plate and its borders with Africa and Anatolia (e.g., Chorowicz et al., 2005; Delph et al., 2017; Stern and Johnson, 2019). This regional volcanism began developing at ~4.5-5 Ma along the northwest collisional margin of Arabia with Eurasia (Ekici and Macpherson, 2019) and is consistent with geologic evidence that, at this time, the EAFZ was already linked to the DSFZ and active as a major bounding fault in the tectonic escape of the Anatolian microplate (Yilmaz et al., 2006; Brocard et al., 2020). Tectonic escape of the Anatolian plate combined with rollback of the African slab has resulted in a migrating triple junction and plate boundary that includes the areas between strands of the EAFZ and their projections toward Cyprus.

Most of the Quaternary volcanic rocks erupted along, or between strands of the EAFZ and near the A^3 triple junction have melt equilibration depths of ~60 km, consistent with the seismically imaged depth of the LAB. The Toprakkale basanites are the only exceptions and appear to originate from a deeper (~90 km) source that could be upwelling mantle or may represent melting of detached fragments of mantle lithosphere foundering at greater depths within the asthenospheric mantle. A mafic lava with a $^{40}Ar/^{39}Ar$ plateau age of 2.63 ± 0.17 Ma represents the earliest stage of volcanism within the Toprakkale and Karasu volcanic fields associated with the developing A^3 triple junction. This time period is consistent with other data from the study area and from nearby areas such as the Karacadağ volcanic field (e.g., Ekici and Macpherson, 2019) supporting an increase in magmatic activity from 2 Ma. Episodic eruption of lavas in the last 2.6 Ma along discrete segments of the EAFZ clearly demonstrates that volcanism is being localized along the transform faults related to the A^3 triple junction. The DSFZ and EAFZ plate boundaries are high-angle shear zones that likely penetrate into the mantle lithosphere, providing the “leaky” conduits along which melts infiltrate to reach the surface. The spatially restricted distribution of basalts proximal to the A^3 triple junction indicates the potential for a causal relationship, as they occur within a zone of transtension near the triple junction and are not more widespread along the length of the EAFZ.

Acknowledgments

This study was partially funded with collaborative support of the National Science Foundation as part of the Continental Dynamics program (NSF/EAR-1109762 and 1109826). We thank Nuretdin Kaymakçı for fruitful scientific discussions and introducing some of us to the field area. We also thank Gilles Brocard for maps and scientific discussions. Any use of trade, product, or firm names is for descriptive purposes only and does not imply endorsement by the U.S. Government.

FIGURE CAPTIONS

Figure 1. Regional tectonic map of the eastern Mediterranean illustrating major tectonic elements, relative fault displacements, and relative plate motions. Faults in red represent approximate those associated with the tectonic escape and subduction of the Anatolian plate. Faults in black are active and related to regional stress patterns associated with motions of the African, Arabian, and Anatolian plates relative to a stable Eurasia. Dominant motions of the tectonic plates and their relative motions illustrated by large blue arrows. Box inset shows location of Figure 2A, which is also the general area defined by the A^3 triple junction. Modified from Holzer (2000).

Figure 2. A) Regional digital elevation map including major geologic and tectonic elements of the study area. Samples from this investigation were collected from Quaternary volcanic deposits of the Toprakkale and Karasu volcanic fields, which are approximately located and highlighted in yellow. The Eastern Anatolian fault zone (EAFZ) is shown in red. The shaded green area represents the exposed imbricated late Cretacous ophiolite and over-thrusted Miocene carbonate rocks of the former collisional margin between the Nubian (Arabia-Africa) and Eurasian (Anatolia) plates. The numbers are keyed to the following: (1) main southern strand of the EAFZ; (2) northern strand of the EAFZ; (3) Dead Sea fault zone (DSFZ); (4) Karataş fault: (5) Yumurtalık fault; (6) limit of late Cretaceous to late Miocene collisional front (Bitlis suture); (7) Yesemek (East Hatay) fault; (8) Aeferin fault; (9) Central Anatolian (Ecemis) fault; (10) Kyrenia- Misis fault zone; (11) area of fault transition to the Cyprean arc. Note the transition of the DSFZ to the EAFZ near the Amik Basin. The Karasu (Amanos) fault segment (KF) of the

EAFZ is indicated, where it runs along the base of the Amanos Mountains on the west side of the Karasu Basin. B) Inset from figure 2A showing sample locations and the overall distribution of major faults and Quaternary volcanic rocks between the main and northern strands of the EAFZ. Samples from the Karasu volcanic field occur within the Amik sub-basin of the Karsu rift (basin,) where the DSFZ transitions to the EAFZ. The transtenssional nature of the field area is expressed by major basin development including the Karasu, Amik, İskenderun, and Narli basins, and transpression expressed by uplift of the Amanos Mountains. The Toprakkale volcanic field includes all Quaternary volcanic rocks of the Ceyhan (location on Figure 9) -Osmaniye (O) -Erzin (E) -Toprakkale (T) and immediately surrounding areas. Samples R12OS-1 and R12OS-3 are located near the summit of the Delihalil volcano. Samples from the Karasu volcanic field (R12HA-1 through R12HA-3) are associated with different segments of the Karasu fault segment of the EAFZ.

Figure 3. Plot of compiled rock compositions from the Toprakkale and Karasu volcanic fields on a total alkali versus silica (TAS) diagram (after Le Maitre et al., 1989). Data from this study are solid colors (green triangles = basanite from Delihalil; orange squares = alkali basalt from Toprakkale; blue diamonds = alkali basalt from the Karasu volcanic field). Black symbols are data from cited literature. Shaded fields show compositional ranges for the Toprakkale (light blue) and Karasu (light orange) volcanic fields.

Figure 4. Primitive mantle-normalized (McDonough and Sun, 1995) incompatible trace element diagrams for samples analyzed in this study comparing Toprakkale basanites, Toprakkale basalts, and Karasu basalts.

Figure 5. Primitive mantle-normalized (McDonough and Sun, 1995) incompatible trace element diagrams for (A) Toprakkale basanites, (B) Toprakkale basalts, and (C) Karasu basalts. Fields show literature data, with some anomalous results excluded (Zr in three basalts where Zr/Hf <16 and Nb in two basalts where Nb/Ta ≤11). Data sources are Oyan (2018), Nikogosian et al. (2018), and summary by Uslular and Gençalioğlu-Kuşcu (2019a).

Figure 6. Photomicrographs of selected samples from the Toprakkale and Karasu volcanic fields. A) and B) are basanites from the Delihalil volcano (R12-OS3 and R12-OS1), C) and D) are alkali basalts from along the Yumurtalık fault (Botaş) (R12-OS5 and R12-OS6), and E and F are alkali basalts from near Hassa and İslahiye (R12-HA2 and R12-HA3). Note the glassy, vesicular (v) groundmass and euhedral-subhedral skeletal olivine (ol) phenocrysts in the basanites (A and B) versus the large euhedral olivine (ol) and plagioclase (pl) phenocrysts in the intergranular groundmass of the alkali basalts.

Figure 7. Plots of (A) $^{143}Nd/^{144}Nd$ versus $^{87}Sr/^{86}Sr$, (B) ε_{Hf} versus ε_{Nd}, (C) $^{207}Pb/^{204}Pb$ versus $^{206}Pb/^{204}Pb$, and (D) $^{208}Pb/^{204}Pb$ versus $^{206}Pb/^{204}Pb$ for samples from the Toprakkale and Karasu volcanic fields. Darker large symbols with black margins are from this study (see legend and Figure 3), lighter large symbols with colored margins are from Arger et al. (2000), Parlak et al. (2000), Alıcı et al. (2001), Bağcı et al. (2011), and Oyan et al. (2018). Also shown are comparative data of mainly Miocene rocks for Central Anatolia (Şen, et al., 2004; Reid et al., 2017; Uslular and Gençalioğlu-Kuşcu, 2019b) and locations in Northern Arabia: Karacadağ (small diamonds: Pearce et al., 1990; Şen, et al., 2004; Lustrino et al., 2010; Keskin et al., 2012;

Ekici et al., 2014); Dead Sea Fault, Syria (small circles: Ma et al., 2011); northwestern Syria (crosses: Krienitz et al., 2006), Harrat Ash Shalam, Jordan (x's: Shaw et al., 2003), and Afar plume (Pik et al., 1999). General locations of mantle end-member HIMU ("high-μ"), common mantle ("C"), and the enriched mantle end-members EM1 and EM2, along with eastern Mediterranean sediments (EMS; Klaver et al., 2015) and the location of the mantle array (Vervoort et al., 1999) are shown for reference.

Figure 8. Plots of $^{40}Ar/^{39}Ar$ data from this study. A) Samples of basanite from the Delihalil volcano. B) Samples of alkali basalt from the Toprakkale volcanic field. C) Samples of alkali basalt from the Karasu volcanic field.

Figure 9. (A) Distribution of major fault patterns near the Cyprus-Arabia-Anatolia triple junction overlain on upper mantle shear-wave velocity (70 km below surface). Faults in red correspond to the main and northern strands of the EAFZ. Faults in orange include the DSFZ, the Central Analtolian fault, the Yesemek fault, and the Aeferin fault (see Fig. 2 for locations). Velocities reach < 4.2 km/s in the upper mantle, indicating the presence of melt under much of the region. Blue contour demarcates the edge of Cyprean slab from Delph et al. (2017). Volcanism only appears to reach the surface east of the Cyprean slab where faulting occurs near the triple junction. Yellow squares are samples from this study; red circles are samples from other studies cited in text. Purple line is cross-section location for Fig. 9B with white circle demarcating 100 km distance along line. (B) Cross-section through the A^3 triple junction (modified from Delph et al., 2017). Estimates of melting equilibration depths for primary melts shown, obtained for samples analyzed in this study (yellow squares) and for compiled literature data (red circles).

Red line shows the approximate location of the lithosphere-asthenosphere boundary (LAB). CAF: Central Anatolian fault; N. EAFZ: Northern strand of the East Anatolian fault; DSF/EAFZ: Dead Sea fault/East Anatolian fault.

Figure 10. Temporal and spatial locations of K-Ar and $^{40}Ar/^{39}Ar$ data (this study and all published data cited in the text) from the Toprakkale and Karasu volcanic fields plotted on Google Earth satellite image. The position of all major faults associated with the EAFZ are plotted in yellow, and specific fault names can be found in Figure 2. Data from the Toprakkale volcanic field indicate punctuated volcanism in close proximity to faults. Data from from the Karasu volcanic field are similarly associated with faulting. Although equivocal, the data from the Karasu volcanic field exhibit a possible record of eastward migration of active volcanism (indicated by white arrows) over the last 200 ka.

Figure 11. Digital elevation map with major tectonic features of the EAFZ system labeled and illustrating the approximate position of the Anatolia-Arabia-Africa (A^3) triple junction at 5 Ma near Kahramanmaraş (K) and at 0 Ma near the Amik Basin (A). Some faults are dotted for clarity, and others are dashed where inferred. The triple junction migration was synchronous with a southward repositioning of the Africa – Anatolia plate boundary to the south of Cyprus by 5 Ma. Note the restriction of Quaternary (< 2.6 Ma) basalts (yellow) to a region of transtension between the triple junction positions (block arrows), and the two strands of the EAFZ. Active extrusion of the Anatolian microplate at 5 Ma transformed the triple junction from a boundary along a convergent zone (Bitlis suture) to one migrating along a transform plate boundary influenced by the extruding plate. The plate boundary reorganization was coincident with a

southward jump in the position of the active trench (red arrows) to one defining the current Anatolia–Africa plate boundary. This trench jump is consistent with Pliocene uplift occurring within Cyprus (e.g., McCallum and Robertson, 1995; Kinnaird et al., 2011). The current position of the A^3 triple junction is consistent with deformation transitioning from the northern strand to the main southern strand of the EAFZ. Geologic conditions favor continued migration of the A^3 triple junction in conjunction with rollback of the African plate along the Dead Sea transform fault, with future uplift of the Eratosthenes seamount as trench migration progresses.

References

Abgarmi, B., Delph, J.R., Ozacar, A.A., Beck, S.L., Zandt, G., Sandvol, E., Turkelli, N., and Biryol, C.B., 2017, Structure of the crust and African slab beneath the central Anatolian plateau from receiver functions: New insights on isostatic compensation and slab dynamics. Geosphere, v. 13 (6), p. 1774–1787. doi: https://doi.org/10.1130/GES01509.1

Aksu, A.E., Calon, T.J., Hall, J., and Yaşar, D., 2005, Origin and evolution of the Neogene İskenderun Basin, northeastern Mediterranean Sea, Marine Geology, v. 221, Issues 1–4, pp. 161-187, https://doi.org/10.1016/j.margeo.2005.03.010.

Aldanmaz, E., Köprübaşı, N., Gürer, Ö.F., Kaymakçı, N. and Gourgaud, A., 2006, Geochemical constraints on the Cenozoic, OIB-type alkaline volcanic rocks of NW Turkey: Implications for mantle sources and melting processes, Lithos, v. 86, p. 50-76, https://doi.org/10.1016/j.lithos.2005.04.003.

Aldanmaz, E., Pickard, M., Meisel, T., Altunkaynak, Ş., Kaan, S., Pinar, Ş., Hannan, B., and Furman, T., 2015, Source components and magmatic processes in the genesis of Miocene to Quaternary lavas in western Turkey: constraints from HSE distribution and Hf–Pb–Os isotopes. Contrib Mineral Petrol v. 170, https://doi.org/10.1007/s00410-015-1176-x.

Alıcı, P., Temel, A., Gourgaud, A., Vidal, P., and Gündogdu, M.N., 2001, Quaternary tholeittic to alkaline volcanism in the Karasu Valley, Dead Sea rift zone, Southeast Turkey: Sr-Nd-Pb-O isotopic and trace-element approaches to crust-mantle interaction. International Geology Review, v. 43:2, p. 120-138.

Angus, D.A., Wilson, D.C., Sandvol, E., and Ni, J.F., 2006, Lithospheric structure of the Arabian and Eurasian collision zone in eastern Turkey from *S*-wave receiver functions, Geophysical Journal International, v. 166, Issue 3, September 2006, p. 1335–1346, https://doi.org/10.1111/j.1365-246X.2006.03070.x

Arger, J., Mitchell, J., and Westaway, R.W.C., 2000, Neogene and Quaternary volcanism of southeastern Turkey. Geological Society, London, Special Publications, v. 173, p. 459-487.

Arpat, A.E., and Şaroğlu, F., 1972, Doğu Anadolu Fayı ile ilgili bazı gözlem ve düşünceler. Bulletin of the Mineral Research and Exploration, v.73, p. 1–9.

Bağcı, U., Alpaslan, M., Frei, R., Kurt, M.A., and Temel, A., 2011, Different degrees of partial melting of the enriched mantle source for Plio-Quaternary basis volcanism, Toprakkale (Osmaniye) region, southern Turkey. Turkish Journal of Earth Sciences, v. 20, p. 115-135.

Becker, T.W., and Faccenna, C., 2011, Mantle conveyor beneath the Tethyan collisional belt, Earth and Planetary Science Letters, v. 310, p. 453-461.

Bertrand, H., Chazot, G., Blichert-Toft, J., and Thoral, S., 2003, Implications of widespread high-μ volcanism on the Arabian Plate for Afar mantle plume and lithosphere composition, Chemical Geology, v. 198, pp. 47-61, https://doi.org/10.1016/S0009-2541(02)00418-7.

Birck, J.L. and Allégre, C.J., 1978, Chronology and chemical history of the parent body of basaltic achondrites studied by ^{87}Rb-^{87}Sr method. Earth Planetary Science Letters, v. 39, p. 37-51.

Biryol, C. B., S. L. Beck, G. Zandt, and Özacar, A.A., 2011, Segmented African lithosphere beneath the Anatolian region inferred from teleseismic P-wave tomography, Geophys. J. Int., v. 184, p. 1037–1057, doi:10.1111/j.1365-246X.2010.04910.x.

Blichert-Toft, J., Chauvel, C., and Albarède, F. (1997). Separation of Hf and Lu for high-precision isotope analysis of rock samples by magnetic sector-multiple collector ICP-MS. Contributions to Mineralogy and Petrology, v. 127(3), p. 248-260.

Bosworth, W., and Stockli, D., 2016. Early magmatism in the greater Red Sea rift: Timing and significance. Canadian Journal of Earth Sciences, v. 53. 10.1139/cjes-2016-0019.

Brocard, G.Y., Meijers, M.J.M, Cosca, M.A., Salles, T., Willenbring, J., Teyssier, C., and Whitney, D.L., 2020. Fast integration of the Central Anatolian Plateau drainage driven by Pliocene surface uplift and escape tectonics. Geosphere (in review).

Burton-Ferguson, R, Aksu, A.E., Calon, T.J., and Hall, J., 2005, Seismic stratigraphy and structural evolution of the Adana Basin, eastern Mediterranean. Marine Geology, v. 221, p. 189-222.

Çapan, U.Z., Vidal, P.H. and Cantagrel, J.M. 1987, K-Ar, Nd, Sr and Pb isotopic study of Quaternary volcanism in Karasu valley (Hatay), N-end of Dead Sea rift zone in SE Turkey. Yerbilimleri, v. 14, p. 165–178.

Cavalié, O., and Jónsson, S., 2014, Block-like plate movements in eastern Anatolia observed by InSar. Geophysical Research Letters, v. 41., p. 26-31, doi:10.1002/2013GL058170.

Cesare, B., Rubatto, D., and Gómez-Pugnaire, M.T., 2009. Do extrusion ages reflect magma generation processes at depth? An example from the Neogene Volcanic Province of SE Spain. Contributions to Mineralogy and Petrology, v. 157, p. 267–279.

Chorowicz, J., Dhont, D., Ammar, O., Rukieh, M., and Bilal, A., 2005, Tectonics of the Pliocene Homs basalts (Syria) and implications for the Dead Sea Fault Zone activity. Journal of the Geological Society, London, v. 162, p. 259–271.

Çoban, H., 2007, Basalt magma genesis and fractionation in collision- and extension-related provinces: A comparison between eastern, central and western Anatolia, Earth-Science Reviews, v. 80, p. 219-238, https://doi.org/10.1016/j.earscirev.2006.08.006.

Cosentino, D., Schildgen, T.F., Cipollari, P., Faranda, C., Gliozzi, E., Hudáčková, N., Lucifora, S., Strecker, M.R., 2012, Late Miocene surface uplift of the southern margin of the Central Anatolian Plateau, Central Taurides, Turkey. GSA Bulletin, v. 124 (1-2), p.133–145. doi: https://doi.org/10.1130/B30466.1

Dalrymple, G.B., Alexander, E.C., Lanphere, M.A. and Kraker, G.P., 1981, Irradiation of samples for 40Ar/39Ar dating using the geological survey TRIGA reactor. *In: USGS Professional Papers. U.S. Geological Survey, Reston, VA, United States. 1176: 29.*

Delph, J.R., Abgarmi, B., Ward, K.M., Beck, S.L., Özacar, A.A., Zandt, G., Sandvol, E., Türkelli, N., Kalafat, D., 2017, The effects of subduction termination on the continental lithosphere: Linking volcanism, deformation, surface uplift, and slab tearing in central Anatolia. Geosphere, v. 13, p. 1788–1805. doi: https://doi.org/10.1130/GES01478.1

Dewey, J.F., and Şengör, A.M.C., 1979, Aegean and surrounding regions: Complex multiplate and continuum tectonics in a convergent zone. GSA Bulletin, v. 90 (1), p, 84–92. doi: https://doi.org/10.1130/0016-7606(1979)90<84:AASRCM>2.0.CO;2

Dewey, J.F., Hempton, M.R., Kidd, W.S.F., Saroglu, F., and Şengör, A.M.C., 1986, Shortening of continental lithosphere: the neotectonics of Eastern Anatolia — a young collision zone. Geological Society, London, Special Publications, v.19, p.1-36, https://doi.org/10.1144/GSL.SP.1986.019.01.01

Duman, T.Y., and Emre, O., 2013, The East Anatolian Fault: geometry, segmentation and jog characteristics. In: Robertson, A. H. F., Parlak, O., and Ünlügenc, U. C. (eds) 2013. Geological Development of Anatolia and the Easternmost Mediterranean Region. Geological Society, London, Special Publications, v. 372, p. 495–529.

Ekici, T., and Macpherson, C., 2019, Convergence-aligned foreland magmatism in the Arabia-Anatolia Collision: geochronological evidence from the Karacadağ Volcanic Complex, south-east Turkey. Turkish Journal of Earth Sciences, v. 28, p. 719-733. doi:10.3906/yer-1902-25.

Ekici, T., Macpherson, C. G., Otlu, N., and Fontignie, D. 2014, Foreland magmatism during the Arabia–Eurasia collision: Pliocene–Quaternary activity of the Karacadağ Volcanic Complex, SW Turkey. Journal of Petrology, v. *55*(9), p. 1753-1777.

Eisele, J., Abouchami, W., Galer, S. J., and Hofmann, A. W., 2003, The 320 kyr Pb isotope evolution of Mauna Kea lavas recorded in the HSDP- 2 drill core. Geochemistry, Geophysics, Geosystems, v. 4(5).

Ergin, M., Aktar, M., Eyidoğan, H., 2004, Present-day seismicity and seismotectonics of the Cilician Basin: Eastern Mediterranean region of Turkey, Bulletin of the Seismological Society of America, v. 94 (3), pp. 930-939. DOI: 10.1785/0120020153.

Ferrari, L., 2004. Slab detachment control on mafic volcanic pulse and mantle heterogeneity in central Mexico. Geology, v. 32, p. 77–80.

Gürsoy, H., Tatar, O., Piper, J.D.A., Heimann, A., and Mesci, L., 2003, Neotectonic deformation linking the east Anatolian and the Karatas-Osmaniye intracontinental transform fault zones in the Gulf of İskenderun, southern Turkey, deduced from paleomagnetic study of the Ceyhan-Osmaniye volcanics. Tectonics, v. 22, 1067, doi:10.1029/2003TC001524.

Hanan, B.B., and Graham, D.W., 1996, Lead and Helium Isotope Evidence from Oceanic Basalts for a Common Deep Source of Mantle Plumes, Science, v. 272, Issue 5264, p. 991-995 DOI: 10.1126/science.272.5264.991.

Hansen, S.E., Rodgers, A.J., Schwartz, S.Y., and Al-Amri, A.M.S., 2007, Imaging ruptured lithosphere beneath the Red Sea and Arabian Peninsula. Earth and Planetary Science Letters, v. 259, p. 256-265.

Hempton, M., 1987, Constraints on Arabian plate motion and extensional history of the Red Sea. Tectonics, v. 6, p. 687-705.

Holzer, T. L., 2000, Implications for Earthquake Risk Reduction in the United States from the Kocaeli, Turkey Earthquake of August 17, 1999. U.S. Geological Survey Circular 1193. Washington: U.S. G.P.O. Print. 64p.

Imprescia, P., Pondrelli, S., Vannucci, G., and Gresta, S., 2012, Regional centroid moment tensor solutions in Cyprus from 1977 to the present and seismotectonic implications. J. Seismology, v. 16, p. 147–167. https://doi.org/10.1007/s10950-011-9254-7

Italiano, F., Yuce, G., Di Bella, M., Rojay, B., Sabatino, G., Tripodo, A., Martelli, M., Rizzo, A.L., and Misseri, M., 2017, Noble gases and rock geochemistry of alkaline intraplate volcanics from the Amik and Ceyhan-Osmaniye areas, SE Turkey, Chemical Geology, v. 469, p. 34-46.

Kaislaniemi, L., and van Hunen, J. (2014), Dynamics of lithospheric thinning and mantle melting by edge- driven convection: Application to Moroccan Atlas mountains, Geochem. Geophys. Geosyst., v.15, p. 3175– 3189, doi:10.1002/2014GC005414.

Karakas, O., Degruyter, W., Bachmann, O., and Dufek, J., 2017, Lifetime and size of shallow magma bodies controlled by crustal-scale magmatism. Nature Geoscience, v.10(6), p. 446-450.

Karig, D.E., and Kozlu, H., 1990. Late Paleogene evolution of the triple junction region near Maraş, south-central Turkey. Journal of the Geological Society, London, 147, pp. 1023-1034.

Kavak, K.S., Tatar, O., Piper, J., Kocbulut, F., and Mesci, B.L., 2009, Determination of neotectonic features of the Karasu Basin (SE Turkey) and their relationship with Quaternary volcanic activity using Landsat ETM+ imagery. International Journal of Remote Sensing, v. 30:17, p. 4507-4524.

Kelley, K. A., and Cottrell, E., 2009, Water and the oxidation state of subduction zone magmas. Science, v. *325*(5940), p. 605-607.

Keshav, S., and Gudfinnsson, G. H., 2004, Silica-poor, mafic alkaline lavas from ocean islands and continents: Petrogenetic constraints from major elements. J Earth Syst Sci, v. 113, p. 723–736. https://doi.org/10.1007/BF02704032

Keskin, M., Chugaev, A.V., Lebedev, V.A., Sharkov, E.V., Oyan, V., and Kavak, O., 2012, The geochronology and origin of mantle sources for late Cenozoic intraplate volcanism in the frontal part of the Arabian plate in the Karacadağ neovolcanic area of Turkey. Part 1. The results of isotope-geochronological studies. J. Volcanolog. Seismol., v. 6, p. 352–360, https://doi.org/10.1134/S0742046312060036.

Kinnaird, T., Robertson, A., and Morris, A., 2011, Timing of uplift of the Troodos Massif (Cyprus) constrained by sedimentary and magnetic polarity evidence. Journal of the Geological Society. 168. 1-14. 10.1144/0016-76492009-150.

Klaver, M., T. Djuly, S. de Graaf, A. Sakes, J. Wijbrans, G. Davies, and P. Vroon (2015), Temporal and spatial variations in provenance of Eastern Mediterranean Sea sediments: Implications for Aegean and Aeolian arc volcanism, Geochim. Cosmochim. Acta, v. 153, p. 149–168.

Krienitz, M. S., Haase, K. M., Mezger, K., Eckardt, V., and Shaikh-Mashail, M. A., 2006, Magma genesis and crustal contamination of continental intraplate lavas in northwestern Syria. Contributions to Mineralogy and Petrology, v. 151(6), p. 698-716.

Kuiper, K.F., Deino, A., Hilgen, F.J., Krijgsman, W., Renne, P.R., and Wijbrans, J.R., 2008, Synchronizing rock clocks of earth history: Science, doi:10.1126/science.1154339.

Le Maitre, R.W., Bateman, P., Dudek, A., Keller, J., Lameyre, J., Le Bas, M.J., Sabine, P.A., Schmid, R., Sorensen, H., Streckeisen, A. and Woolley, A.R., 1989. A classification of igneous rocks and glossary of terms. Recommendations of the IUGS Subcommission on the Systematics of Igneous rocks. London: Blackwell Scientific Publications.

Lee, C-T, Luffi, P., Plank, T, Dalton, H., and Leeman, W. P., 2009, Constraints on the depths and temperatures of basaltic magma generation on Earth and other terrestrial planets using new thermobarometers for mafic magmas, Earth and Planetary Science Letters, v. 279, Issues 1–2, p 20-33.

Lee, J.Y., Marti, K., Severinghaus, J.P., Kawamura, K., Yoo, H.S., Lee, J.B., and Kim, J.S., 2006, A redetermination of the isotopic abundances of atmospheric Ar. Geochimica et Cosmochimica Acta, doi:10.1016/j.gca.2006.06.1563.

Ludwig, K.R., 1980, Calculation of uncertainties of U-Pb data: Earth and Planetary Science Letters, v. 46, p. 212-220.

Ludwig, K.R., 1985, PBDAT200: A Computer Program for processing raw Pb-U-Th isotope data. U.S. Geol. Surv. Open-File Report 85-547, 54 p.

Lugmair G.W., Scheinin, N.B., and Marti,K, 1975, Sm-Nd age and history of Apollo 17 basalt 75075: Evidence for early differentiation of the lunar exterior. Proc. Lunar Sci. Conf. 6th, pp. 1419-1429.

Lustrino, M., Keskin, M., Mattioli, M., Lebedev, V. A., Chugaev, A., Sharkov, E., and Kavak, O. 2010, Early activity of the largest Cenozoic shield volcano in the circum-Mediterranean area: Mt. Karacadağ, SE Turkey. European Journal of Mineralogy, v. 22(3), p. 343-362.

Ma, G.S.K., Malpas, J., Xenophontos, C. and Chan, G.H.N., 2011, Petrogenesis of latest Miocene–Quaternary continental intraplate volcanism along the northern Dead Sea Fault System (Al Ghab–Homs Volcanic Field), western Syria: evidence for lithosphere–asthenosphere interaction. Journal of Petrology, v. 52(2), p. 401-430.

Mahmoud, Y., Masson, F., Meghraoui, M., Cakir, Z., Alchalbi, A., Yavasoglu, H. Yönlü, O., Daoud, M., Ergintav, S., and Inan, S., 2013, Kinematic study at the junction of the East Anatolian fault and the Dead Sea fault from GPS measurements, Journal of Geodynamics, v. 67, p. 30-39, https://doi.org/10.1016/j.jog.2012.05.006.

McCallum, J. E., and Robertson, A. H. F. (1995), Sedimentology of two fan-delta systems in the Pliocene-Pleistocene of the Mesaoria Basin, Cyprus, Sediment. Geol., v.98 (1–4), p. 215–244.

McDonough, W.F., and Sun, S.S., 1995. The composition of the Earth, Chemical Geology, v. 120 (3-4), p. 223-253.

McKenzie, D. P., 1976, The East Anatolian Fault; a major structure in eastern Turkey. Earth and Planetary Science Letters, v. 29, p. 189–193.

McNab, F., Ball, P. W., Hoggard, M. J., and White, N. J., 2018, Neogene uplift and magmatism of Anatolia: Insights from drainage analysis and basaltic geochemistry. Geochemistry, Geophysics, Geosystems, v.19, p. 175– 213. https://doi.org/10.1002/2017GC007251.

Meijers, M.J.M., Brocard, G.Y., Cosca, M.A., Lüdecke, T., Teyssier, C., Whitney, D.L., and Mulch, A., 2018, Rapid late Miocene surface uplift of the Central Anatolian Plateau margin. Earth and Planetary Science Letters, v. 497, p. 29-41. doi: 10.1016/j.epsl.2018.05.040

Meijers, M.J.M., Brocard, G.Y., Whitney, D.L., and Mulch, A. 2020, Paleoenvironmental conditions and drainage evolution of the central Anatolian lake system (Turkey) during late Miocene to Pliocene surface uplift. Geosphere, doi: https://doi.org/10.1130/GES02135.1

Min, K., Mundil, R., Renne, P.R., and Ludwig, K.R., 2000, A test for systematic errors in ^{40}Ar/^{39}Ar geochronology through comparison with U/Pb analysis of a 1.1-Ga rhyolite: Geochimica et Cosmochimica Acta, doi:10.1016/S0016-7037(99)00204-5

Muehlberger, W.R. and Gordon, M.B., 1987, Observations on the complexity of the East Anatolian fault, Turkey. Journal of Structural Geology, v. 9, p. 889-903.

Nikogosian, I. K., Bracco Gartner, A. J. J., van Bergen, M. J., Mason, P. R. D., and van Hinsbergen, D. J. J., 2018, Mantle sources of recent Anatolian intraplate magmatism: A regional plume or local tectonic origin? Tectonics, v. 37. https://doi.org/10.1029/2018TC005219

Over, S., Kavak, Ş., Bellier, O., and Özden, S., 2004, Is the Amik Basin (SE Turkey) a triple-junction area? Analyses of SPOT XX imagery and seismicity. Int. J. Remote Sensing, v. 25, p. 3857-3872.

Oyan, V., 2018, Petrogenesis of the Quaternary mafic alkaline volcanism along the African-Anatolian plates boundary in Turunçlu-Delihalil (Osmaniye) region in southern Turkey. Lithos, v. 314-315, p. 630-645.

Parlak, O., Delaloye, M., Kozlu, H., and Fontignie, D., 2000, Trace element and Sr-Nd isotope geochemistry of the alkali basalts observed along the Yumurtalık Fault (Adana) in southern Turkey. Yerbilimleri, v. 22, p. 137-148.

Parlak O., Kozlu H., Demirkol C., and Delaloye M. (1997) Intracontinental Plio-Quaternary volcanism along the African-Anatolian plate boundary, southern Turkey. Ofioliti, v. 22, p. 111–117.

Parlak, O., Kop, A., Ünlügenç, U.C., and Demirkol, C., 1998, Geochronology and geochemistry of basaltic rocks in the Karasu graben around Kirikhan (Hatay), S. Turkey. Turkish Journal of Earth Sciences, v. 7, p. 53-61.

Pearce, J.A., 1996, A users guide to basaltic discrimination diagrams, in Wyman, D.A., ed., Trace element geochemistry of volcanic rocks: Applications for massive sulphide exploration: Geological Association of Canada, Short Course Notes, v. 12, p. 79-113.

Pearce, J.A., Bender, J.F., De Long, S.E., Kidd, W.S.F., Low, P.J., Güner, Y., Şaroglu, F., Yılmaz, Y., Moorbath, S. and Mitchell, J.G., 1990, Genesis of collision volcanism in Eastern Anatolia, Turkey. Journal of Volcanology and Geothermal Research, v. 44(1-2), p. 189-229.

Perinçek D., and Çemen İ. ,1990, The structural relationship between the East Anatolian and Dead Sea fault zones in southeastern Turkey. Tectonophysics, v. 172, p. 331–340.

Pik, R., Deniel, C., Coulon, C., Yirgu, G., and Marty, B., 1999, Isotopic and trace element signatures of Ethiopian flood basalts: evidence for plume–lithosphere interactions. Geochimica et Cosmochimica Acta, v. 63(15), p. 2263-2279.

Pilet, S., Baker, M.B., and Stolper, E.M., 2008, Metasomatized Lithosphere and the Origin of Alkaline Lavas. Science, v. 320, Issue 5878, p. 916-919, doi: 10.1126/science.1156563

Plank, T., and Forsyth, D.W., 2016, Thermal structure and melting conditions in the mantle beneath the Basin and Range Province from seismology and petrology: Geochemistry Geophysics Geosystems, v. 17, p. 1312–1338, https://doi .org/10.1002/2015GC006205.

Polat, A., Kerrich, R., and Casey, J.F., 1997, Geochemistry of Quaternary basalts erupted along the east Anatolian and Dead Sea fault zones of southern Turkey: implications for mantle sources. Lithos, v. 40, p. 55-68.

Portner, D.E., Delph, J.R., Biryol, C.B., Beck, S.L., Zandt, G., Ozacar, A.A., Sandvol, E., and Turkelli, N., 2018, "Subduction termination through progressive slab deformation across eastern Mediterranean subduction zones from updated P-wave tomography beneath Anatolia", Geosphere, v. 14, p. 907-925, doi:10.1130/GES01617.1.

Premo W.R. and Loucks, R.R., 2000, Age and Pb-Sr-Nd isotopic systematics of plutonic rocks from the Green Mountain magmatic arc, southeastern Wyoming: Isotopic characterization of a Paleoproterozoic island arc system, Rocky Mountain Geology, v. 35, no. 1, p. 51-70.

Premo, W.R. and Taylor, C.D., 2010, Radiogenic isotopic characterization and petrogenesis of host rocks to the Greens Creek deposit (Chapter 12) in *Geology, geochemistry, and genesis of the Greens Creek massive sulfide deposit, Admiralty Island, southeastern Alaska*: Taylor, C.D. and Johnson, C.A., eds. U.S. Geological Survey Professional Paper 1763, p. 335 – 365.

Reid, M. R., Bouchet, R. A., Blichert-Toft, J., Levander, A., Liu, K., Miller, M. S., and Ramos, F. C., 2012, Melting under the Colorado Plateau, USA. Geology, v. 40(5), p. 387-390.

Reid, M. R., Delph, J. R., Cosca, M. A., Schleiffarth, W. K., and Gençalioğlu Kuşcu, G., 2019, Melt equilibration depths as sensors of lithospheric thickness during Eurasia-Arabia collision and the uplift of the Anatolian Plateau. Geology, v. 47(10), p. 943-947.

Reid, M. R., Schleiffarth, W. K., Cosca, M. A., Delph, J. R., Blichert-Toft, J., and Cooper, K. M., 2017, Shallow melting of MORB-like mantle under hot continental lithosphere, Central Anatolia, Geochem. Geophys. Geosyst., v.18, p. 1866–1888, doi:10.1002/2016GC006772.

Reilinger, R., McClusky, S., Vernant, P., Lawrence, S., Ergintav, S., Cakmak, R., Ozener, H., Kadirov, F., Guliev, I., Stepanyan, R. and Nadariya, M., 2006, GPS constraints on continental deformation in the Africa-Arabia-Eurasia continental collision zone and implications for the dynamics of plate interactions, J. Geophys. Res., v. 111, B05411, doi:10.1029/2005JB004051.

Rojay, B., Heimann, A., and Toprak, V., 2001, The transition zone between the Dead Seas transform and the East Anatolian fault zone. Geodinamica Acta, v. 14, p. 197-212.

Schildgen, T., Cosentino, D., Bookhagen, B., Niedermann, S., Yıldırım, C., Echtler, H., Wittmann, H., and Strecker, M., 2012, Multi-phased uplift of the southern margin of the Central

Anatolian plateau, Turkey: A record of tectonic and upper mantle processes. Earth and Planetary Sciences, v. 317-318, p. 85-95. 10.1016/j.epsl.2011.12.003.

Şen, P. A., Temel, A., & Gourgaud, A. (2004). Petrogenetic modelling of Quaternary post-collisional volcanism: a case study of central and eastern Anatolia. Geological Magazine, v. 141(1), p. 81-98.

Şengör A.M.C. and Yilmaz, Y., 1981. Tethyan evolution of Turkey: a plate tectonic approach. Tectonophysics, v.75, p. 181-241.

Şengör, A.M.C., Görür, N., and Saroglu, 1985, Strike-slip faulting and related basin formation in zones of tectonic escape: Turkey as a case study. The Society of Economic Paleontologists and Mineralogists Special Publication 37, Strike-slip deformation, basin formation, and sedimentation, p. 227-264.

Seyrek, A., Demir, T., Pringle, M., Yurtmen, S., Westaway, R., Bridgland, D., Beck, A., and Rowbotham, G., 2008, Late Cenozoic uplift of the Amanos Mountains and incision of the Middle Ceyhan river gorge, southern Turkey; Ar-Ar dating of the Düziçi basalt. Geomorphology, v. 97, p. 321-355.

Seyrek, A., Demir, T., Pringle, M.S., Yurtmen, S., Westaway, R.W.C., Beck, A., and Rowbotham, G., 2007, Ar/Ar dating of offset Pleistocene basalt flows: transpression between the

African and Arabian plates. Geological Society, London, Special Publications, v. 290, p. 255-284.

Shaw, J. E., Baker, J. A., Menzies, M. A., Thirlwall, M. F., and Ibrahim, K. M., 2003, Petrogenesis of the largest intraplate volcanic field on the Arabian Plate (Jordan): a mixed lithosphere–asthenosphere source activated by lithospheric extension. Journal of Petrology, v. 44(9), p. 1657-1679.

Stern, R.J., and Johnson, P., 2010, Continental lithosphere of the Arabian Plate: A geologic, petrologic, and geophysical synthesis, Earth-Science Reviews, vol. 101, Issues 1–2, p. 29-67, https://doi.org/10.1016/j.earscirev.2010.01.002.

Stern, R.J., and Johnson, P., 2019, Constraining the Opening of the Red Sea: Evidence from the Neoproterozoic Margins and Cenozoic Magmatism for a Volcanic Rifted Margin. In: N. M. A. Rasul and I. C. F. Stewart (eds.), Geological Setting, Palaeoenvironment and Archaeology of the Red Sea, https://doi.org/10.1007/978-3-319-99408-6_4, p. 53-79.

Tanaka, T., Togashi, S., Kamioka, H., 19 other authors, and Dragusanu, C., 2000, JNdi-1: A neodymium isotopic reference in consistency with LaJolla neodymium, Chemical Geology, v. 168, p. 279-281.

Tarı, U., Tüysüz, O., Can Genç, Ş.., İmren, C., Blackwell, B., Lom, N., Tekeşin, Ö., Sibel Üsküplü, S., Erel, L., Altıok, S., and Beyhan, M., 2014, The geology and morphology of the

Antakya Graben between the Amik Triple Junction and the Cyprus Arc, Geodinamica Acta, p. 1-29, DOI:10.1080/09853111.2013.858962

Tatar, O., Piper, J.D.A., Gürsoy, H., Heimann, A., and Koçbulut, F., 2004, Neotectonic deformation in the transition zone between the Dead Sea Transform and the East Anatolian Fault Zone, Southern Turkey: a paleomagnetic study of the Karsu Rift Volcanism. Tectonophysics, v. 385, p. 17-43.

Tatsumoto, M. and Unruh, D.M., 1976, KREEP basalt age: Grain by grain U-Th-Pb systematics study of the quartz monzodiorite clast 15405, 88. Proc. Lunar Sci. Conf. 7th, p. 2107-2129.

Uslular, G., and Gençalioğlu-Kuşcu, G., 2019a, Geochemical characteristics of Anatolian basalts: Comment on “Neogene uplift and magmatism of Anatolia: Insights from drainage analysis and basaltic geochemistry” by McNab et al. Geochemistry, Geophysics, Geosystems, v. 20(1), p. 530-541.

Uslular, G. and Gençalioğlu-Kuşcu, G., 2019b, Mantle source heterogeneity in monogenetic basaltic systems: A case study of Eğrikuyu monogenetic field (Central Anatolia, Turkey). Geosphere, v.15(2), p. 295-323.

Vervoort, J. D., P. J. Patchett, Blichert-Toft, J., and Albarède , F., 1999, Relationships between Lu-Hf and Sm-Nd isotopic systems in the global sedimentary system, Earth and Planetary Science Letters, v. 168, p. 79–99.

Westaway, R., 2003. Kinematics of the Middle East and Eastern Mediterranean updated. Turkish Journal of Earth Sciences v. 12, p. 5–46.

Westaway, R., 2004. Kinematic consistency between the Dead Sea Fault Zone and the Neogene and Quaternary left-lateral faulting in SE Turkey. Tectonophysics v. 391, p. 203–237.

White, W.M., Albarède, F. and Télouk, P., 2000, High-precision analysis of Pb isotope ratios by multi-collector ICP-MS. Chemical Geology, v. 167(3-4), p.257-270.

Yilmaz, H., Over, S., and Ozden, S., 2006, Kinematics of the East Anatolian Fault Zone between Turkoglu (Kahramanmaraş) and Çelikhan (Adiyaman), eastern Turkey. Earth Planets Space, v. 58, p. 1463-1473.

Yuce, G., Italiano, F., D'Alessandro, W., Yalcin, T.H., Yasin, D.U., Gulbay, A.H., Ozyurt, N.N., Rojay, B., Karabacak, V., Bellomo, S., Brusca, L., Yang, T., Fu, C.C., Lai, C.W., Ozacar, A., and Walia, V., 2014, Origin and interactions of fluids circulating over the Amik Basin (Hatay, Turkey) and relationships with the hydrologic, geologic, and tectonic settings. Chemical Geology, v. 388, p. 23-39.

Yurtmen, S., Guillou, H., Westaway, R., Rowbotham, G., and Tatar, O., 2002, Rate of strike-slip motion on the Amanos Fault (Karasu Valley, southern Turkey) constrained by K-Ar dating and geochemical analysis of Quaternary basalts. Tectonophysics, v. 344, p. 207-246.

Yurtmen, S., Rowbotham, G., Isler, F., and Floyd, P.A., 2000, Petrogenesis of basalts from Southern Turkey: the Plio-Quaternary volcanism to the North of İskenderun ;Gulf. Geological Society, London, Special Publications 2000, v. 173, p. 489-512.

Figure 1

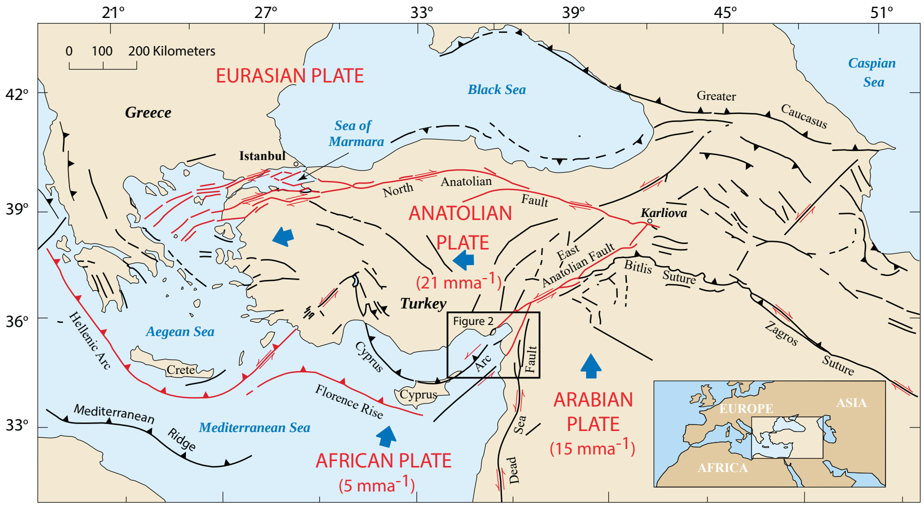

Figure 1.

Figure 2

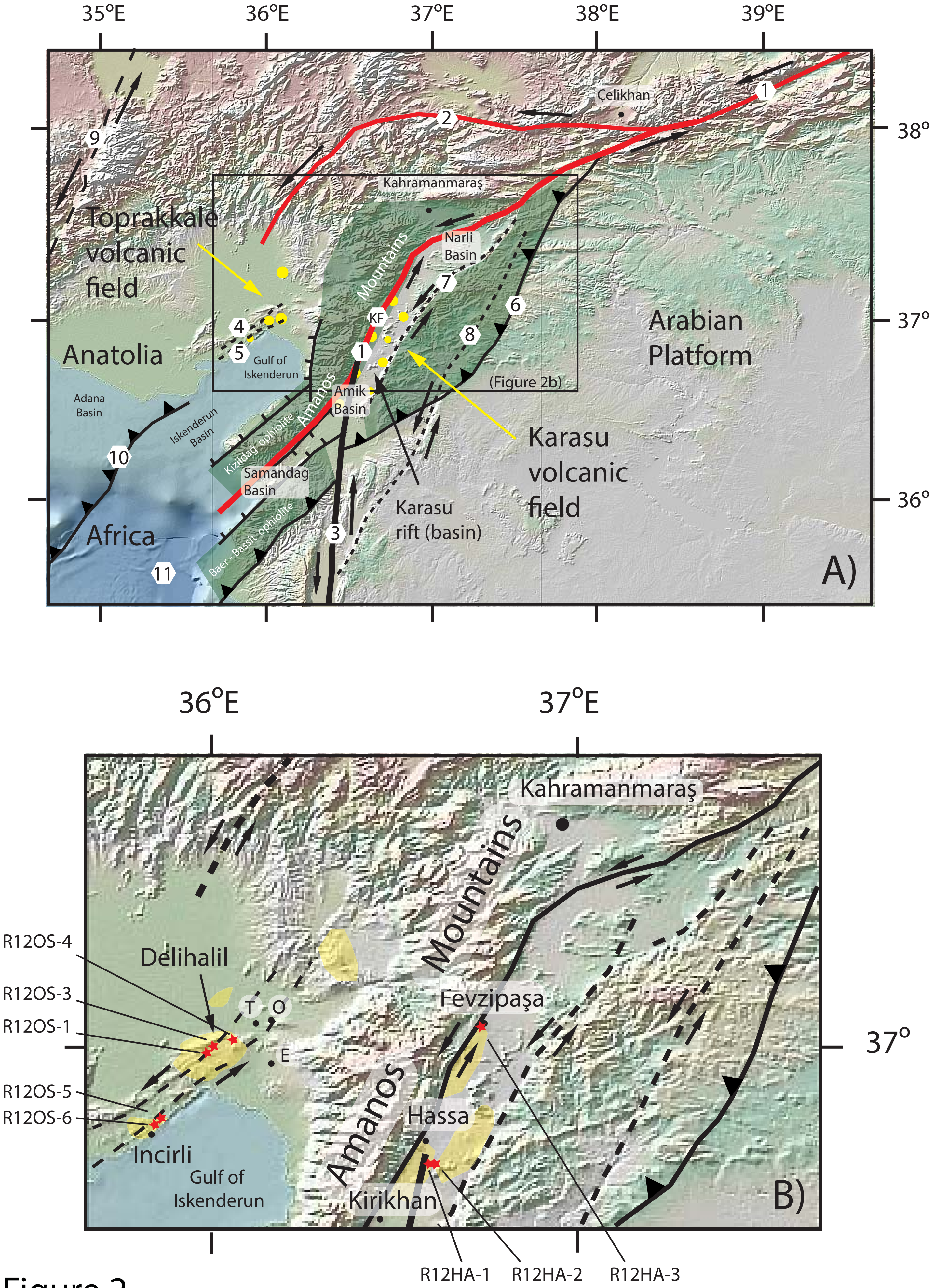

Figure 2.


F


F


F


F

Figure 3

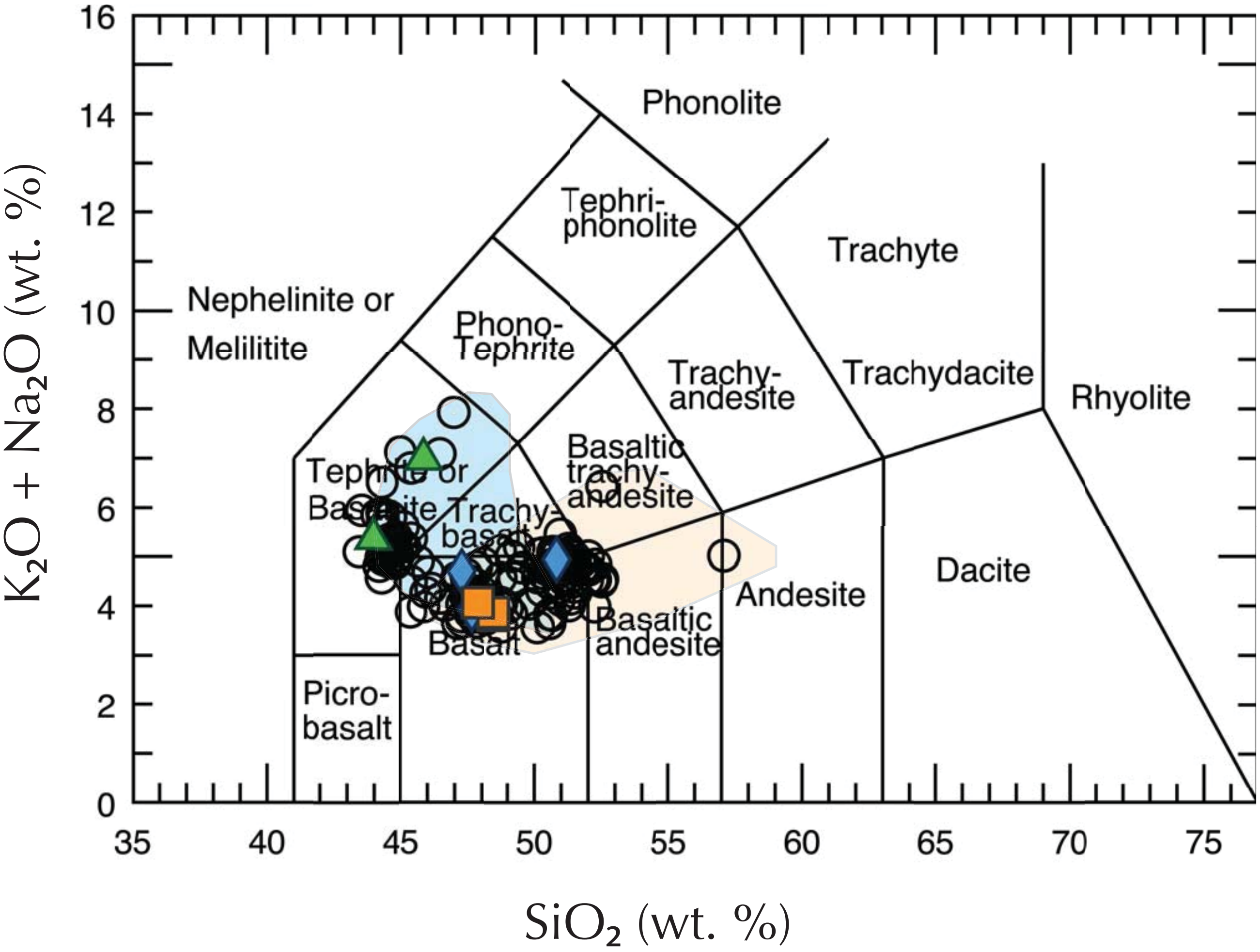

Figure 3.

Figure 4

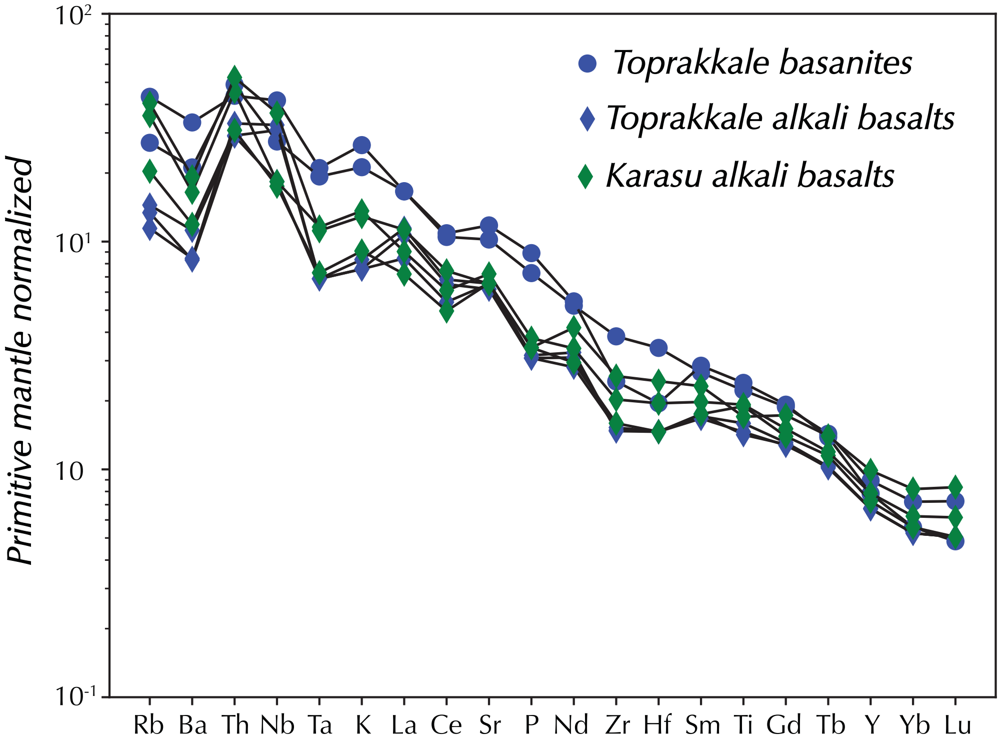

Figure 4.

Figure 5

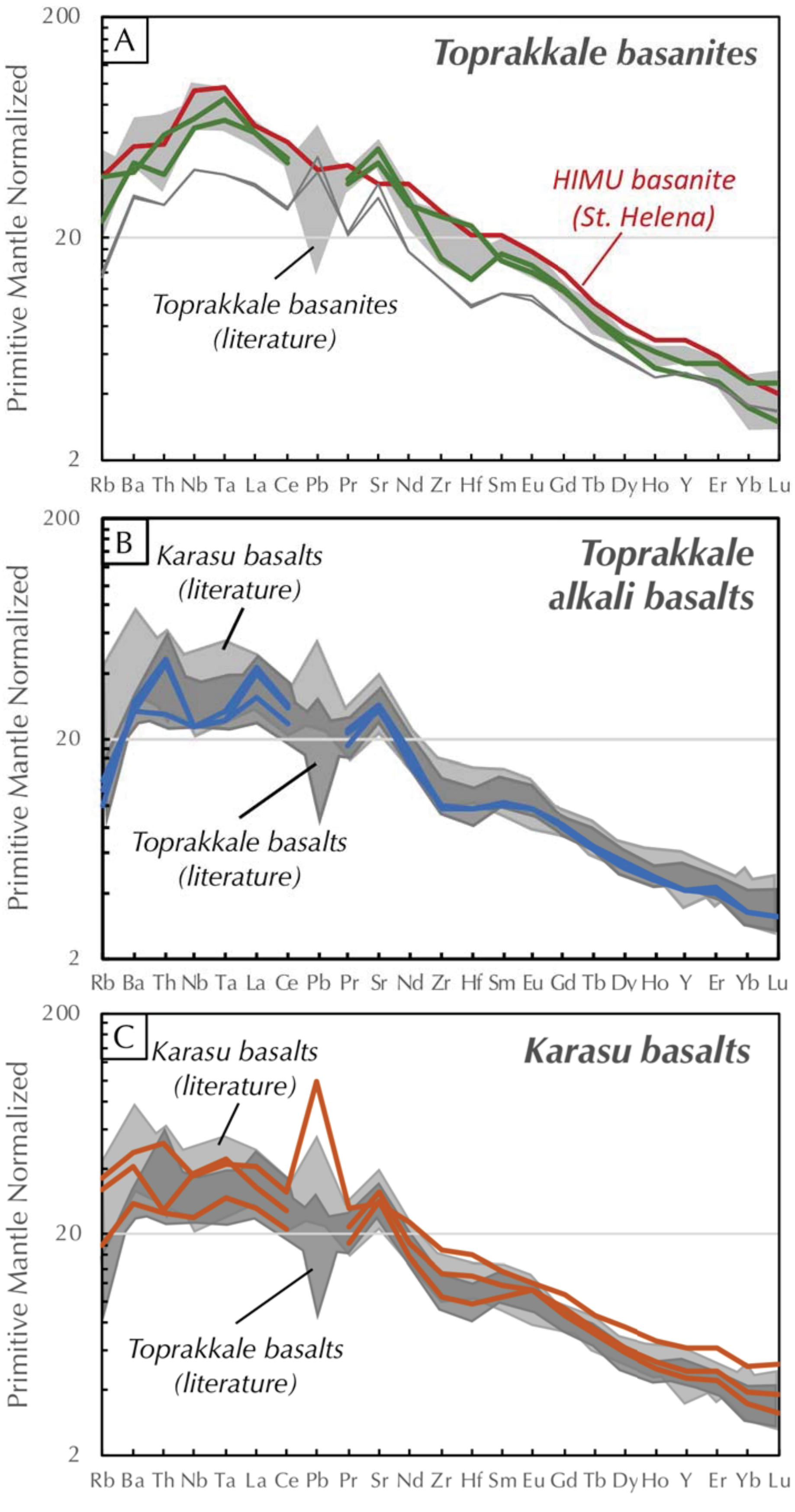

Figure 5.

Figure 6

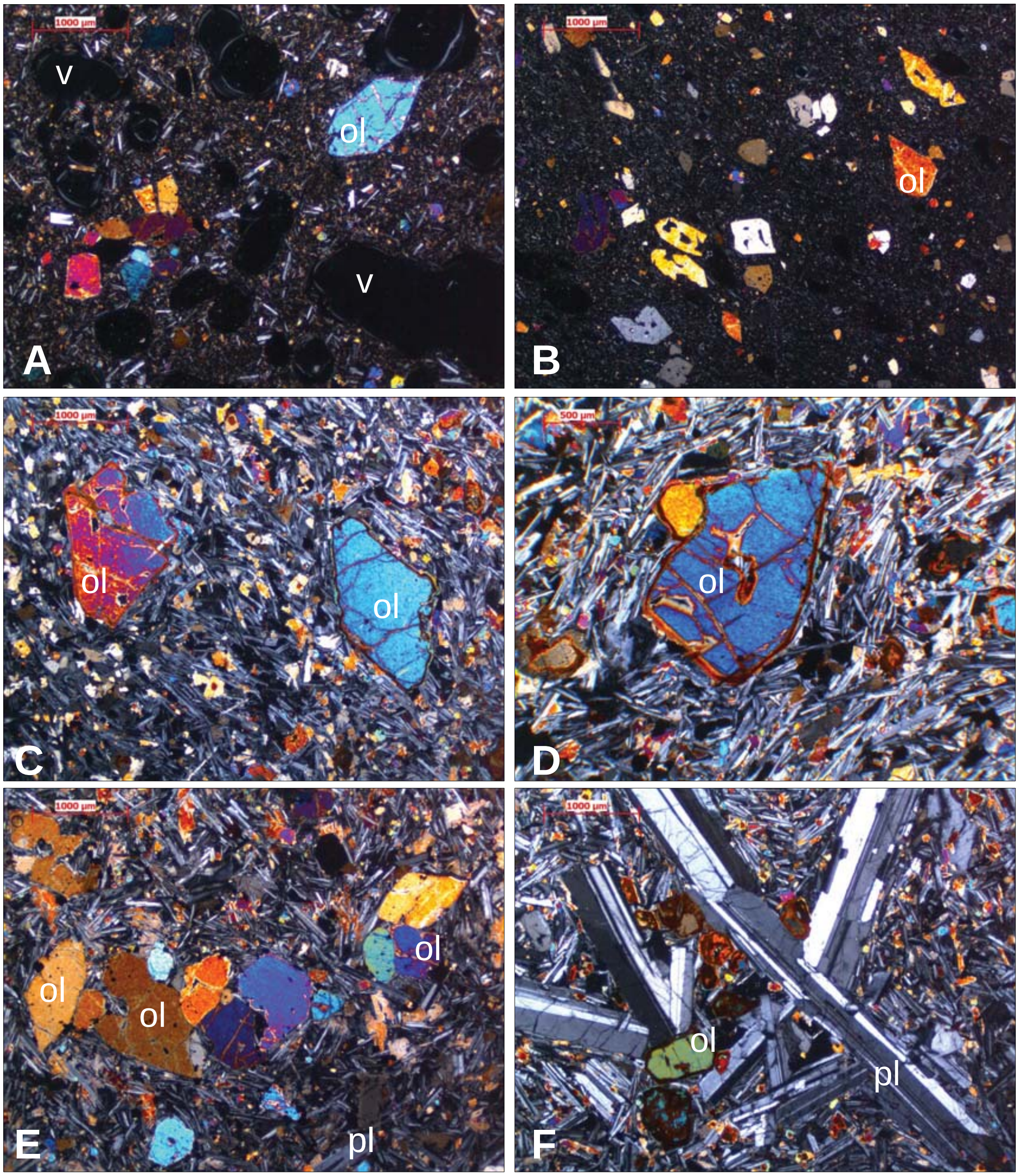

Figure 6.

Figure 7

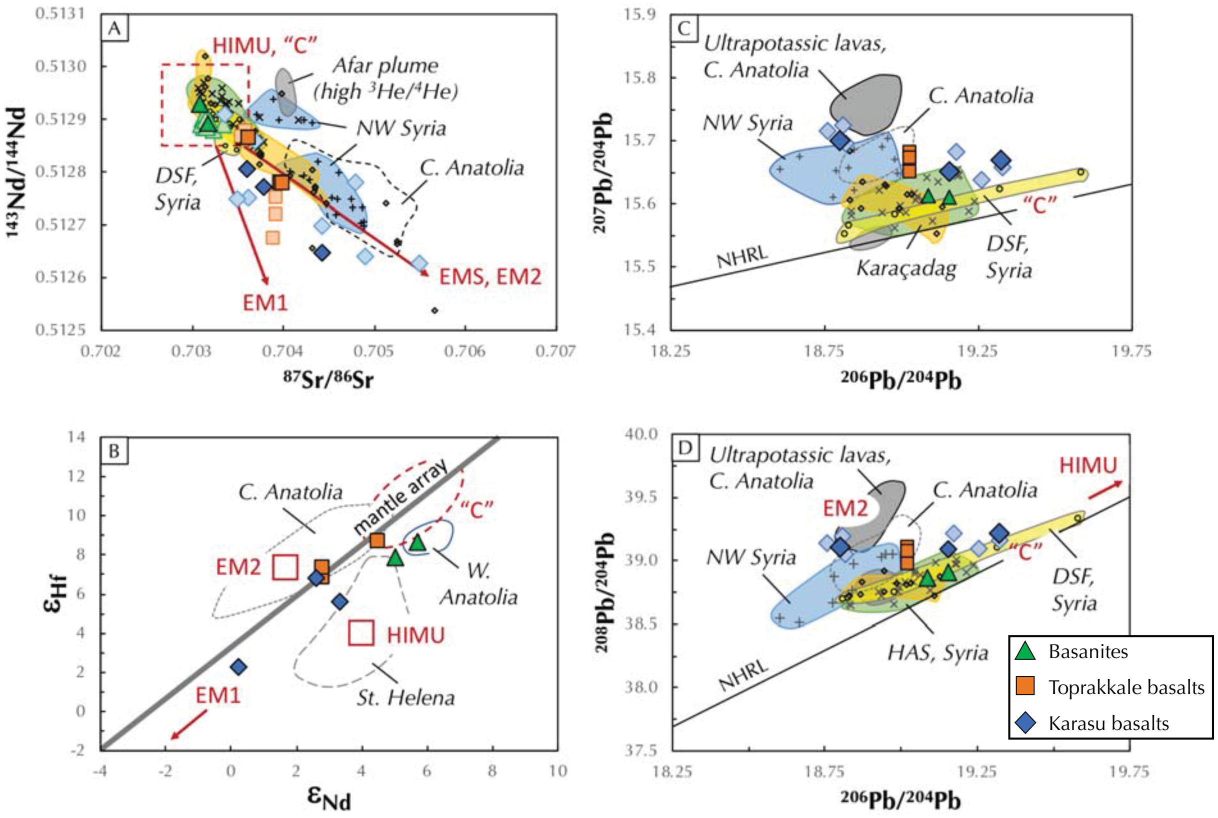

Figure 7.

Figure 8

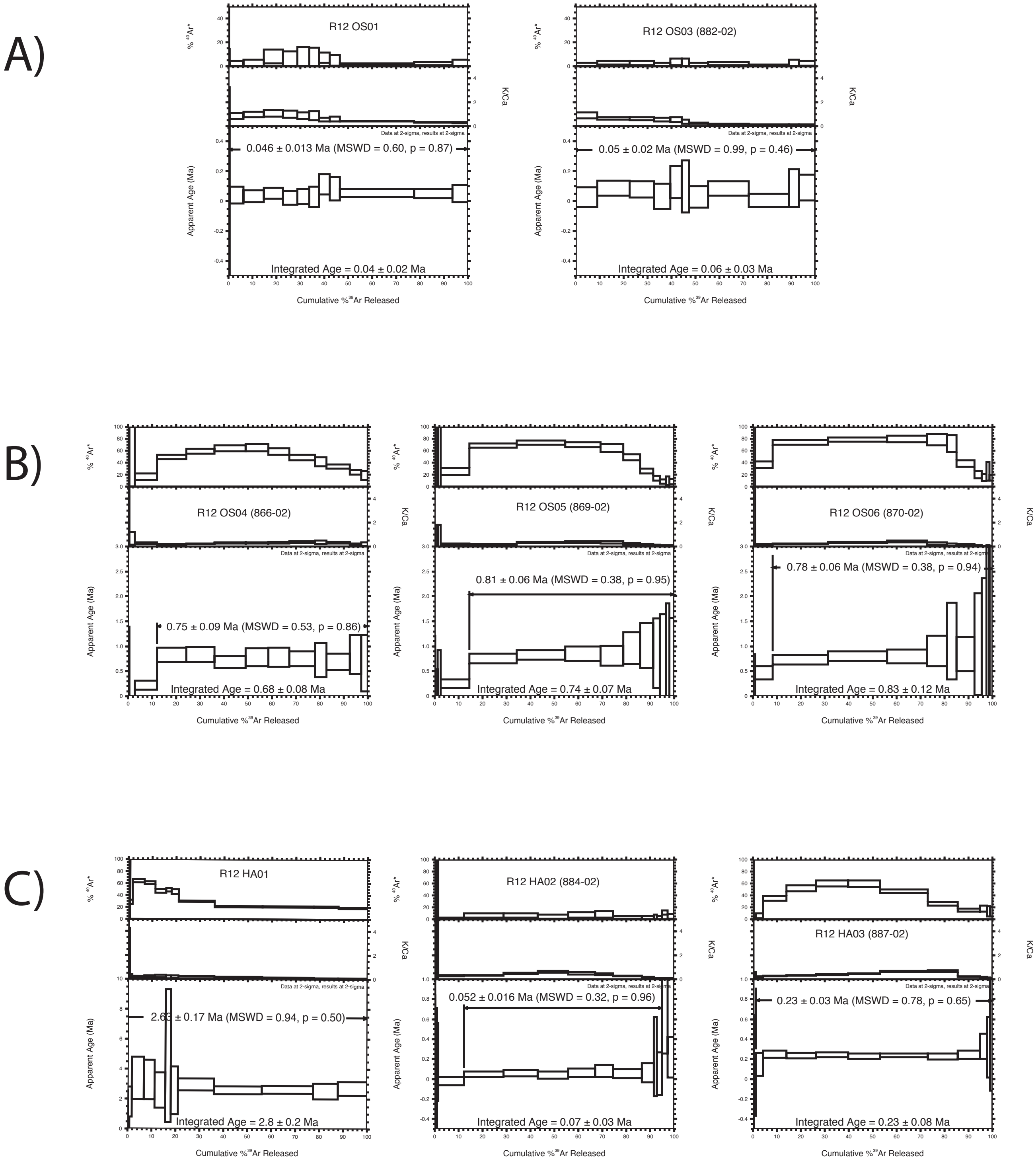

Figure 8.

Figure 9

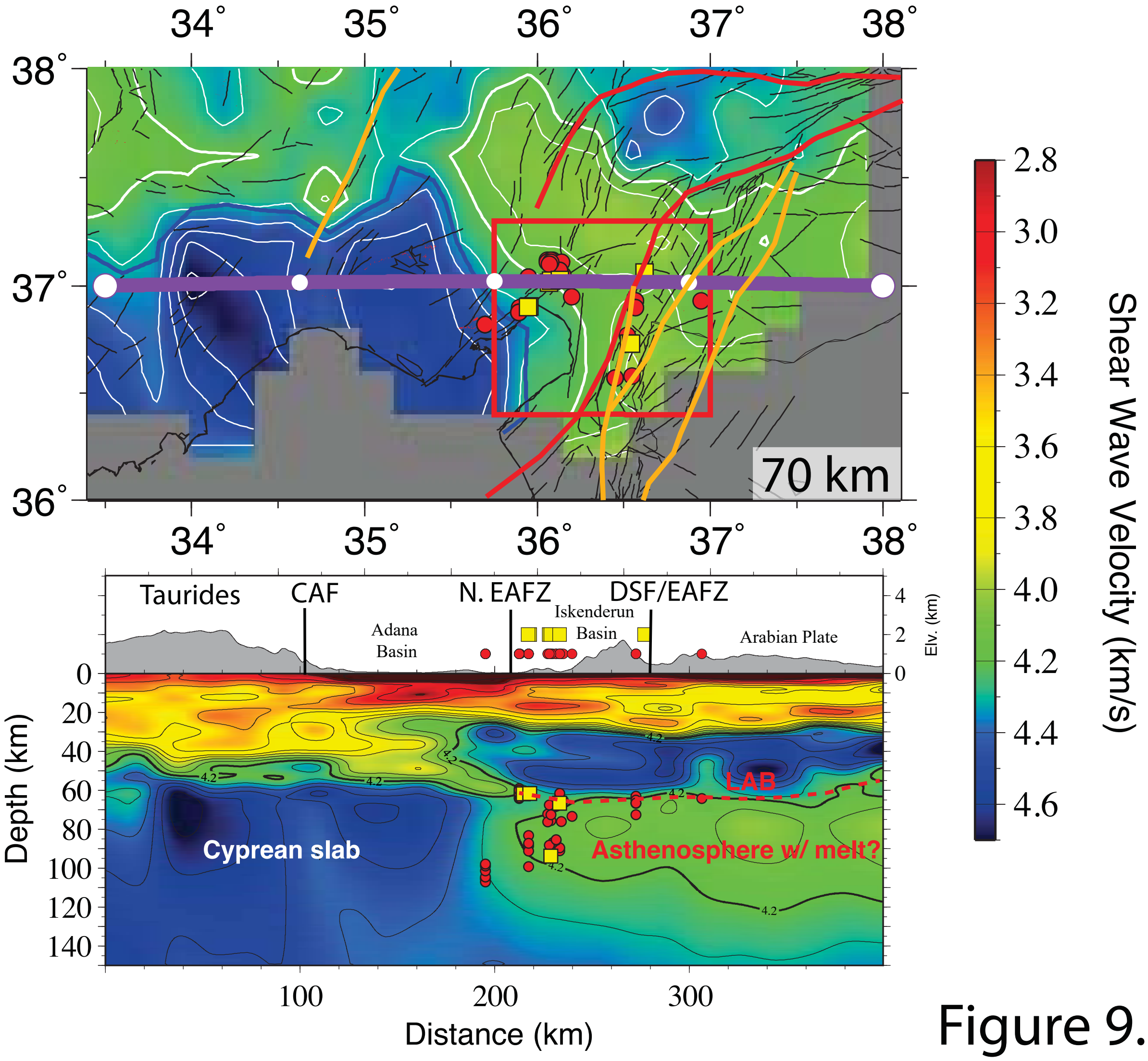

Figure 9.

Figure 10

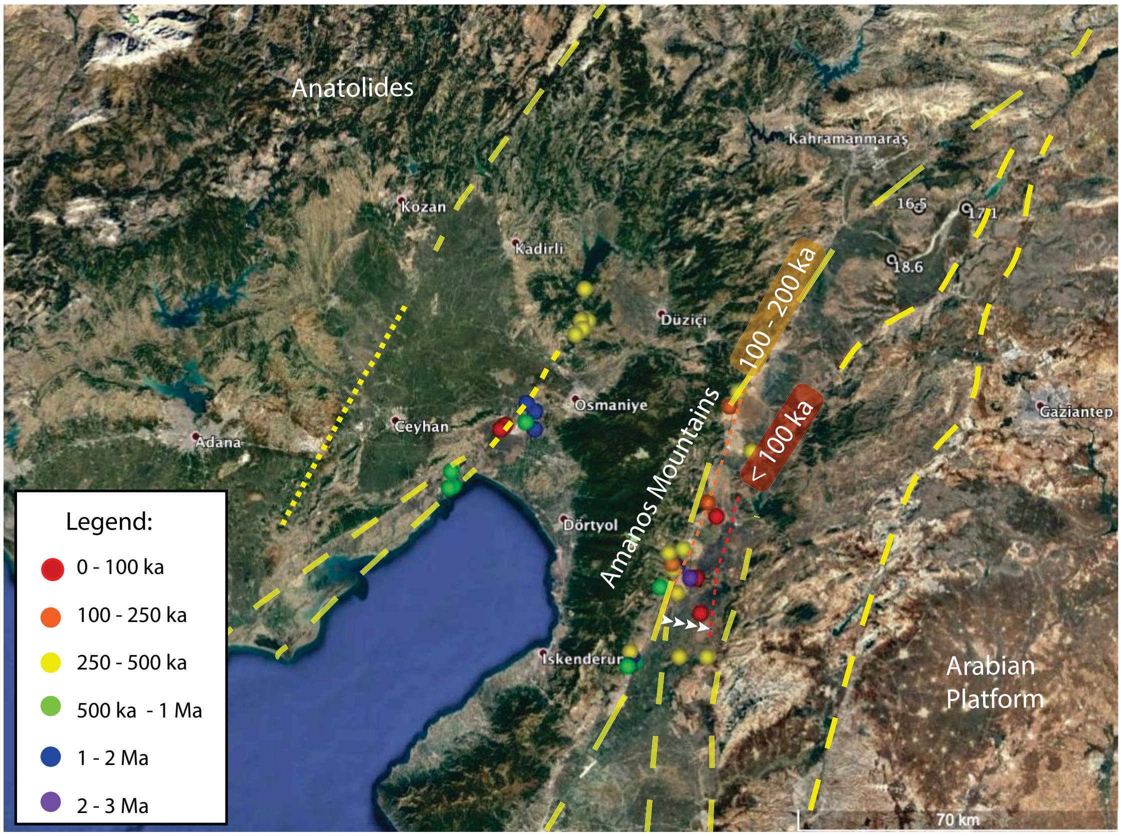

Figure 10.

Figure 11

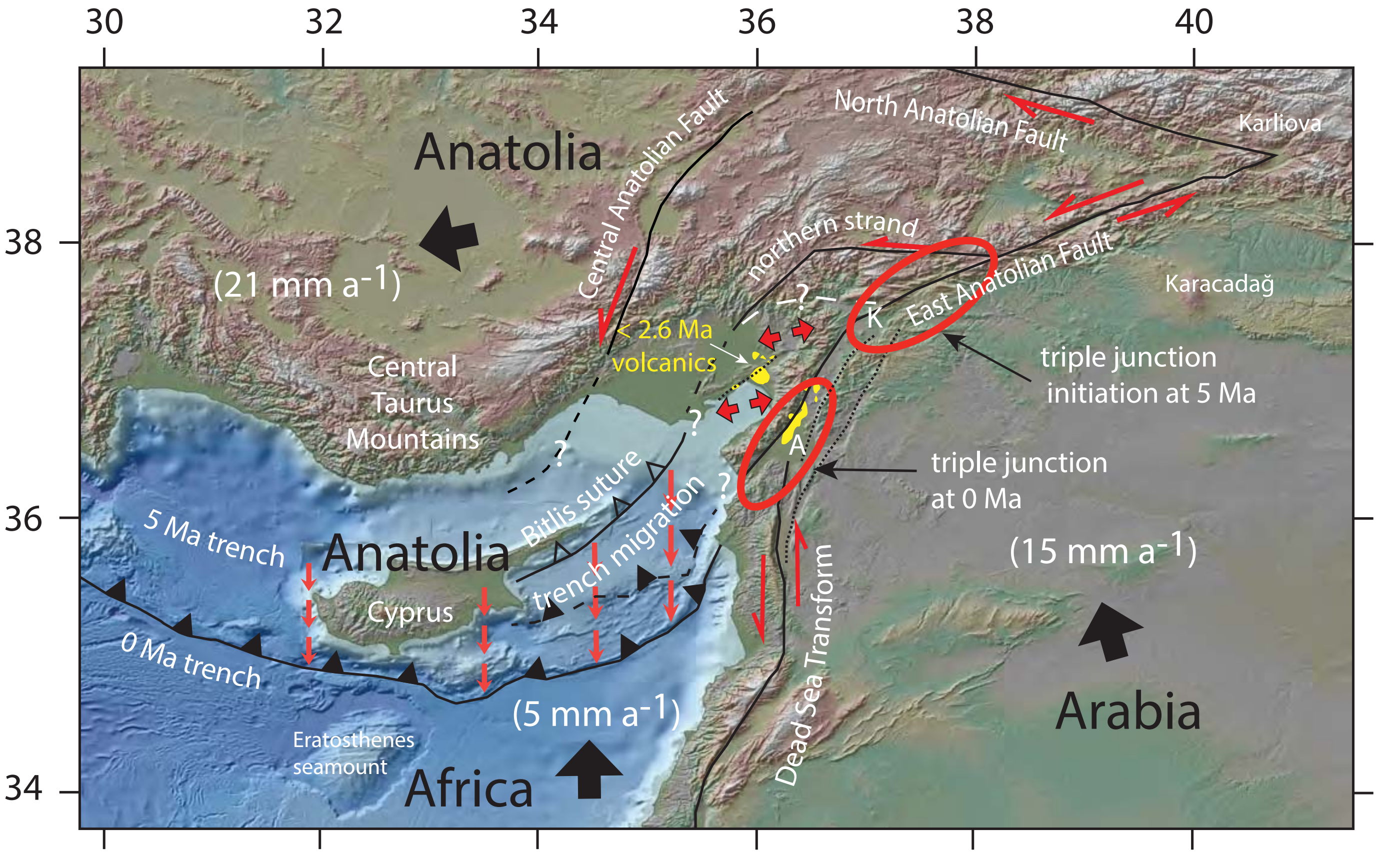

Figure 11.

Sample	R12 OS 01	R12 OS 03	R12 OS 04	R12 OS 05	R12 OS 06	R12 HA 01
Latitude	37.015	37.023	37.029	36.905	36.901	36.732
Longitude	36.067	36.078	36.128	35.955	35.945	36.529
Rock type	Basanite	Basanite	Basalt	Basalt	Basalt	Basalt
SiO_2	45.3	43.5	47.4	48.5	48.2	47.4
TiO_2	2.82	3.04	2.02	1.8	1.85	2.4
Al_2O_3	15.9	14.4	15.4	15.3	15.1	16.1
Fe_2O_3	11.8	13.4	12.7	12.9	12.9	12.8
Cr_2O_3	0.01	0.05	0.04	0.05	0.05	0.03
MnO	0.17	0.18	0.16	0.17	0.17	0.18
MgO	7.86	9.34	7.92	8.74	8.62	6.99
CaO	8.28	9.92	10.2	9.73	9.71	10.5
Na_2O	4.56	3.83	3.25	3.26	3.19	3.07
K_2O	2.41	1.53	0.81	0.6	0.61	0.86
P_2O_5	0.85	1.04	0.36	0.36	0.37	0.4
LOI	1.12	0.522	0.482	<0.01	<0.01	0.171
Sum	99.96	100.23	100.26	101.41	100.77	100.73

Ag	<1	<1	<1	<1	<1	<1
As	<30	<30	<30	<30	<30	<30
Ba	275	308	183	184	208	194
Be	<5	<5	<5	<5	<5	<5
Bi	<0.1	<0.1	<0.1	<0.1	<0.1	<0.1
Cd	<0.2	<0.2	<0.2	<0.2	<0.2	<0.2
Ce	78.6	81.6	40.7	48.8	51.1	37.2
Co	39.4	44.1	46.3	48.1	48	43.6
Cr	140	210	280	310	310	160
Cs	0.2	0.1	0.4	<0.1	<0.1	<0.1
Cu	45	58	50	29	41	54
Dy	5.23	4.89	4.05	3.84	3.85	4.29
Er	2.65	2.16	1.93	1.98	2.03	2.11
Eu	2.38	2.56	1.64	1.61	1.62	1.87
Ga	19	18	19	19	19	20
Gd	6.92	7.08	4.83	4.74	4.69	5.14

Ge	<1	<1	1	1	1	1
Hf	7	4	3	3	3	3
Ho	1	0.86	0.76	0.75	0.76	0.81
In	<0.2	<0.2	<0.2	<0.2	<0.2	<0.2
La	41.5	41.6	21.1	26.8	28.6	18
Li	<10	<10	<10	<10	<10	<10
Lu	0.33	0.22	0.23	0.23	0.23	0.23
Mo	4	3	<2	<2	<2	<2
Nb	49	45	16	16	16	17
Nd	38.2	39.9	20.5	22.6	23.8	21.5
Ni	111	150	126	137	144	88
Pb	<5	<5	<5	<5	<5	<5
Pr	9.78	10.2	5.05	5.82	6.08	5.01
Rb	24.2	15.2	8.1	7.5	6.4	11.4
Sb	0.2	<0.1	<0.1	0.1	0.1	0.1
Sc	20	20	23	22	23	25
Sm	7	7.5	4.5	4.6	4.4	4.6
Sn	2	2	1	1	<1	1
Sr	919	1060	587	556	589	591
Ta	3.5	2.8	1	1	1.1	1.2
Tb	0.96	0.93	0.69	0.68	0.69	0.77
Th	5	3.3	2.2	3.7	3.9	2.1
Tl	<0.5	<0.5	<0.5	<0.5	<0.5	<0.5
Tm	0.36	0.27	0.27	0.28	0.26	0.28
U	1.6	1.12	0.63	0.88	0.64	0.67
V	178	187	197	191	200	229
W	<1	<1	<1	<1	<1	<1
Y	25	21.9	18.9	18.8	18.8	20.3
Yb	2.2	1.7	1.6	1.6	1.6	1.7
Zn	92	91	111	106	109	103
Zr	284	180	113	110	109	118

Note: Major elements in weight percent and trace elements in parts per million

R12 HA 02	R12 HA 03
36.732	37.063
36.543	36.621
Basalt	Basalt
47.2	50.2
2.44	2.16
15.4	16.5
13.1	11.6
0.04	0.03
0.16	0.16
8.05	5.59
9.62	8.33
3.51	3.55
1.19	1.39
0.44	0.4
<0.01	0.354
101.15	99.91
<1	<1
<30	<30
287	331
<5	<5
<0.1	<0.1
<0.2	<0.2
45.8	55.8
47.2	39.4
230	100
0.3	0.1
58	16
4.5	5.63
2.32	2.92
1.89	2.04
21	23
5.55	6.36

1	1
4	5
0.87	1.08
<0.2	<0.2
22.6	28.2
<10	10
0.28	0.38
<2	2
27	26
24.8	30.6
122	33
<5	7
6.02	7.32
20	22.7
<0.1	0.3
24	25
5.2	6.1
2	2
649	587
1.8	1.7
0.8	0.94
2.2	4.4
<0.5	<0.5
0.3	0.4
0.73	1.07
215	217
<1	<1
22	27.7
1.9	2.5
97	102
150	190

Run_ID	Sample	Material	CO2 laser po	40Ar	40Ar sd	39Ar
865-02A	R12 OS01	whole rock	0.1	-0.1990	0.3983	0.0064
865-02B	R12 OS01	whole rock	0.3	-0.5635	0.3983	0.2092
865-02C	R12 OS01	whole rock	0.5	-0.4188	0.3992	-0.0834
865-02D	R12 OS01	whole rock	0.7	6.2740	0.4052	0.1492
865-02E	R12 OS01	whole rock	0.9	66.9007	0.3989	3.1154
865-02F	R12 OS01	whole rock	1.1	56.8115	0.4026	4.5999
865-02G	R12 OS01	whole rock	1.3	25.5533	0.3943	4.3011
865-02H	R12 OS01	whole rock	1.5	15.9954	0.3941	3.1890
865-02I	R12 OS01	whole rock	1.7	12.7708	0.3939	2.7501
865-02J	R12 OS01	whole rock	1.9	11.5117	0.3935	2.0762
865-02K	R12 OS01	whole rock	2.5	36.2308	0.3947	2.5178
865-02L	R12 OS01	whole rock	3.0	33.6497	0.3994	2.1678
865-02M	R12 OS01	whole rock	4.0	527.8910	0.4254	16.7281
865-02N	R12 OS01	whole rock	5.0	197.7330	0.4080	8.6706
865-02O	R12 OS01	whole rock	6.0	66.3060	0.3998	3.3720

Plateau age = 0.046 ± 0.013 Ma, steps A-O, MSWD = 0.6, 100% of 39Ar. Integrated age = 0.04 ±

882-02A	R12 OS03	whole rock	0.1	-0.1766	0.3935	-0.1841
882-02B	R12 OS03	whole rock	0.3	-0.1670	0.3985	-0.1885
882-02C	R12 OS03	whole rock	0.5	-0.5906	0.3977	0.0310
882-02D	R12 OS03	whole rock	0.7	1.6306	0.3992	0.1250
882-02E	R12 OS03	whole rock	0.9	105.5190	0.4052	3.4394
882-02F	R12 OS03	whole rock	1.1	133.5860	0.4052	4.6887
882-02G	R12 OS03	whole rock	1.3	97.5470	0.4052	3.5623
882-02H	R12 OS03	whole rock	1.5	81.0361	0.4019	2.3027
882-02I	R12 OS03	whole rock	1.7	58.4496	0.3949	1.7006
882-02J	R12 OS03	whole rock	1.9	40.9107	0.3946	1.0119
882-02K	R12 OS03	whole rock	2.5	90.8228	0.4019	2.8557
882-02L	R12 OS03	whole rock	3.0	209.7410	0.4080	5.8725
882-02M	R12 OS03	whole rock	4.0	207.9860	0.4111	5.9189
882-02N	R12 OS03	whole rock	5.0	51.1968	0.3946	1.4274
882-02O	R12 OS03	whole rock	6.0	88.5523	0.4026	2.3478

Plateau age = 0.05 ± 0.02 Ma, steps A-O, MSWD = 1.0, 100% of 39Ar. Integrated age = 0.06 ± 0.

866-02A	R12 OS04	whole rock	0.1	-0.2946	0.3985	0.1267
866-02B	R12 OS04	whole rock	0.3	-0.4315	0.3985	-0.3751
866-02C	R12 OS04	whole rock	0.5	-0.6462	0.3983	-0.1068
866-02D	R12 OS04	whole rock	0.7	0.6176	0.3936	0.9875

866-02E	R12 OS04	whole rock	0.9	26.3600	0.3992	2.1260
866-02F	R12 OS04	whole rock	1.1	42.7790	0.3957	2.7894
866-02G	R12 OS04	whole rock	1.3	34.4750	0.3935	2.6468
866-02H	R12 OS04	whole rock	1.5	29.1529	0.3977	2.9845
866-02I	R12 OS04	whole rock	1.7	23.5637	0.3951	2.1264
866-02J	R12 OS04	whole rock	1.9	24.6632	0.3951	1.9935
866-02K	R12 OS04	whole rock	2.5	35.0803	0.3943	2.4561
866-02L	R12 OS04	whole rock	3.0	17.8728	0.3933	1.1112
866-02M	R12 OS04	whole rock	4.0	41.6482	0.4016	2.2147
866-02N	R12 OS04	whole rock	5.0	34.8882	0.3935	1.0721
866-02O	R12 OS04	whole rock	6.0	19.2220	0.3941	0.5807

Plateau age = 0.75 ± 0.06 Ma, steps F-O, MSWD = 0.5, 87.9% of 39Ar. Integrated age = 0.68 ± 0

869-02A	R12 OS05	whole rock	0.1	-0.2083	0.3996	-0.0689
869-02B	R12 OS05	whole rock	0.3	-0.0303	0.3937	0.1361
869-02C	R12 OS05	whole rock	0.5	-0.1549	0.3992	0.2166
869-02D	R12 OS05	whole rock	0.7	0.6190	0.3979	0.2290
869-02E	R12 OS05	whole rock	0.9	23.0189	0.3957	2.4857
869-02F	R12 OS05	whole rock	1.1	40.8275	0.4026	4.0461
869-02G	R12 OS05	whole rock	1.3	42.2212	0.4021	4.1013
869-02H	R12 OS05	whole rock	1.5	33.3455	0.3936	3.0064
869-02I	R12 OS05	whole rock	1.7	22.1001	0.4007	1.9432
869-02J	R12 OS05	whole rock	1.9	26.2850	0.3952	1.4617
869-02K	R12 OS05	whole rock	2.5	38.8438	0.3941	1.0773
869-02L	R12 OS05	whole rock	3.0	34.4600	0.3937	0.6072
869-02M	R12 OS05	whole rock	4.0	44.1550	0.3996	0.4985
869-02N	R12 OS05	whole rock	5.0	19.6527	0.3940	0.2981
869-02O	R12 OS05	whole rock	6.0	29.8533	0.3923	0.3946

Plateau age = 0.81 ± 0.06 Ma, steps F-O, MSWD = 0.4, 85.3% of 39Ar. Integrated age = 0.74 ± 0

870-02A	R12 OS06	whole rock	0.1	-0.3483	0.3994	0.1853
870-02B	R12 OS06	whole rock	0.3	-0.7100	0.3987	-0.4520
870-02C	R12 OS06	whole rock	0.5	-0.7450	0.3996	-0.4490
870-02D	R12 OS06	whole rock	0.7	0.1622	0.3983	0.0331
870-02E	R12 OS06	whole rock	0.9	24.4374	0.3947	2.0992
870-02F	R12 OS06	whole rock	1.1	35.2019	0.3943	3.8978
870-02G	R12 OS06	whole rock	1.3	39.2775	0.3944	4.2021
870-02H	R12 OS06	whole rock	1.5	26.1331	0.3933	2.8373
870-02I	R12 OS06	whole rock	1.7	14.8068	0.3941	1.4151

870-02J	R12 OS06	whole rock	1.9	9.8128	0.3985	0.6980
870-02K	R12 OS06	whole rock	2.5	25.3349	0.3947	1.2685
870-02L	R12 OS06	whole rock	3.0	23.8623	0.3943	0.4946
870-02M	R12 OS06	whole rock	4.0	22.7759	0.3944	0.3637
870-02N	R12 OS06	whole rock	5.0	8.4471	0.3996	0.1931
870-02O	R12 OS06	whole rock	6.0	35.4605	0.3939	0.2117

Plateau age = 0.78 ± 0.06 Ma, steps F-O, MSWD = 0.4, 91.7% of 39Ar. Integrated age = 0.83 ± 0

875-02A	R12 HA01	whole rock	0.1	-0.1587	0.3987	0.2218
875-02B	R12 HA01	whole rock	0.3	-0.5097	0.3931	-0.1296
875-02C	R12 HA01	whole rock	0.5	-0.6066	0.3977	-0.4878
875-02D	R12 HA01	whole rock	0.7	0.2114	0.3981	0.0344
875-02E	R12 HA01	whole rock	0.9	48.1310	0.4111	0.8346
875-02F	R12 HA01	whole rock	1.1	54.1874	0.4012	1.1316
875-02G	R12 HA01	whole rock	1.3	55.3989	0.4026	1.1175
875-02H	R12 HA01	whole rock	1.5	52.6430	0.3996	1.0584
875-02I	R12 HA01	whole rock	1.7	45.7695	0.4012	0.5009
875-02J	R12 HA01	whole rock	1.9	36.6241	0.3935	0.7180
875-02K	R12 HA01	whole rock	2.5	322.5240	0.4111	3.5757
875-02L	R12 HA01	whole rock	3.0	536.1970	0.4215	4.7303
875-02M	R12 HA01	whole rock	4.0	584.6410	0.4338	5.0924
875-02N	R12 HA01	whole rock	5.0	269.5950	0.4144	2.4561
875-02O	R12 HA01	whole rock	6.0	372.2770	0.4215	2.8757

Plateau age = 2.63 ± 0.14 Ma, steps D-O, MSWD = 0.9, 101.7% of 39Ar. Integrated age = 2.8 ± (

884-02A	R12 HA02	whole rock	0.1	-0.2793	0.3996	0.1555
884-02B	R12 HA02	whole rock	0.3	-0.1877	0.3971	0.0177
884-02C	R12 HA02	whole rock	0.5	-0.0231	0.3936	0.3854
884-02D	R12 HA02	whole rock	0.7	0.4351	0.3998	-0.1847
884-02E	R12 HA02	whole rock	0.9	36.0552	0.3947	4.0931
884-02F	R12 HA02	whole rock	1.1	41.2442	0.3947	5.8970
884-02G	R12 HA02	whole rock	1.3	41.8315	0.4026	5.0788
884-02H	R12 HA02	whole rock	1.5	40.8670	0.4579	4.6183
884-02I	R12 HA02	whole rock	1.7	33.0439	0.3943	4.0171
884-02J	R12 HA02	whole rock	1.9	25.8905	0.4026	2.6865
884-02K	R12 HA02	whole rock	2.5	74.8168	0.4026	4.3258
884-02L	R12 HA02	whole rock	3.0	45.7107	0.3935	1.7247
884-02M	R12 HA02	whole rock	4.0	36.3744	0.4007	0.5032
884-02N	R12 HA02	whole rock	5.0	32.9729	0.3931	0.7517

884-02O	R12 HA02	whole rock	6.0	44.7776	0.3961	0.8773
884-02P	R12 HA02	whole rock	7.0	41.8508	0.3994	0.9284

Plateau age = 0.052 ± 0.017 Ma, steps F-N, MSWD = 0.3, 82.5% of 39Ar. Integrated age = 0.07 ±

887-02A	R12 HA03	whole rock	0.1	-0.5039	0.3931	-0.1698
887-02B	R12 HA03	whole rock	0.3	-0.3650	0.3943	0.2017
887-02C	R12 HA03	whole rock	0.5	-0.4786	0.3992	0.1902
887-02D	R12 HA03	whole rock	0.7	-0.6598	0.3994	-0.0013
887-02E	R12 HA03	whole rock	0.9	33.9484	0.3941	0.5699
887-02F	R12 HA03	whole rock	1.1	37.8065	0.3949	1.6116
887-02G	R12 HA03	whole rock	1.3	34.7580	0.3937	5.1828
887-02H	R12 HA03	whole rock	1.5	27.2288	0.3944	6.5583
887-02I	R12 HA03	whole rock	1.7	26.9394	0.3947	7.1887
887-02J	R12 HA03	whole rock	1.9	25.2613	0.3949	7.0719
887-02K	R12 HA03	whole rock	2.5	49.9146	0.3944	10.6898
887-02L	R12 HA03	whole rock	3.0	53.8593	0.4014	6.6038
887-02M	R12 HA03	whole rock	4.0	73.3447	0.4019	4.9591
887-02N	R12 HA03	whole rock	5.0	29.2023	0.3983	1.6642
887-02O	R12 HA03	whole rock	6.0	14.8935	0.3931	0.6571
887-02P	R12 HA03	whole rock	7.0	16.1232	0.3932	0.4348

Plateau age = 0.23 ± 0.01 Ma, steps F-P, MSWD = 0.8, 98.5% of 39Ar. Integrated age = 0.23 ± 0.

Monitors for sample data

868-11	FCT-A	sanidine	4.0	1576.3140	0.6742	5.8688
868-12	FCT-A	sanidine	0.0	7025.8150	1.3572	0.4618
868-13	FCT-A	sanidine	4.0	2304.9580	0.6420	8.5405
868-14	FCT-A	sanidine	4.0	1558.5670	0.5308	6.0620
868-15	FCT-A	sanidine	4.0	2604.0340	0.7072	10.1073
868-16	FCT-A	sanidine	4.0	1893.2260	0.5880	7.4272
868-17	FCT-A	sanidine	4.0	662.6170	0.4295	2.5814
868-18	FCT-A	sanidine	4.0	887.6470	0.4478	3.0431
868-19	FCT-A	sanidine	4.0	596.4680	0.4254	2.3677
868-20	FCT-A	sanidine	4.0	282.8150	0.4080	1.1402
868-21	FCT-A	sanidine	4.0	557.4870	0.4254	2.0243
881-10	FCT-B	sanidine	4.0	4228.1610	1.0177	16.5244
881-11	FCT-B	sanidine	4.0	3353.8950	0.8188	12.8207
881-12	FCT-B	sanidine	4.0	1764.4200	0.5308	6.7293
881-13	FCT-B	sanidine	4.0	4332.0290	1.0640	16.9342
881-14	FCT-B	sanidine	4.0	2194.7450	0.6263	8.4620
881-15	FCT-B	sanidine	4.0	2599.0250	0.6420	9.6620

881-16	FCT-B	sanidine	4.0	796.7530	0.4478	2.9662
881-17	FCT-B	sanidine	4.0	2854.5100	0.7926	10.9422
881-18	FCT-B	sanidine	4.0	2405.4890	0.6185	9.0414
894-10	FCT-C	sanidine	4.0	1834.8300	0.5515	6.9164
894-11	FCT-C	sanidine	4.0	2902.2600	0.8013	10.9256
894-12	FCT-C	sanidine	4.0	949.3380	0.4632	3.5163
894-13	FCT-C	sanidine	4.0	562.6810	0.4254	1.9838
894-14	FCT-C	sanidine	4.0	346.2900	0.4111	1.3532
894-15	FCT-C	sanidine	4.0	488.4230	0.4254	1.9969

39Ar sd	38Ar	38Ar sd	37Ar	37Ar sd	36Ar	36Arsd
0.2282	-0.0089	0.1472	0.0395	0.1358	-0.0003	0.0015
0.2293	-0.0015	0.1455	0.1006	0.1361	-0.0001	0.0015
0.2313	-0.0214	0.1472	0.0109	0.1370	0.0006	0.0015
0.2282	-0.0942	0.1463	0.0778	0.1367	0.0222	0.0016
0.2285	0.1656	0.1472	1.1011	0.1374	0.2210	0.0023
0.2287	0.1828	0.1460	1.4236	0.1374	0.1865	0.0024
0.2287	0.0655	0.1472	1.2142	0.1356	0.0793	0.0020
0.2382	0.0384	0.1482	0.9701	0.1367	0.0520	0.0019
0.2277	0.0100	0.1478	0.9564	0.1364	0.0408	0.0017
0.2274	0.0142	0.1485	0.7251	0.1377	0.0373	0.0017
0.2269	-0.0198	0.1488	1.4024	0.1358	0.1135	0.0021
0.2274	-0.0290	0.1466	1.1017	0.1356	0.1079	0.0021
0.2502	0.4728	0.1478	11.7661	0.1364	1.7455	0.0065
0.2277	0.2398	0.1460	7.7884	0.1367	0.6527	0.0036
0.2290	0.1238	0.1466	3.5221	0.1353	0.2185	0.0027

: 0.2 Ma.

0.2290	-0.1907	0.1458	0.0788	0.1370	-0.0013	0.0015
0.2307	0.0553	0.1460	-0.0238	0.1364	-0.0004	0.0015
0.2293	-0.0061	0.1472	0.0099	0.1350	-0.0010	0.0015
0.2406	0.1043	0.1469	0.0444	0.1361	0.0065	0.0015
0.2456	0.2053	0.1472	1.1365	0.1364	0.3513	0.0033
0.2277	0.1648	0.1482	2.1145	0.1358	0.4361	0.0035
0.2285	-0.0675	0.1458	1.7662	0.1361	0.3189	0.0026
0.2272	0.1086	0.1463	1.2947	0.1356	0.2699	0.0027
0.2267	0.2541	0.1469	0.9442	0.1350	0.1895	0.0024
0.2287	0.0030	0.1478	0.8543	0.1377	0.1343	0.0023
0.2310	0.1398	0.1452	3.5366	0.1374	0.3035	0.0029
0.2282	0.1145	0.1460	10.5188	0.1356	0.6919	0.0043
0.2414	0.2402	0.1466	12.9865	0.1370	0.7017	0.0038
0.2285	-0.2209	0.1482	3.8559	0.1361	0.1693	0.0024
0.2390	0.0595	0.1458	7.5930	0.1370	0.2933	0.0028

.03 Ma.

0.2293	0.0669	0.1455	-0.0189	0.1370	-0.0017	0.0015
0.2414	0.1357	0.1455	0.1999	0.1350	-0.0014	0.0015
0.2293	0.0249	0.1469	0.1007	0.1361	-0.0007	0.0015
0.2456	0.0229	0.1463	0.4446	0.1356	0.0079	0.0016

0.2502	0.2378	0.1472	2.4544	0.1370	0.0750	0.0021
0.2285	0.1027	0.1469	5.2919	0.1364	0.0749	0.0020
0.2279	-0.0808	0.1469	4.2252	0.1367	0.0497	0.0019
0.2414	-0.0143	0.1455	3.0736	0.1361	0.0367	0.0018
0.2310	0.0691	0.1466	2.3108	0.1356	0.0289	0.0017
0.2274	-0.0204	0.1469	2.0992	0.1358	0.0357	0.0016
0.2293	0.1668	0.1463	2.2040	0.1350	0.0620	0.0019
0.2414	-0.1334	0.1482	1.0632	0.1367	0.0356	0.0017
0.2406	0.1617	0.1452	2.3049	0.1361	0.0939	0.0020
0.2332	-0.1648	0.1458	2.0525	0.1361	0.0902	0.0019
0.2236	-0.0715	0.1460	1.0127	0.1353	0.0531	0.0019

.08 Ma.

0.2298	-0.0799	0.1469	0.1687	0.1356	-0.0007	0.0015
0.2456	0.0768	0.1485	0.1190	0.1370	-0.0006	0.0015
0.2293	0.0508	0.1469	0.1384	0.1367	0.0007	0.0015
0.2290	0.0572	0.1452	0.1430	0.1358	0.0007	0.0015
0.2502	0.3422	0.1482	4.0281	0.1358	0.0602	0.0019
0.2414	-0.1009	0.1466	7.4636	0.1358	0.0469	0.0018
0.2301	0.1044	0.1458	3.5467	0.1377	0.0399	0.0018
0.2394	0.0495	0.1482	2.5732	0.1356	0.0354	0.0017
0.2274	0.0642	0.1478	1.7849	0.1374	0.0272	0.0017
0.2296	-0.0557	0.1475	2.0462	0.1367	0.0462	0.0018
0.2290	-0.0616	0.1466	2.7869	0.1358	0.0982	0.0020
0.2262	0.1995	0.1460	2.2921	0.1348	0.1006	0.0021
0.2293	0.0781	0.1463	4.4776	0.1370	0.1377	0.0024
0.2307	-0.0726	0.1452	2.7736	0.1358	0.0609	0.0019
0.2243	0.0130	0.1463	4.7840	0.1374	0.0939	0.0019

.07 Ma.

0.2293	-0.1589	0.1466	-0.0496	0.1367	-0.0017	0.0015
0.2456	0.0317	0.1452	-0.0562	0.1370	-0.0013	0.0015
0.2456	-0.1370	0.1455	0.0025	0.1361	-0.0006	0.0015
0.2282	0.0558	0.1478	-0.0244	0.1358	0.0009	0.0015
0.2456	0.2586	0.1478	4.2758	0.1356	0.0543	0.0019
0.2414	-0.0448	0.1475	6.2062	0.1377	0.0337	0.0017
0.2298	0.0371	0.1450	3.7802	0.1380	0.0311	0.0017
0.2285	0.1280	0.1469	2.0943	0.1364	0.0194	0.0016
0.2298	0.0460	0.1482	1.7618	0.1364	0.0117	0.0016

0.2367	0.1069	0.1463	1.4624	0.1374	0.0101	0.0016
0.2414	0.0919	0.1472	3.3824	0.1356	0.0538	0.0019
0.2296	0.1568	0.1472	4.5754	0.1358	0.0663	0.0019
0.2269	0.0556	0.1472	6.0147	0.1370	0.0679	0.0019
0.2282	-0.0805	0.1472	3.2315	0.1364	0.0226	0.0017
0.2260	-0.0721	0.1472	9.1886	0.1367	0.1058	0.0021

.12 Ma.

0.2301	0.0003	0.1466	0.0762	0.1374	-0.0010	0.0015
0.2293	-0.1664	0.1463	0.0170	0.1361	0.0003	0.0015
0.2456	0.0939	0.1488	-0.0302	0.1353	-0.0008	0.0015
0.2307	0.1452	0.1475	0.1240	0.1374	0.0010	0.0016
0.2264	0.2853	0.1469	0.9499	0.1377	0.1163	0.0022
0.2382	0.0075	0.1469	1.9992	0.1380	0.0668	0.0019
0.2277	-0.0557	0.1460	1.6127	0.1380	0.0750	0.0019
0.2398	0.1153	0.1463	1.3670	0.1364	0.0943	0.0021
0.2279	0.0353	0.1478	1.0106	0.1358	0.0793	0.0021
0.2258	0.1129	0.1460	1.1815	0.1345	0.0678	0.0019
0.2414	0.2689	0.1463	5.6441	0.1374	0.7620	0.0042
0.2293	0.2795	0.1458	8.4057	0.1350	1.4300	0.0057
0.2277	0.2089	0.1463	14.4876	0.1367	1.5618	0.0064
0.2414	0.2303	0.1488	10.6967	0.1370	0.7205	0.0041
0.2277	0.0704	0.1472	17.5108	0.1370	1.0206	0.0048

.2 Ma.

0.2320	0.0441	0.1478	0.1331	0.1353	-0.0009	0.0015
0.2287	0.0426	0.1463	0.2167	0.1361	-0.0017	0.0015
0.2272	0.2428	0.1463	0.0327	0.1374	-0.0021	0.0015
0.2290	0.1402	0.1452	-0.0293	0.1361	0.0015	0.0015
0.2502	0.2252	0.1485	4.0198	0.1367	0.1255	0.0024
0.2287	0.0882	0.1472	5.4029	0.1377	0.1319	0.0022
0.2296	0.0677	0.1469	2.9420	0.1361	0.1326	0.0022
0.2307	0.0787	0.1458	2.1323	0.1364	0.1323	0.0022
0.2277	0.4059	0.1466	2.3299	0.1367	0.1041	0.0021
0.2287	0.0553	0.1482	1.9266	0.1361	0.0810	0.0020
0.2293	0.1141	0.1472	4.9690	0.1364	0.2460	0.0027
0.2282	-0.0603	0.1463	3.2285	0.1370	0.1513	0.0022
0.2258	-0.0080	0.1463	3.4715	0.1361	0.1199	0.0023
0.2255	-0.0753	0.1458	3.5161	0.1356	0.1107	0.0021

0.2262	-0.0224	0.1472	5.9034	0.1387	0.1355	0.0022
0.2253	-0.1642	0.1463	7.0506	0.1356	0.1370	0.0022

0.03 Ma.

0.2285	-0.0770	0.1488	-0.0102	0.1370	-0.0011	0.0015
0.2456	0.1565	0.1482	-0.0680	0.1374	-0.0023	0.0015
0.2301	0.0000	0.1469	-0.0140	0.1348	-0.0003	0.0015
0.2296	0.1584	0.1478	0.2092	0.1370	-0.0025	0.0015
0.2239	0.0071	0.1455	0.4960	0.1356	0.1155	0.0021
0.2410	0.0676	0.1463	2.4058	0.1358	0.1206	0.0023
0.2272	0.0516	0.1466	5.3656	0.1364	0.0790	0.0019
0.2394	0.0825	0.1463	5.4486	0.1364	0.0467	0.0018
0.2287	0.1846	0.1455	4.9784	0.1364	0.0387	0.0017
0.2290	0.0810	0.1466	4.1127	0.1361	0.0367	0.0017
0.2307	0.3519	0.1475	4.4183	0.1361	0.0914	0.0020
0.2282	0.2368	0.1463	2.6273	0.1356	0.1359	0.0022
0.2279	0.2468	0.1478	6.7378	0.1367	0.2115	0.0025
0.2269	-0.0306	0.1482	3.2867	0.1374	0.0825	0.0019
0.2247	-0.1672	0.1463	1.9845	0.1374	0.0444	0.0017
0.2247	-0.0810	0.1460	3.1103	0.1367	0.0486	0.0018

.08 Ma.

0.2293	0.0086	0.1482	-0.0381	0.1370	0.0106	0.0017
0.2269	-0.0551	0.1478	0.2431	0.1361	0.0836	0.0024
0.2299	0.2491	0.1458	0.1467	0.1374	0.0080	0.0017
0.2298	0.1433	0.1475	0.0678	0.1367	0.0074	0.0017
0.2304	0.1755	0.1460	0.1742	0.1364	0.0104	0.0017
0.2502	0.0747	0.1469	0.0829	0.1358	0.0075	0.0017
0.2287	-0.0473	0.1488	0.0478	0.1377	0.0033	0.0016
0.2406	-0.0116	0.1472	-0.0178	0.1361	0.0039	0.0017
0.2285	0.1039	0.1475	-0.0256	0.1353	0.0048	0.0017
0.2290	0.1225	0.1452	0.1108	0.1364	0.0014	0.0016
0.2287	-0.0550	0.1469	0.1447	0.1361	0.0066	0.0016
0.2457	0.1723	0.1482	0.2197	0.1345	0.0263	0.0019
0.2316	0.2654	0.1469	0.2130	0.1353	0.0100	0.0017
0.2307	0.0832	0.1478	0.2724	0.1358	0.0216	0.0018
0.2398	0.2277	0.1472	0.2433	0.1364	0.0276	0.0019
0.2310	0.1924	0.1466	0.2126	0.1370	0.0075	0.0017
0.2343	0.2291	0.1469	0.2366	0.1364	0.0230	0.0018

0.2290	-0.0256	0.1475	0.0431	0.1356	0.0038	0.0016
0.2293	0.2378	0.1466	0.0113	0.1367	0.0253	0.0019
0.2279	0.1831	0.1466	0.0889	0.1350	0.0163	0.0017
0.2290	0.1031	0.1466	0.0880	0.1367	0.0063	0.0017
0.2301	0.0813	0.1463	0.3176	0.1370	0.0146	0.0018
0.2290	0.0218	0.1472	0.1964	0.1361	0.0030	0.0016
0.2282	-0.1118	0.1460	0.0993	0.1356	0.0078	0.0016
0.2398	0.0747	0.1475	0.0490	0.1374	0.0017	0.0015
0.2296	-0.0367	0.1466	-0.0040	0.1367	0.0015	0.0016

Ca/K	%40Ar rad	Age	Age sd	39Ar moles	Irradiation	J
20.99481	58.33556	-1.994806	72.89487	1.94E-19	DT-15a	0.0000593
1.624895	93.59872	-0.2735001	0.4346668	6.38E-18	DT-15a	0.0000593
-0.4435368	140.0848	0.7628916	2.260844	-2.54E-18	DT-15a	0.0000593
1.76375	-5.575563	-0.2543508	0.5992777	4.55E-18	DT-15a	0.0000593
1.195619	1.596568	0.0371884	0.0281646	9.50E-17	DT-15a	0.0000593
1.047153	2.308473	0.0309245	0.0194735	1.40E-16	DT-15a	0.0000593
0.9554494	7.975068	0.0513889	0.0182073	1.31E-16	DT-15a	0.0000593
1.029836	3.625197	0.019722	0.0231411	9.72E-17	DT-15a	0.0000593
1.17764	5.579742	0.0281051	0.0256919	8.38E-17	DT-15a	0.0000593
1.182981	4.099094	0.0246533	0.0337677	6.33E-17	DT-15a	0.0000593
1.887067	6.956182	0.1086014	0.0338917	7.68E-17	DT-15a	0.0000593
1.722307	4.68274	0.0788589	0.0386806	6.61E-17	DT-15a	0.0000593
2.384175	1.559082	0.0533883	0.0129882	5.10E-16	DT-15a	0.0000593
3.045531	1.930875	0.0477925	0.0145795	2.64E-16	DT-15a	0.0000593
3.542323	2.270049	0.0484556	0.0295538	1.03E-16	DT-15a	0.0000593
-1.471781	-127.8145	-0.1312344	0.3842189	-5.61E-18	DT-15c	0.0000585
0.4349875	25.36001	0.0240664	0.344612	-5.75E-18	DT-15c	0.0000585
1.104068	47.02257	-0.9600012	7.404042	9.45E-19	DT-15c	0.0000585
1.222999	-18.37057	-0.2567734	0.72039	3.81E-18	DT-15c	0.0000585
1.137094	0.7295749	0.0239766	0.0334662	1.05E-16	DT-15c	0.0000585
1.552266	2.738291	0.083582	0.0257184	1.43E-16	DT-15c	0.0000585
1.706925	2.609439	0.0765559	0.02706	1.09E-16	DT-15c	0.0000585
1.936204	0.7785817	0.0293587	0.0418571	7.02E-17	DT-15c	0.0000585
1.91237	3.429692	0.1262988	0.0543298	5.18E-17	DT-15c	0.0000585
2.908663	2.235736	0.096886	0.0869057	3.08E-17	DT-15c	0.0000585
4.267627	0.7309502	0.0249283	0.0356171	8.71E-17	DT-15c	0.0000585
6.173904	2.146035	0.0822423	0.0246646	1.79E-16	DT-15c	0.0000585
7.564285	0.0650099	0.0024524	0.022149	1.80E-16	DT-15c	0.0000585
9.315146	2.228134	0.0858401	0.0630536	4.35E-17	DT-15c	0.0000585
11.15513	2.187189	0.0886661	0.0432335	7.16E-17	DT-15c	0.0000585
-0.5066588	-70.03711	0.1765784	0.6053953	3.86E-18	DT-15a	0.0000593
-1.808358	-4.101151	-0.0051118	0.1740613	-1.14E-17	DT-15a	0.0000593
-3.200282	65.17983	0.4271061	1.101338	-3.26E-18	DT-15a	0.0000593
1.52875	-273.3736	-0.185483	0.083154	3.01E-17	DT-15a	0.0000593

3.921166	16.20966	0.2181896	0.0454644	6.48E-17	DT-15a	0.0000593
6.445504	49.29623	0.8213333	0.07292	8.50E-17	DT-15a	0.0000593
5.424875	58.50023	0.8275052	0.076614	8.07E-17	DT-15a	0.0000593
3.500699	63.77857	0.676168	0.0598524	9.10E-17	DT-15a	0.0000593
3.694786	64.65821	0.77768	0.0906409	6.48E-17	DT-15a	0.0000593
3.581169	57.88866	0.7773099	0.0951822	6.08E-17	DT-15a	0.0000593
3.052636	48.00169	0.7440035	0.0760077	7.49E-17	DT-15a	0.0000593
3.255754	41.27701	0.7205034	0.1686744	3.39E-17	DT-15a	0.0000593
3.542149	33.35292	0.6807369	0.0819754	6.75E-17	DT-15a	0.0000593
6.517772	23.57856	0.8336213	0.1949683	3.27E-17	DT-15a	0.0000593
5.938656	18.14481	0.652436	0.2832723	1.77E-17	DT-15a	0.0000593

-8.351647	-9.571015	-0.0316088	0.9594585	-2.10E-18	DT-15b	0.0000599
2.984234	-540.4586	0.1320194	0.5388276	4.15E-18	DT-15b	0.0000599
2.181793	213.9376	-0.1678625	0.3537798	6.60E-18	DT-15b	0.0000599
2.133006	68.745	0.2038362	0.3549853	6.98E-18	DT-15b	0.0000599
5.535125	24.17407	0.245844	0.0395207	7.58E-17	DT-15b	0.0000599
6.302101	67.98202	0.7534058	0.0485558	1.23E-16	DT-15b	0.0000599
2.955068	72.86263	0.8228698	0.049544	1.25E-16	DT-15b	0.0000599
2.925451	69.28285	0.842996	0.0710758	9.16E-17	DT-15b	0.0000599
3.140265	64.32684	0.8026274	0.1009449	5.92E-17	DT-15b	0.0000599
4.786944	48.49703	0.9572833	0.1585924	4.46E-17	DT-15b	0.0000599
8.848017	25.43058	1.007848	0.2268625	3.28E-17	DT-15b	0.0000599
12.91457	13.71775	0.8569099	0.346989	1.85E-17	DT-15b	0.0000599
30.73525	8.186352	0.8029462	0.4148899	1.52E-17	DT-15b	0.0000599
31.84155	9.319985	0.6806063	0.5891369	9.09E-18	DT-15b	0.0000599
41.50508	8.12366	0.6831044	0.4398811	1.20E-17	DT-15b	0.0000599

-0.9160066	-41.00867	0.0844772	0.376302	5.65E-18	DT-15b	0.0000599
0.4255732	45.01975	0.0775239	0.1525123	-1.38E-17	DT-15b	0.0000599
-0.0187938	77.42605	0.140805	0.1675276	-1.37E-17	DT-15b	0.0000599
-2.53116	-68.4014	-0.3673487	3.223095	1.01E-18	DT-15b	0.0000599
6.983187	35.88648	0.4589706	0.0645156	6.40E-17	DT-15b	0.0000599
5.460002	73.61395	0.7299737	0.0488328	1.19E-16	DT-15b	0.0000599
3.085635	77.58152	0.7955752	0.0465839	1.28E-16	DT-15b	0.0000599
2.532437	78.81235	0.7962509	0.0686183	8.65E-17	DT-15b	0.0000599
4.272206	77.92251	0.8948339	0.1531641	4.31E-17	DT-15b	0.0000599

7.191058	71.17022	1.099097	0.3864072	2.13E-17	DT-15b	0.0000599
9.15453	38.23758	0.8395714	0.1707078	3.87E-17	DT-15b	0.0000599
31.76357	19.41293	1.037365	0.5097544	1.51E-17	DT-15b	0.0000599
56.80058	14.37369	1.005605	0.6742758	1.11E-17	DT-15b	0.0000599
57.48512	24.96543	1.220142	1.515669	5.89E-18	DT-15b	0.0000599
149.1444	14.20555	2.743839	3.108219	6.45E-18	DT-15b	0.0000599

1.220092	-103.6103	0.0812806	0.3104334	6.76E-18	DT-15b	0.0000599
-0.4667423	115.4822	0.4975299	1.013855	-3.95E-18	DT-15b	0.0000599
0.2201904	60.95666	0.0830982	0.1409042	-1.49E-17	DT-15b	0.0000599
12.81718	-26.67485	-0.1806152	2.314155	1.05E-18	DT-15b	0.0000599
4.044133	28.15078	1.78111	0.4944466	2.54E-17	DT-15b	0.0000599
6.278969	63.70293	3.347966	0.708959	3.45E-17	DT-15b	0.0000599
5.13032	59.98194	3.262388	0.6687989	3.41E-17	DT-15b	0.0000599
4.592281	46.84745	2.556279	0.5845921	3.23E-17	DT-15b	0.0000599
7.175449	48.56841	4.869953	2.224264	1.53E-17	DT-15b	0.0000599
5.85401	45.13608	2.527057	0.8026897	2.19E-17	DT-15b	0.0000599
5.616303	29.68836	2.938603	0.2026106	1.09E-16	DT-15b	0.0000599
6.324187	20.57851	2.560652	0.1308451	1.44E-16	DT-15b	0.0000599
10.12728	20.56883	2.595543	0.1237496	1.55E-16	DT-15b	0.0000599
15.50713	20.72683	2.5053	0.2541053	7.49E-17	DT-15b	0.0000599
21.68639	18.7669	2.680745	0.2213133	8.77E-17	DT-15b	0.0000599

3.084749	-1.902024	0.0036624	0.4158974	4.74E-18	DT-15c	0.0000585
44.17557	-187.2427	2.158904	28.56404	5.39E-19	DT-15c	0.0000585
0.3059837	-2631.678	0.168925	0.1950863	1.17E-17	DT-15c	0.0000585
0.57129	-2.833982	0.0071505	0.3515114	-5.63E-18	DT-15c	0.0000585
3.542474	-2.409953	-0.0227585	0.0213661	1.25E-16	DT-15c	0.0000585
3.305571	6.221343	0.0466433	0.0138352	1.80E-16	DT-15c	0.0000585
2.090433	6.3217	0.055792	0.0162036	1.55E-16	DT-15c	0.0000585
1.666508	4.06168	0.0385061	0.0184126	1.41E-16	DT-15c	0.0000585
2.093991	6.867176	0.0605278	0.0198616	1.22E-16	DT-15c	0.0000585
2.589681	7.635062	0.0788546	0.0294434	8.19E-17	DT-15c	0.0000585
4.149148	2.694391	0.0499684	0.0223333	1.32E-16	DT-15c	0.0000585
6.763171	2.108024	0.059961	0.0476811	5.26E-17	DT-15c	0.0000585
24.9311	2.826391	0.2206076	0.1978149	1.53E-17	DT-15c	0.0000585
16.90843	1.153568	0.0544937	0.1063286	2.29E-17	DT-15c	0.0000585

24.32765	11.41715	0.6289894	0.1892557	2.67E-17	DT-15c	0.0000585
27.46332	4.471162	0.217816	0.10306	2.83E-17	DT-15c	0.0000585

0.2333938	34.5698	0.1098635	0.405164	-5.18E-18	DT-15c	0.0000585
-1.303923	-87.99503	0.1704425	0.3781406	6.15E-18	DT-15c	0.0000585
-0.2846733	78.96422	-0.2128032	0.4250293	5.80E-18	DT-15c	0.0000585
-627.0653	-19.65094	-8.900016	1310.441	-3.94E-20	DT-15c	0.0000585
3.369706	-1.340934	-0.0856354	0.1421552	1.74E-17	DT-15c	0.0000585
5.780676	5.65824	0.1423981	0.0569404	4.91E-17	DT-15c	0.0000585
4.009806	34.36365	0.2470763	0.0180337	1.58E-16	DT-15c	0.0000585
3.218624	51.69476	0.2300461	0.013725	2.00E-16	DT-15c	0.0000585
2.683611	59.73714	0.2399034	0.0122689	2.19E-16	DT-15c	0.0000585
2.25407	58.95336	0.2256406	0.0122587	2.16E-16	DT-15c	0.0000585
1.602376	46.60756	0.2331369	0.0087556	3.26E-16	DT-15c	0.0000585
1.542727	25.34451	0.2214307	0.0144887	2.01E-16	DT-15c	0.0000585
5.2698	15.20009	0.2411241	0.0214189	1.51E-16	DT-15c	0.0000585
7.662025	17.24398	0.3248089	0.0632935	5.07E-17	DT-15c	0.0000585
11.71952	12.92507	0.3149017	0.151142	2.00E-17	DT-15c	0.0000585
27.76188	12.65723	0.5071739	0.3116414	1.33E-17	DT-15c	0.0000585

-0.0178978	99.79959	28.83768	1.117895	1.79E-16	DT-15a	0.0000593
1.451758	99.64501	1173.459	425.9179	1.41E-17	DT-15a	0.0000593
0.0520501	99.89666	29.00335	0.7744993	2.60E-16	DT-15a	0.0000593
0.0338919	99.85866	27.62962	1.039848	1.85E-16	DT-15a	0.0000593
0.0522492	99.8818	27.69305	0.6266965	3.08E-16	DT-15a	0.0000593
0.0339837	99.88177	27.40108	0.9163599	2.26E-16	DT-15a	0.0000593
0.0563348	99.85363	27.58355	2.425928	7.87E-17	DT-15a	0.0000593
-0.017839	99.86734	31.3168	2.454874	9.28E-17	DT-15a	0.0000593
-0.0330517	99.75862	27.04822	2.590798	7.22E-17	DT-15a	0.0000593
0.2970538	99.85302	26.663	5.31714	3.48E-17	DT-15a	0.0000593
0.2185366	99.6469	29.51904	3.309085	6.17E-17	DT-15a	0.0000593
0.0403301	99.81459	27.78634	0.4100287	5.04E-16	DT-15b	0.0000599
0.0504085	99.91195	28.43086	0.5098003	3.91E-16	DT-15b	0.0000599
0.1228569	99.63619	28.41837	0.9669898	2.05E-16	DT-15b	0.0000599
0.0437668	99.81026	27.77883	0.3904601	5.16E-16	DT-15b	0.0000599
0.0765426	99.8994	28.18662	0.7637557	2.58E-16	DT-15b	0.0000599
0.0746347	99.73737	29.17773	0.7018925	2.95E-16	DT-15b	0.0000599

0.0444911	99.85827	29.17108	2.234442	9.04E-17	DT-15b	0.0000599
0.0031674	99.73543	28.30221	0.5885654	3.34E-16	DT-15b	0.0000599
0.0300743	99.79837	28.87825	0.7223809	2.76E-16	DT-15b	0.0000599
0.0386248	99.89826	28.16157	0.9253794	2.11E-16	DT-15c	0.0000585
0.0882996	99.85122	28.18609	0.589265	3.33E-16	DT-15c	0.0000585
0.1697308	99.90796	28.66037	1.852226	1.07E-16	DT-15c	0.0000585
0.1526266	99.58927	30.00323	3.423518	6.05E-17	DT-15c	0.0000585
0.1103476	99.85163	27.161	4.777716	4.12E-17	DT-15c	0.0000585
-0.0061704	99.90841	25.98273	2.966094	6.09E-17	DT-15c	0.0000585

J sd	Isoch_36_Ov	Pct_i36_Over	Isoch_39_Ov	Pct_i39_Over_	Pct_i39_Over_	Correl_40_Ov
2.73E-06	0.00140	589.99580	-0.03173	-3620.00800	-3656.90400	0.14277
2.73E-06	0.00021	1270.86500	-0.37116	-130.45660	-1273.64100	0.99475
2.73E-06	-0.00134	-291.63750	0.19909	293.41070	-391.14530	0.66601
2.73E-06	0.00354	9.68535	0.02377	153.15230	153.18530	0.03511
2.73E-06	0.00330	1.21823	0.04656	7.36034	7.41257	0.12496
2.73E-06	0.00327	1.47525	0.08095	5.02452	5.13971	0.22078
2.73E-06	0.00308	2.96389	0.16830	5.53888	5.89061	0.36677
2.73E-06	0.00323	4.35154	0.19934	7.86866	8.28867	0.35664
2.73E-06	0.00316	5.27115	0.21530	8.83757	9.31968	0.37196
2.73E-06	0.00321	5.74768	0.18032	11.47894	11.89229	0.31239
2.73E-06	0.00312	2.19198	0.06946	9.08431	9.21695	0.17906
2.73E-06	0.00319	2.32360	0.06440	10.56405	10.68537	0.16072
2.73E-06	0.00330	0.38426	0.03167	1.49924	1.54348	0.23800
2.73E-06	0.00328	0.59690	0.04381	2.63661	2.68751	0.19555
2.73E-06	0.00327	1.40173	0.05081	6.82604	6.91601	0.16517
2.91E-06	0.00763	249.37440	1.04314	255.13900	167.35210	0.30072
2.91E-06	0.00250	435.53870	1.12857	268.21940	384.35140	0.79295
2.91E-06	0.00177	159.34140	-0.05247	-743.03890	-753.96020	0.17359
2.91E-06	0.00396	34.26463	0.07663	194.12610	194.06000	0.08645
2.91E-06	0.00333	1.02341	0.03259	7.15521	7.20753	0.12200
2.91E-06	0.00326	0.85236	0.03509	4.86783	4.92319	0.15120
2.91E-06	0.00326	0.92628	0.03651	6.43041	6.47010	0.11437
2.91E-06	0.00332	1.11432	0.02840	9.88445	9.92223	0.09006
2.91E-06	0.00323	1.44106	0.02908	13.35514	13.39853	0.08391
2.91E-06	0.00327	1.97409	0.02471	22.64778	22.69254	0.06623
2.91E-06	0.00332	1.04895	0.03140	8.11379	8.15727	0.10571
2.91E-06	0.00328	0.65075	0.02795	3.89875	3.94307	0.15028
2.91E-06	0.00335	0.58728	0.02839	4.09350	4.12592	0.12621
2.91E-06	0.00327	1.62499	0.02780	16.07387	16.11886	0.07813
2.91E-06	0.00328	1.06151	0.02642	10.22829	10.26303	0.08445
2.73E-06	0.00570	162.34530	-0.43012	-225.95050	-202.02490	0.24564
2.73E-06	0.00349	136.55670	0.87007	112.54220	119.37950	0.62059
2.73E-06	0.00117	210.54270	0.16548	223.13910	294.12330	0.65443
2.73E-06	0.01251	67.19597	1.59844	68.41560	32.76143	0.20622

2.73E-06	0.00281	3.17464	0.08056	11.88202	12.11066	0.20249
2.73E-06	0.00170	2.89401	0.06508	8.26013	8.65385	0.30024
2.73E-06	0.00139	4.02880	0.07665	8.70250	9.45264	0.39199
2.73E-06	0.00121	5.23101	0.10227	8.21186	9.54285	0.51084
2.73E-06	0.00118	6.25070	0.09015	11.00672	12.43308	0.46655
2.73E-06	0.00141	5.00133	0.08075	11.53365	12.36501	0.36297
2.73E-06	0.00174	3.33790	0.06995	9.41229	9.85900	0.30016
2.73E-06	0.00197	5.29124	0.06212	21.85841	22.27275	0.19646
2.73E-06	0.00223	2.35420	0.05312	10.91830	11.08542	0.17673
2.73E-06	0.00256	2.43421	0.03067	21.83405	21.91113	0.08725
2.73E-06	0.00274	4.17858	0.03016	38.63094	38.74754	0.08187

1.02E-06	0.00367	274.96580	0.33199	383.81590	386.39860	0.36523
1.02E-06	0.02145	1320.10500	-4.48831	-1311.90800	-294.73110	0.13935
1.02E-06	-0.00382	-363.70530	-1.39742	-278.61460	277.66220	0.65232
1.02E-06	0.00105	245.16360	0.36975	118.94370	256.86850	0.88877
1.02E-06	0.00254	3.70685	0.10780	10.23096	10.60638	0.27431
1.02E-06	0.00107	4.19999	0.09891	6.05947	7.23922	0.54815
1.02E-06	0.00091	4.75171	0.09706	5.69706	7.29486	0.62517
1.02E-06	0.00103	5.02280	0.09009	8.05733	9.34628	0.50770
1.02E-06	0.00119	6.75794	0.08785	11.85508	13.40222	0.46792
1.02E-06	0.00173	4.21903	0.05553	15.80230	16.21657	0.22712
1.02E-06	0.00250	2.29561	0.02766	21.34433	21.41920	0.08623
1.02E-06	0.00289	2.37199	0.01755	37.43442	37.47447	0.04861
1.02E-06	0.00308	1.97764	0.01118	46.48094	46.50524	0.03362
1.02E-06	0.00304	3.69606	0.01501	78.25239	78.28796	0.03332
1.02E-06	0.00308	2.47553	0.01304	57.66066	57.68363	0.03083

1.02E-06	0.00472	148.40180	-0.53223	-168.67550	-155.50770	0.38462
1.02E-06	0.00184	129.18530	0.63670	78.15335	128.40230	0.81591
1.02E-06	0.00076	278.83470	0.60287	76.61114	279.03450	0.96228
1.02E-06	0.00564	296.09600	0.20418	731.63060	708.73890	0.13040
1.02E-06	0.00215	3.88171	0.08572	11.84016	12.24862	0.26202
1.02E-06	0.00088	5.65869	0.11055	6.30473	8.32181	0.65330
1.02E-06	0.00075	5.71148	0.10689	5.56690	7.84772	0.70524
1.02E-06	0.00071	9.00469	0.10850	8.19835	11.98954	0.73001
1.02E-06	0.00074	14.72951	0.09545	16.48233	21.78055	0.65414

1.02E-06	0.00097	17.62606	0.07098	34.23939	38.07719	0.43830
1.02E-06	0.00207	3.86230	0.04992	19.15244	19.41294	0.16657
1.02E-06	0.00270	3.31969	0.02051	46.93918	46.99804	0.05313
1.02E-06	0.00287	3.41346	0.01567	63.62970	63.67379	0.03981
1.02E-06	0.00251	9.21585	0.02243	120.57570	120.74130	0.05622
1.02E-06	0.00287	2.38050	0.00567	112.38110	112.39510	0.01657

1.02E-06	0.00682	287.89260	-1.39759	-271.84100	-174.72980	0.39275
1.02E-06	-0.00052	-573.63330	0.25446	192.90660	-595.31800	0.94620
1.02E-06	0.00131	199.99310	0.80426	82.67579	195.52950	0.91286
1.02E-06	0.00424	256.91800	0.16194	699.94670	696.39470	0.17069
1.02E-06	0.00241	2.10181	0.01732	27.18222	27.23640	0.06442
1.02E-06	0.00122	3.00894	0.02084	21.11074	21.29804	0.13272
1.02E-06	0.00134	2.68972	0.02014	20.42249	20.57290	0.12119
1.02E-06	0.00178	2.33408	0.02008	22.70204	22.79621	0.09156
1.02E-06	0.00172	2.76199	0.01092	45.62226	45.68869	0.05436
1.02E-06	0.00184	3.05043	0.01957	31.52388	31.63434	0.08447
1.02E-06	0.00236	0.56223	0.01107	6.76486	6.78576	0.07860
1.02E-06	0.00266	0.40950	0.00881	4.85804	4.87398	0.08092
1.02E-06	0.00266	0.41668	0.00868	4.48673	4.50480	0.08956
1.02E-06	0.00266	0.59587	0.00906	9.88110	9.89663	0.05620
1.02E-06	0.00272	0.49121	0.00767	7.97612	7.98961	0.05821

2.91E-06	0.00341	213.71910	-0.55621	-206.81430	-217.98810	0.54111
2.91E-06	0.00962	227.07240	-0.09283	-1329.87600	-1315.53400	0.02274
2.91E-06	0.09150	1705.37400	-16.68447	-1704.85000	-93.48384	0.03301
2.91E-06	0.00344	137.11800	-0.42448	-154.35140	-160.44500	0.47085
2.91E-06	0.00343	2.21700	0.11341	6.21778	6.41687	0.26123
2.91E-06	0.00314	1.91806	0.14285	3.99926	4.22370	0.34103
2.91E-06	0.00314	1.90222	0.12135	4.62447	4.81143	0.29413
2.91E-06	0.00321	1.98613	0.11297	5.12280	5.26069	0.25736
2.91E-06	0.00312	2.33694	0.12151	5.79580	6.01685	0.28713
2.91E-06	0.00309	2.93489	0.10370	8.66206	8.87714	0.23778
2.91E-06	0.00326	1.22209	0.05775	5.33498	5.41991	0.18176
2.91E-06	0.00328	1.67875	0.03765	13.28927	13.33930	0.09276
2.91E-06	0.00325	2.23571	0.01372	45.25781	45.28601	0.03738
2.91E-06	0.00331	2.24213	0.02267	30.20036	30.23631	0.05319

2.91E-06	0.00297	1.89749	0.01944	26.01176	26.05069	0.05701
2.91E-06	0.00320	1.87100	0.02198	24.51458	24.54864	0.05639

2.91E-06	0.00219	157.42090	0.33700	155.54340	191.83160	0.61907
2.91E-06	0.00630	126.10870	-0.55291	-162.76500	-138.05840	0.24321
2.91E-06	0.00070	453.33780	-0.39744	-146.97310	-461.76100	0.94857
2.91E-06	0.00401	83.41140	0.00237	14681.06000	14681.03000	0.00269
2.91E-06	0.00339	2.14222	0.01677	39.35625	39.38007	0.03842
2.91E-06	0.00316	2.19296	0.04256	15.01851	15.10550	0.11224
2.91E-06	0.00220	2.76098	0.14895	4.53288	5.05973	0.45380
2.91E-06	0.00162	4.30886	0.24066	3.93081	5.46043	0.69986
2.91E-06	0.00135	4.91267	0.26667	3.50563	5.66790	0.78958
2.91E-06	0.00137	5.21053	0.27981	3.59802	5.93322	0.79909
2.91E-06	0.00179	2.37187	0.21410	2.29964	3.10869	0.67824
2.91E-06	0.00250	1.76506	0.12258	3.53672	3.80941	0.38071
2.91E-06	0.00284	1.31758	0.06751	4.63689	4.75764	0.22904
2.91E-06	0.00277	2.74142	0.05685	13.73910	13.87619	0.14865
2.91E-06	0.00292	4.75057	0.04396	34.43263	34.55725	0.09504
2.91E-06	0.00293	4.50754	0.02672	52.21673	52.29679	0.06096

2.73E-06	0.00001	16.23132	0.00372	3.90699	16.69453	0.97223
2.73E-06	0.00001	2.83814	0.00007	49.16704	49.24873	0.05763
2.73E-06	0.00000	21.52900	0.00371	2.69150	21.69631	0.99228
2.73E-06	0.00000	22.44586	0.00389	3.79187	22.76348	0.98603
2.73E-06	0.00000	16.71692	0.00388	2.28009	16.87144	0.99083
2.73E-06	0.00000	22.52950	0.00392	3.36924	22.77966	0.98900
2.73E-06	0.00000	48.66704	0.00390	8.86098	49.46615	0.98383
2.73E-06	0.00000	42.54075	0.00343	7.90589	43.26830	0.98317
2.73E-06	0.00001	34.34235	0.00397	9.64903	35.67107	0.96272
2.73E-06	0.00000	112.24640	0.00403	20.08693	114.02720	0.98436
2.73E-06	0.00001	23.97951	0.00363	11.30032	26.50747	0.90459
1.02E-06	0.00001	7.29317	0.00391	1.48682	7.44298	0.97985
1.02E-06	0.00000	17.19061	0.00382	1.80702	17.28512	0.99452
1.02E-06	0.00001	8.59476	0.00381	3.42903	9.25317	0.92880
1.02E-06	0.00001	6.95632	0.00391	1.41623	7.09882	0.97990
1.02E-06	0.00000	22.91481	0.00386	2.73046	23.07661	0.99298
1.02E-06	0.00001	8.08283	0.00372	2.42471	8.43840	0.95783

1.02E-06	0.00000	42.43032	0.00372	7.72075	43.12619	0.98384
1.02E-06	0.00001	7.57045	0.00383	2.09560	7.85487	0.96376
1.02E-06	0.00001	10.60988	0.00376	2.52116	10.90502	0.97291
2.91E-06	0.00000	26.92419	0.00377	3.31120	27.12669	0.99252
2.91E-06	0.00000	12.33442	0.00377	2.10668	12.51278	0.98573
2.91E-06	0.00000	54.01979	0.00370	6.51321	54.41032	0.99281
2.91E-06	0.00001	21.25836	0.00353	11.50394	24.17020	0.87948
2.91E-06	0.00000	88.61417	0.00391	17.72070	90.36657	0.98058
2.91E-06	0.00000	107.10860	0.00409	11.49643	107.72260	0.99429

Correl_36_Over_39
0.01876
0.03014
0.10616
0.02812
0.03966
0.06776
0.14503
0.17733
0.20418
0.17706
0.05961
0.05739
0.01127
0.02706
0.03800
0.78014
0.48749
0.03830
0.09009
0.02014
0.02218
0.02897
0.02233
0.02372
0.02081
0.02301
0.01492
0.01625
0.02274
0.01904
0.49888
0.55505
0.08088
0.88341

0.06079
0.03579
0.03715
0.04333
0.04086
0.04448
0.04021
0.04187
0.03618
0.02393
0.02605

0.34869
0.97494
0.65528
0.14172
0.07792
0.03821
0.03351
0.03442
0.04103
0.03391
0.02101
0.01470
0.00891
0.01390
0.01210

0.52523
0.31239
0.13467
0.27838
0.05677
0.03517
0.03172
0.03068
0.02919

0.02733
0.03282
0.01752
0.01381
0.02014
0.00461

0.80662
0.05374
0.26000
0.19723
0.01277
0.00863
0.00962
0.01087
0.00610
0.01200
0.00427
0.00311
0.00295
0.00401
0.00327

0.46308
0.14825
0.99850
0.39895
0.08695
0.11942
0.10531
0.12341
0.10512
0.09512
0.04442
0.03321
0.01199
0.02099

0.01585
0.01985

0.24850
0.56851
0.10440
0.00299
0.01599
0.03313
0.10253
0.12390
0.12467
0.13035
0.11449
0.08898
0.04914
0.04940
0.04258
0.02527

0.00003
0.00000
0.00001
0.00001
0.00002
0.00001
0.00001
0.00001
0.00002
0.00001
0.00002
0.00005
0.00002
0.00003
0.00006
0.00001
0.00003

0.00001
0.00005
0.00002
0.00001
0.00003
0.00001
0.00002
0.00001
0.00001

Table X: Pb-Sr-Nd data for basaltic whole-rock samples from Turkey

Sample Name		Sample Wgt (mg)	^{206}Pb/ ^{204}Pb †	error 2SE%	^{207}Pb/ ^{204}Pb †	error 2SE%	^{208}Pb/ ^{204}Pb †	error 2SE%	^{87}Sr/ ^{86}Sr §	error 2SE%	^{143}Nd/ ^{144}Nd #
R12HA01	USGS	177	19.327	0.060	15.664	0.090	39.201	0.120	0.703769	0.0008	0.512772
	ENS*		19.3209		15.6746		39.2368				
R12HA02	USGS	291	19.172	0.060	15.651	0.090	39.108	0.120	0.703586	0.0007	0.512806
	ENS*		19.1347		15.6534		39.0933				
R12HA03	USGS	272	18.813	0.060	15.707	0.090	39.120	0.120	0.704423	0.0008	0.512648
	ENS*		18.7869		15.6971		39.0875				
R120S01	USGS	227	19.099	0.060	15.619	0.090	38.876	0.120	0.703070	0.0009	0.512931
	ENS*		19.0752		15.6098		38.8461				
R120S03	USGS	224	19.158	0.060	15.609	0.090	38.907	0.120	0.703136	0.0008	0.512893
	ENS*		19.1511		15.6129		38.9220				
R120S04	USGS	247	19.029	0.060	15.645	0.090	38.959	0.120	0.703604	0.0008	0.512866
	ENS*		19.0224		15.6565		38.9972				
R120S05	USGS	238	19.021	0.060	15.663	0.090	39.045	0.120	0.703978	0.0007	0.512780
	ENS*		19.0276		15.6838		39.1137				
R120S06	USGS	199	19.035	0.060	15.684	0.090	39.114	0.120	0.703994	0.0013	0.512781
	ENS*		19.0176		15.6780		39.0921				
EN-1 carbonate std									0.709174	0.0009	
SRM-987 std									0.710257	0.0008	
									0.710247	0.0008	
									0.710252	0.0009	
JNd std											0.512088

---

† - USGS results corrected for blank (total Pb ~ 60 pg) and mass fractionation (0.12% per a.m.u.) ; ENS results corrected for mass fractionation

§ - Corrected for blank (total Sr ~30 pg) and mass fractionation (88Sr/86Sr = 8.3752)
The mean value of ^{87}Sr/^{86}Sr for 3 analyses of Sr standard SRM-987 was 0.710252 ±10.

- Corrected for blank (total Nd ~ 60 pg) and mass fractionation (^{146}Nd/^{144}Nd = 0.7219)
The ^{143}Nd/^{144}Nd value for 1 analysis of JNd standard was 0.512087 ±3.

‡ - The 176Hf/177Hf value for 11 analyses of JMC475 was 0.282158 ±4 (2 s.d.)

* - Powder leached in hot 6 N HCl for 50 minutes prior to dissolution

Table X: Pb-Sr-Nd data for basaltic whole-rock samples from Turkey

Table X: Pb-Sr-Nd data for basaltic whole-rock samples from Turkey

error 2SE%	εNd	^{176}Hf/^{177}Hf‡	error ± 2σ	εHf	ΔεHf	mean Δ7/4	mean Δ8/4
0.0005	2.6	0.282965	5	6.8	0.2	8	23
0.0005	3.3	0.282932	6	5.7	-1.9	9	32
0.0004	0.2	0.282837	4	2.3	-1.2	17	75
0.0004	5.7	0.283019	4	8.7	-2.1	5	16
0.0003	5.0	0.282995	10	7.9	-1.9	4	13
0.0008	4.5	0.283019	6	8.7	-0.4	10	35
0.0005	2.8	0.282979	4	7.3	0.4	12	45
0.0008	2.8	0.282966	4	6.9	0	13	47
0.0006							

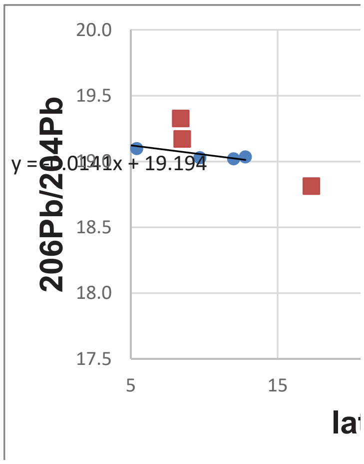

Table X: Pb-Sr-Nd data for basaltic whole-rock samples from Turkey

Table X: Pb-Sr-Nd data for basaltic whole-rock samples from Turkey

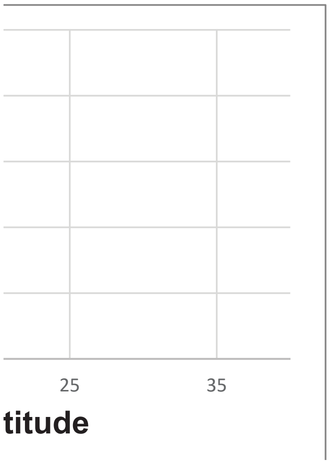

Table X: Pb-Sr-Nd data for basaltic whole-rock samples from Turkey